minerals

*Review*

# The Chemistry and Mineralogy (CheMin) X-ray Diffractometer on the MSL Curiosity rover: A Decade of Mineralogy from Gale crater, Mars

**David Blake[1*], Valerie Tu[2*], Thomas Bristow[1], Elizabeth Rampe[3], David Vaniman[4], Steve Chipera[4], Philippe Sarrazin[5], Richard Morris[3], Shaunna Morrison[6], Albert Yen[7], Robert Downs[8], Robert Hazen[6], Allan Treiman[9], Douglas Ming[3], Gordon Downs[5], Cherie Achilles[10], Nicholas Castle[4], Tanya Peretyazhko[2], David De Marais[1], Patricia Craig[4], Barbara Lafuente[5], Benjamin Tutolo[11], Elisabeth Hausrath[12], Sarah Simpson[3], Richard Walroth[13], Michael Thorpe[14], Johannes Meusburger[1], Aditi Pandey[3, 9], Marc Gailhanou[15], Przemyslaw Dera[16], Jeffrey Berger[2], Lucy Thompson[17], Ralf Gellert[18], Amy McAdam[10], Catherine O'Connell-Cooper[17], Brad Sutter[2], John Michael Morookian[7], Abigail Fraeman[7], John Grotzinger[19], Kirsten Siebach[20], Soren Madsen[7], Ashwin Vasavada[7]**

[1] NASA Ames Research Center, Moffett Field, CA, USA; david.blake@nasa.gov, thomas.f.bristow@nasa.gov, david.j.desmarais@nasa.gov, johannes.m.meusburger@nasa.gov
[2] Jacobs JETSII, NASA Johnson Space Center, Houston, TX, USA; valerie.m.tu@nasa.gov, tanya.peretyazhko@nasa.gov, jeff.berger@nasa.gov, brad.sutter-2@nasa.gov
[3] NASA Johnson Space Center, Houston, TX, USA; elizabeth.b.rampe@nasa.gov, richard.v.morris@nasa.gov, douglas.w.ming@nasa.gov, sarah.l.simpson@nasa.gov, aditi.pandey@nasa.gov
[4] Planetary Science Institute, Tucson, AZ USA; dvaniman@psi.edu, steve.chipera@gmail.com, nicholas.castle@gmail.com, pcraig@psi.edu
[5] SETI Institute, Mountain View, CA, USA; philippe.sarrazin@examinart.com, gordie1997@gmail.com, barbara.lafuente@examinart.com,
[6] Carnegie Institute for Science, Washington, DC, USA; smorrison@carnegiescience.edu, rhazen@carnegiescience.edu,
[7] Jet Propulsion Laboratory, California Institute of Technology, Pasadena CA, USA; albert.s.yen@jpl.nasa.gov, johnmichael.morookian@jpl.nasa.gov, abigail.a.fraeman@jpl.nasa.gov, soren.n.madsen@jpl.nasa.gov, ashwin.r.vasavada@jpl.nasa.gov
[8] Department of Geosciences, University of Arizona, Tucson, AZ, USA; rdowns@arizona.edu
[9] The Lunar and Planetary Institute, Houston, TX, USA; treiman@lpi.usra.edu, aditi.pandey@nasa.gov
[10] NASA Goddard Space Flight Center, Greenbelt, MD, USA; cherie.n.achilles@nasa.gov, amy.mcadam-1@nasa.gov
[11] University of Calgary; Calgary, AB, Canada; benjamin.tutolo@ucalgary.ca
[12] University of Nevada, Las Vegas; Las Vegas, NV, USA.; elisabeth.hausrath@unlv.edu
[13] Genetech, South San Francisco, CA USA; rwalroth89@gmail.com
[14] University of Maryland/Goddard Space Flight Center/CRESST II; Greenbelt, MD, USA; michael.t.thorpe@nasa.gov
[15] CNRS, IM2NP, Marseille, France; marc.gailhanou@im2np.fr
[16] University of Hawaii, Honolulu, HI USA; pdera@hawaii.edu
[17] University of New Brunswick, Fredericton, NB CA; lthompso@unb.ca, catoconnell@gmail.com
[18] Department of Physics, University of Guelph, Guelph, Ontario, CA, rgellert@uoguelph.ca
[19] Division of Geologic and Planetary Sciences, California Institute of Technology, Pasadena, CA, USA; grotz@gps.caltech.edu
[20] Rice University, Houston, TX USA; ksiebach@rice.edu

* Correspondence: david.blake@nasa.gov; valerie.m.tu@nasa.gov

**Citation:** To be added by editorial staff during production.

Academic Editor: Firstname Lastname

Received: date
Revised: date
Accepted: date
Published: date

**Abstract:** For more than a decade, the CheMin X-ray diffraction instrument on the Mars Science Laboratory rover Curiosity has been returning definitive and quantitative mineralogical and mineral-chemistry data from ~3.5-billion-year-old (Ga) sediments in Gale crater, Mars. To date, 40 drilled rock samples and 3 scooped soil samples have been analyzed during the rover's 30+ km transit. These samples document the mineralogy of over 800 meters of flat-lying fluvial, lacustrine and aeolian sedimentary rocks that comprise the lower strata of the central mound of Gale crater (Aeolis Mons; informally known as Mt. Sharp) and the surrounding plains (Aeolis Palus, informally known as the Bradbury Rise). The principal mineralogy of the sedimentary rocks is basaltic, with evidence of early and late-stage diagenetic overprinting. The rocks in many cases preserve much of their primary mineralogy and sedimentary features, suggesting that they were never strongly heated or deformed. Using aeolian soil composition as a proxy for the composition of the deposited and lithified sediment, it appears that in many cases diagenetic changes observed are principally isochemical. Exceptions to this trend include secondary nodules, calcium sulfate veining, and rare Si-rich alteration halos. A surprising and yet poorly understood observation is that nearly all the ~3.5 Ga sedimentary rocks analyzed to date contain 15-70 wt.% of X-ray amorphous material. Overall, this >800-meter section of sedimentary rock explored in lower Mt. Sharp documents a perennial shallow lake environment grading upward into alternating lacustrine/fluvial and aeolian environments, many of which would have been habitable to microbial life.

**Keywords: Powder X-ray Diffraction** 1; Mars 2; Extraterrestrial mineralogy 3; Mars Science Laboratory Curiosity rover

---

## 1. Introduction

The Mars Science Laboratory (MSL) rover Curiosity landed in Gale crater, Mars on August 6, 2012, and has been exploring its floor (Aeolis Palus, informally called the Bradbury Rise) and central peak (Aeolis Mons, informally called Mount Sharp) for nearly twelve Earth years. During its decade-long traverse, Curiosity has travelled more than 30 km and analyzed and documented over 800 vertical meters of flat-lying sedimentary rock. As part of MSL Curiosity's laboratory instrument suite, the Chemistry and Mineralogy (CheMin) instrument determines the mineralogy of scooped or drilled samples delivered to it by the Sample Acquisition, Sample Processing and Handling (SA/SPaH) system [1] or delivered directly from the drill bit. Mineralogical analysis is an invaluable technique for deciphering geologically ancient environments because as thermodynamic phases, minerals have well-defined stability ranges of pressure, temperature, and chemical composition (P, T, X). A full knowledge of the mineralogy of a geologic sample provides insight into the conditions of its formation (paragenesis) and any subsequent changes that have occurred (diagenesis).

CheMin is a powder X-ray diffraction (pXRD) instrument [2] that can identify, quantify, and determine the structure states and major element compositions of minerals in complex polymineralic assemblages such as volcanic rocks and sediments. Here we describe CheMin's geometry, its mode of operation, and the techniques used to process and analyze the downlinked data. We summarize some of the major mineralogical and geochemical discoveries made during the last eleven years and discuss implications for ancient igneous processes, aqueous environments, early habitability, and the gradual drying out and oxidation of the Mars surface environment in the Hesperian (3.7-2.9 Ga) and early Amazonian (2.6 Ga-present) periods.

Gale crater is an ancient 155 km diameter impact crater that sits astride a planet-wide feature on Mars called the "dichotomy boundary" (Figure 1). This boundary separates Mars' two distinct geomorphological terranes: To the north, a relatively flat, topographically low, less cratered (and therefore younger) plain, and to the south, a topographically high, more heavily cratered, and geologically older highland. Gale crater was a deep depression in the Mars crust (4,650 meters below the average elevation of Mars) at a time when the Mars atmosphere was dense enough and the climate warm enough to allow liquid water to flow on its surface.

Gale crater's formation dates to ~3.6-3.8 Ga [3]. Gale is one of a class of "overfilled" craters [4, 5] craters that after their formation filled with sediment, later to be partially exhumed by aeolian processes. The central peak of Gale is comprised of the remnants of this infilling sediment. Orbital infrared imagery and reflectance spectra revealed a vertical succession of sedimentary strata containing hydrous minerals (clay minerals, hydrated Mg-sulfates, etc.) on lower Mt. Sharp that were hypothesized to have been formed in the presence of water, (Figure 2) [6-8]. Gale crater was chosen as the landing site for MSL Curiosity based on these and other orbital images that were interpreted as the morphological remnants of an ancient crater lake, replete with stream channels and alluvial fans extending down from the crater's northern rim, and flat-lying laterally extensive sedimentary strata shrouding Mt. Sharp.

MSL Curiosity [9] brought to Gale crater a full complement of scientific instruments for characterizing surface geology and mineralogy. Optical images of surface materials are acquired with a spatial resolution of tens of microns by the Mars Hand Lens Imager, MAHLI [10] and far-field optical and near-IR imagery at the mm scale with Mastcam [11]. Quantitative compositional data are obtained from surface areas of 2-3 cm diameter using Alpha Particle X-ray Spectroscopy, APXS [12, 13]. Sub-mm point-size elemental data are obtained with the Laser-Induced Breakdown Spectrometry, LIBS instrument [14] on ChemCam [15]. Mineralogical data from powdered 1 cm diameter by 6 cm deep rock cores, or scooped soils, are obtained with CheMin [2] augmented by thermally Evolved Gas Analysis (EGA) data from the Sample Analysis at Mars, SAM instrument [16], near-IR spectral imagery from Mastcam, compositional data from ChemCam-LIBS, and bulk compositional data from the APXS instrument.

## 2. Description of the CheMin instrument

### *2.1. The CheMin geometry*

CheMin is a self-contained lunchbox-sized powder X-ray diffractometer, 30x30x30 cm, with a mass of 10 kg. (Figure 3). The geometry of the CheMin instrument is based on that of an X-ray transmission pinhole camera (Figure 4). A microfocus cobalt anode X-ray tube, operated at 25 KeV and 100 μA, emits a cone of X-rays that is intercepted by a 70 μm collimating aperture. The collimated beam strikes the center of a transmission sample cell 8 mm in diameter and 170 μm thick bounded by 7 μm thick X-ray transparent Mylar or Kapton windows (Figure 5a-b). The samples analyzed by CheMin consist of 50-100 mg aliquots of powdered rock or scooped soil (sieved to a grain size < 150μm) delivered to the cell by the SA/SPaH system (midway through the mission, as a result of a failure of the drill feed mechanism, a modified sample delivery procedure was adopted in which unsieved drill powder was delivered directly to CheMin). During an analysis, the powder in the cell is shaken by piezoelectric vibration, inducing a turbulent flow of randomly oriented grains through the beam over time. Crystalline grains that pass through the beam in Bragg orientation contribute to the diffraction pattern one photon at a time. CheMin's sample cells are arranged in pairs on the periphery of a wheel (Figure 5c) that holds 27 cells that can be filled with sample material, analyzed, and emptied several times, plus 5 sealed cells containing diffraction and fluorescence standards for instrument health checks and calibration.

CheMin's transmission geometry makes it susceptible to sample self-absorption, depending upon the anode material chosen for the X-ray tube. Because Mars is an iron-rich planet, a cobalt anode was chosen rather than a standard copper anode typical of laboratory instruments because CuK$\alpha$ photons with an energy of 8.04 KeV strongly fluoresce Fe, which has its K absorption edge at 7.11 KeV. Indeed, on an iron-rich planet like Mars, if a Cu anode were used in a transmission-geometry instrument, ordinary basaltic composition samples would appear nearly opaque to the beam. An additional performance benefit is that while the longer wavelength of CoK$\alpha$ results in decreased d-value coverage relative to CuK$\alpha$, the major diffraction maxima of clay minerals and those of most rock-forming minerals fall within a range for which CheMin's 2θ resolution is optimized. The CheMin team simulated and measured the diffraction patterns of a wide variety of rock types and specific Mars-relevant minerals at 2θ resolutions ranging from 0.1° to 0.6°. A design specification of 0.35° 2θ was chosen as the minimum (worst) resolution that would still allow the identification of virtually all minerals thought to be on Mars. Changes in the geometry of the instrument could of course result in improved resolution, but only at the expense of count rate, detector size or overall instrument dimensions - critical factors in spacecraft instrument design. Figure 6 shows a ray-tracing simulation of the CheMin geometry, illustrating its range and 2θ resolution [17]. The CheMin flight instrument collects diffraction data over a 2θ range of 3° to 53° (CoK$\alpha$) with a Full Width at Half Maximum (FWHM) figure of merit ranging from 0.25° to 0.35° 2θ sufficient to discriminate virtually all minerals in complex mixtures. Plotted on the 2θ resolution curves in Figure 6 are FWHM peak widths for the four diffraction standards on the CheMin sample wheel. Despite CheMin's relatively poor 2θ resolution, Rietveld refinement and other whole pattern fitting techniques can nevertheless be used to identify, quantify, and determine the lattice parameters and crystal chemistry of virtually all minerals.

### *2.2. The CheMin detector and CheMin data products*

Diffracted and fluoresced photons from the sample are directly detected by CheMin's image sensor, a 2.5 cm square Charge Coupled Device (CCD) having a 600x582 array of 40 μm square pixels. When an X-ray photon is absorbed into the silicon of the detector it dissipates into a cloud of electron-hole pairs that can be tens of μm in diameter depending on the photon's energy. The pixel size of the detector was chosen so that in most cases, the charge cloud generated by the photon is absorbed within a single pixel. CheMin's CCD-224 imager is a custom e2v (Now Teledyne e2v) frame-transfer device. The front-illuminated design has an open gate structure on its surface to optimize detection of low-energy photons and is deep-depleted to maximize the absorption of higher energy photons (e.g., detection efficiency of 0.35 for CoK$\alpha$). The CCD is actively cooled by a Rycor™ tactical cryocooler to reduce background [18]. The cryocooler dissipates heat into Curiosity's Rover Avionic Mounting Platform ("RAMP"). The temperature of the RAMP varies depending on season and time of day from -5 to 20 C. As the cryocooler is only able to maintain a ΔT of -45 C between the RAMP and the CCD, CheMin is operated at night, when the temperature during analysis stays at ~-50 C. Operating the CCD at this temperature lowers background noise to improve the signal-to-noise ratio of the detector.

The CCD is operated in single photon counting mode, meaning that single frames of data are collected and read often enough so that in the vast majority of cases, each pixel will contain either a charge equivalent to the energy of a single detected photon, or background. When operated in this fashion, the detector records both the energy and the x, y pixel position of each photon. The energy of a single electron-hole pair generated in silicon is 3.65 eV; if a CoK$\alpha$ photon is absorbed into a single pixel in the array, on average 6,930 eV / 3.65 eV = 1,899 electron-hole pairs will be generated, which sum to the energy of the CoK$\alpha$ photon. Some energy losses can occur, for example due to secondary fluorescence of Si X-rays from the detector itself, or charge splitting between adjacent pixels. Figure 7 shows a histogram of X-ray energy (displayed as raw Digital Numbers or "DN" from the CCD) from a synthetic ceramic standard containing most of the elements of geologic interest above Z=12, obtained with the CheMin flight instrument during cryogenic vacuum testing on Earth. CheMin was initially designed to have a capability for both XRD and XRF analysis of received samples; however, its XRF analysis capability was descoped for technical and cost reasons early in the flight instrument build.

In a typical sample analysis lasting 10-30 hours and occurring over 2-3 Mars nights, hundreds of ten-second integrations are collected and stored. Raw data consist of 600x582 arrays that store charge collected from individual CCD frames. The data are stored as DN (digital number energy bins) that are transformed to energy (in KeV) after downlink. Ideally, all raw frames would be transmitted to ground for processing, but the data volume is too large for this to be feasible. As a result, only a few frames of raw data are returned to monitor background, assess the health of the CCD and to choose DN values suitable for background and high and low DN limits for energy-discriminated diffraction products. During the on-board processing of individual raw single frames, photons that fall within a window that brackets the energy of CoK$\alpha$ (6.93 keV) are summed into a 600x582 2D counting number array that constitutes an energy-selected CoK$\alpha$ Debye-Scherrer pattern of the sample. An energy histogram of all photons summed from the frames constitutes an X-ray fluorescence spectrum of the sample. An example of energy-selected diffraction and fluorescence data is shown in Figure 8. A minor frame is typically comprised of 180 10-second exposures. As many as 45 minor frames are summed to yield a high signal-to-noise 2D diffraction pattern for analysis. As a contingency measure, a diffraction product is constructed that is comprised of individual frames summed into a 600x582 array as raw data without energy-selection (called "Film mode" because the CCD collects photons in the same fashion as X-ray sensitive photographic film). A single real number array holds the summed images for each minor frame. Figure 9a shows a single minor frame of Film mode data from Rocknest, the first sample analyzed on Mars. The degradation of the image is due to the detection of a flood of neutrons and cascades of secondary X-ray photons from the rover's Radioisotope Thermal Generator (RTG) power source (which contains several kg of plutonium), and cosmic ray background. For comparison, Figure 9b shows CoK$\alpha$ energy-selected data from 6 summed minor frames of a modern regolith target Rocknest (RN, sol 0095). All downlinked higher-level data products are described in [2] and can be downloaded from the "Gale Crater Mineralogy and Geochemistry Sample Database," [19]. However, in all cases, energy selected CoK$\alpha$ data are used in our published analyses.

### 2.3. CheMin 2$\theta$ calibration

The total X-ray beam path from the sample to the detector is 18.5 mm. As a result of this compact geometry, the largest error in 2θ pattern measurement is introduced by the ±50 μm machining tolerances of individual sample cells. Morrison et al. [20] describe a method to correct for these sample displacement errors using the refined lattice parameters of plagioclase feldspar, a mineral found in sufficient abundance in all but one sample analyzed on Mars to date. A compilation of the published lattice parameters of terrestrial plagioclase feldspars is found in the RRUFF database [21] see also [20, their Appendix 1]. If one plots the relationship of the plagioclase $\gamma$ vs. c parameters for terrestrial examples, the points lie on a linear regression line [20], their Figure 3). Using a sample-detector distance calculated from an analysis of one of CheMin's standards as a starting point, refined lattice parameters for $\gamma$ and c are determined. The sample-detector distance for each cell is then adjusted by increments until $\gamma$ vs c from the Martian plagioclase falls on the $\gamma$ vs c parameter regression line for terrestrial plagioclase.

### 2.4. Analysis of CheMin diffraction patterns

Data are downlinked from the spacecraft as 2D "minor frames." Each minor frame is a 600x582 counting number array of CoK$\alpha$ photons summed from 180 individual 10-sec. exposures of the CCD. A complete analysis typically includes the data from 15 to 45 minor frames of 30 minutes each collected over two or more martian sols. However, in some off-nominal analyses, for example when grain motion is poor due to clogging, the mineralogy of patterns containing as few as 4 minor frames has been successfully quantified, albeit with higher mineral detection limits (e.g., the Buckskin sample reported in [22]). All minor frames contain some off-ring blobs and spots due to cosmic rays, detector defects, etc. These are removed and replaced with local background values prior to the 2D to 1D conversion. Once downlinked, CheMin's 2D Debye diffraction rings, corrected for arc length, are summed circumferentially around the central beam to yield a conventional 1D diffraction pattern using a modified version of GSE_ADA software v1.09 [23]; however commercial software such as FilmScan™ (ICDD, Newtown Square, PA) can be used as well.

All raw data from the CheMin instrument are downloadable from the "Gale Crater Mineralogy and Geochemistry Sample Database," [19] as well as 2D and 1D diffraction patterns, crystallographic information files (CIFs) files chosen for quantitative analyses and cell parameter refinement, our preferred analytical result, companion data from other instruments and all papers published by the CheMin science team.

There are 3 components that commonly contribute to CheMin's diffraction patterns: A crystalline component, a poorly crystalline clay mineral component and an X-ray amorphous component. The treatment of these three components during quantitative analysis is described below:

### *2.4.1. Analysis of the crystalline component*

In each pattern, a small contribution to the background is due to the Kapton or mylar cell windows, and this "empty cell" contribution is subtracted during the refinement process. An aluminized mylar film in the beam path between the sample and the detector is used to shield the CCD from sample-generated optical fluorescence. The crystalline Al on this "light shield" produces diffracted intensity at approximately 25.5° and 32° 2θ that must be subtracted from the pattern. A custom light shield CIF was constructed for this purpose; however, because the most intense light shield peak occurs at the position of the principal peak of cristobalite, a cristobalite CIF can also be used. If clay minerals are present, patterns obtained from clay mineral standards with CheMin-IV, a ground-based instrument having the same geometry as CheMin, are fit to the pattern and subtracted. Finally, nearly all samples analyzed to date contain X-ray amorphous components, manifested as a broad scattering background having a maximum between 26° and 31° 2θ, and a low angle rise extending from 4° to 14° 2θ. This scattering intensity is modelled and fit to the pattern so that proper peak intensities and backgrounds can be retrieved from crystalline component. For the identification and refinement of the crystalline component, CIFs from the AMCSD database (http://rruff.geo.arizona.edu/AMS/amcsd.php) are used in addition to a small number of CIFs created from structure refinements of minerals hand-picked from Martian meteorites. The identities, amounts and refined lattice parameters of crystalline phases present in the sample are determined through search-match and Rietveld refinement (e.g., [24, 25]) using the Jade™ code (ICDD, Newtown Square, PA). Immediately after initial data are downlinked, independent refinements are performed by four or five members of the CheMin team, and a synopsis of these results is provided to the MSL Science Team for planning purposes. Once an entire analysis (comprising two or more nights of data) has been downlinked, a sample displacement offset is calculated and applied to the pattern and a second round of Rietveld refinements is conducted. The reported mineral identifications, abundances and mineral lattice parameters are a consensus result of these refinements. Compositions are calculated for those minerals having variable compositions and present at >~3 wt. %, using regression equations of lattice parameter vs. composition from [26]. These minerals typically include plagioclase and alkali feldspars, Mg-Fe-Ca C2/c clinopyroxene, Mg-Fe-Ca P21/c clinopyroxene, Mg-Fe-Ca orthopyroxene, Mg-Fe olivine, magnetite and other spinel oxides, and alunite-jarosite. In some cases, the Scherrer equation [27] is used to identify crystal sizes when the FWHM peak width of a particular mineral exceeds the instrument FWHM.

### *2.4.2. Analysis of clay mineral components*

In terrestrial laboratories, the identification of clay minerals with X-ray diffraction typically involves the use of oriented sample mounts and sample processing techniques such as humidity variation, sample heating or treatment with ethylene glycol; none of these methods were implemented for the CheMin instrument on Mars. In the low Relative Humidity (RH) environment of the CheMin sample cell, expandable clay minerals lose their interlayer water with the result that collapsed smectite cannot be discriminated from illite and other 2:1 clay minerals solely on the basis of the position of the (001) diffraction maximum (e.g., [28]). However, the breadth of the (001) diffraction peak and lack of correlation between clay mineral content (determined with CheMin) and bulk K content of the sample (determined with the APXS instrument) suggest that illite (which contains K as its interlayer cation) is not present [29]. In addition, kaolinite-group clay minerals have a distinctive diffraction at low 2θ that has not been observed in any sample to date.

For smectite clay minerals, the occupancy and cation species within the octahedral sheet (i.e., dioctahedral vs. trioctahedral) is used for clay mineral identification and has important implications for mineral paragenesis. In terrestrial laboratories, the 06*l* band is used for this purpose, but is beyond CheMin's 2θ range. The 02*l* band (22.5° to 23.1° 2θ CoK$\alpha$; 4.53 Å to 4.47 Å) is used for this purpose [30], albeit with occasional interferences from diffractions from other minerals. NEWMOD software [31] is used for detailed modeling of the (001) maximum of clay minerals (e.g., see [32] and [33] and the BGMN software [34] is used for detailed modeling of the 02*l* band in clay minerals (e.g., see [28, 29]. Water release EGA data from SAM complement CheMin data and can also be used to discriminate between the types of smectite clays present in a drill target based on the temperature of the water evolution (e.g., [35]).

The amount of clay mineral in a sample vs. other components is determined using the Full Pattern Fitting program FULLPAT [36, 37]. Purified clay mineral standards, heated prior to analysis to collapse the interlayer to 10 Å, were analyzed in CheMin-IV. A combination of trioctahedral and dioctahedral smectite clays account for the majority of clay mineral components in the Martian samples at Gale.

### 2.4.3. *Analysis of X-ray amorphous components*

All CheMin samples analyzed to date on Mars contain an X-ray amorphous component. The proportion of the X-ray amorphous component relative to the crystalline and clay mineral components is determined by two complimentary methods:

By diffraction: Using FULLPAT, X-ray amorphous standards are chosen to fit the broad scattering background at mid-2θ and a rise in background at low-2θ not explained by the crystalline or clay mineral components. X-ray amorphous standards (allophane, palagonite, hisingerite, synthetic basaltic composition glass, opal-A, etc.) spiked with a beryl or corundum standard were analyzed in the CheMin IV instrument to determine their RIR values [38, 39]. These patterns are then fit to the unknown pattern. The amorphous component(s) found in the Martian samples are almost certainly not the same structure or composition as their lab-measured surrogates. For this reason, the relative amounts of the amorphous component(s) determined with FULLPAT are stated as ±2σ of the amount present.

By elemental composition: A second method utilizes the bulk elemental composition of the sample as determined by APXS, obtained from the "dump pile" of material collected for analysis (this is not the same aliquot of sample analyzed by CheMin, and could have subtle compositional differences). The composition of the crystalline component (as determined by CheMin using refined lattice parameter vs. composition equations in [26], multiplied by a scalar value is subtracted from the bulk composition determined by APXS. The scalar value is increased until one of the major oxides in the bulk composition is reduced to zero. These two methods produce the same result within the stated error limits.

Smith et al. [40] performed laboratory analyses of natural samples containing X-ray amorphous components using three different quantitation methods (Rietveld refinement, full pattern fitting analysis and mass balance calculations) and compared them to a commonly used quantitative XRD method using internal standards. Amorphous abundance and amorphous composition measurements were found to be comparable for all methods. Results from CheMin analog methods were comparable to quantitative XRD results using internal standards. These results suggest that the amorphous abundances and compositions determined with CheMin XRD data and APXS bulk compositional data are reasonably accurate, albeit with the caveat that the structure of the amorphous component(s) (and therefore the scattering distribution of the broad amorphous maxima) are unknown.

Lattice parameters are not sensitive to the presence of minor or trace elements incorporated in the minerals; without a correction, these elements measured in the bulk sample would be assigned to the amorphous component. To correct for this, minor and trace elements were measured from mineral phases found in Martian meteorites and added to their respective mineral phases in the samples analyzed on Mars.

## 3. Major discoveries ("CheMin's diary of discovery")

As of sol ~4100 (a martian sol, or day, is ~40 minutes longer than an Earth Day), 40 drilled samples of sedimentary rock and 3 scooped samples of soil have been analyzed over the course of Curiosity's 30+ km transect. These samples document the mineralogy of over 800 vertical meters of flat-lying fluvial, lacustrine, and occasional aeolian sedimentary rocks that comprise the lower strata of Mt. Sharp and the surrounding plains (Figure 10). Table S1 lists the attributes of all samples analyzed to date, and Figure S1 shows images of the drill holes and scooped samples. Figure 11 traces Curiosity's path across the Bradbury Rise and its ascent up lower Mt. Sharp. The principal mineralogy of the rocks is basaltic, with evidence of early and late-stage diagenesis involving fluids. The rocks in many cases preserve much of their primary mineralogy and depositional sedimentary structures, suggesting that they were never strongly heated or deeply buried. Using the composition of present-day aeolian regolith as a proxy for the composition of the deposited and lithified sediment, it appears that in many cases the diagenetic changes that occurred were isochemical and the minerals present are authigenic. Exceptions include secondary nodules and crystal dendrites, calcium sulfate veining, silica enrichment of the amorphous component in Mt. Sharp sedimentary strata and Si-rich alteration halos. A striking hematite-rich feature in lower Mt. Sharp called Vera Rubin ridge is interpreted to be lake sediment subject to relatively enhanced diagenesis in comparison with adjacent age equivalent strata. A surprising and still poorly understood observation is that all the ~3.5 Ga sedimentary rocks analyzed to date contain 15-70 wt.% X-ray amorphous material. Overall, the >800-meter section of sedimentary rock explored in lower Mt. Sharp documents a perennial shallow lake environment grading upward into alternating lacustrine/fluvial and aeolian environments. The present mineralogy of the sedimentary rocks is a result of depositional, early diagenetic, and late diagenetic alteration occurring over hundreds of millions of years. Taken together, the sedimentology and mineralogy of the strata appear to document the drying out and oxidation of the Mars surface environment in Hesperian time (3.7-2.6 Ga).

### *3.1. The Mineralogy and Composition of the Mars Global Soil*

Curiosity investigated three unconsolidated aeolian features during its traverse of Gale crater. Rocknest (RN) is an inactive near-recent sand shadow investigated by Curiosity from sol 57 to sol 100 [41, 42, 43], Namib Dune (Gobabeb, GB) is part of the active Bagnold Dune Field that was investigated from sol 1164 to 1244 [44, 45] and the Mount Desert Island ripple field (Ogunquit Beach, OG), also part of the Bagnold Dune Field, was investigated from sol 1602 to 1660 [46, 47].

CheMin's analysis of the scooped and sieved <150 μm grain size component of Rocknest provided the first quantitative mineralogic analysis of Mars soil [41, 42, 43]. Rocknest is an accumulation of aeolian sediment deposited in the lee of a high relief cluster of rocks in the path of the wind (called a "sand shadow"). The surface is comprised of rounded 1- to 2-mm sand grains that form an armored surface ~2 to 3 mm in thickness. Beneath this armored surface, the bedform interior (analyzed by CheMin) consists of finer-grained material whose size distribution extends through the lower resolution limit of MAHLI images (~30 μm per pixel [10]). Rocknest is similar to coarse-grained granule ripples encountered at both Gusev crater and at Meridiani Planum by the MER Spirit and Opportunity rovers [48-51]. At Meridiani Planum, where a cratering record postdates the deposition of a field of pristine granule ripples, crater counting yields an estimated bedform age of

50,000 to 200,000 years [52]. If one assumes that the coarse-grained bedform armor at Rocknest was deposited by the same high-wind event (perhaps during the most recent period of Mars obliquity [53, 54]), the Rocknest sand shadow would have been inactive for that period of time as well. Figure 12 shows the first X-ray diffraction pattern returned from Mars, 100 years after the discovery of X-ray diffraction by Max von Laue [55].

Table 1 lists the APXS compositions of aeolian materials from RN and GB (MSL) compared with average soils from Meridiani Planum and Gusev crater (MER). The striking similarity in composition between modern soil samples measured at various locations on Mars is compelling evidence that these materials represent a global soil average composition [41- 43]. The mineralogy of soils analyzed by the MER rovers was determined from mid-IR spectral deconvolutions, normative geochemical calculations, and Mössbauer spectroscopy [56-58]. The mineralogy of RN, GB and OG as determined by CheMin is chemically and mineralogically similar to that inferred for Martian basalts across the planet and broadly similar to estimates of the average Martian crust [59]. These basalts contain (or have normative chemical compositions consistent with) the minerals olivine, augite, pigeonite, and plagioclase feldspar. The mineral proportions of the crystalline components of RN, GB, and OG are virtually identical to those determined from normative calculations for the unaltered Adirondack class basalts from Gusev crater [11, 56, 57] (Table 2). The compositions of plagioclase, olivine, augite and pigeonite from Rocknest and Gobabeb (determined from their refined lattice parameters [20, 26] shown in Table 3 are a significant revision of those shown in [41] and are the preferred values. The molar Mg/(Mg+Fe) ratios for olivine and pigeonite in both samples are similar, permissive evidence that they formed in the same environment. However, the augite is distinctly more magnesian, and could not have formed in equilibrium with the pigeonite and olivine, suggesting that either the source basalts had a complex cooling history, or the pyroxenes came from different basalts [44, 45, 26]. It should be noted, however that the refined unit cell parameters and calculated crystal chemistries of pyroxenes in samples with more than one pyroxene species present have significant errors associated with them due to the relatively low 2θ resolution of CheMin.

The fraction of RN soil <150 μm in particle size analyzed by CheMin contains ~80% crystalline material consistent with a basaltic heritage and ~20% X-ray amorphous material. The amorphous component of RN is iron-rich and silicon-poor, is the host of the volatiles (water, oxygen, sulfur dioxide, carbon dioxide, and chlorine) detected by SAM [60] and likely constitutes the fine-grained nanophase oxide component first described from basaltic soils analyzed by MERs [57].

### 3.2. *Discovery and characterization of an ancient habitable environment on Mars*

In its first drilled sample, acquired on sol 192, Curiosity documented a section of fluvio-lacustrine strata at Yellowknife Bay (YKB), an embayment on the floor of Gale crater, approximately 500 m east of the Bradbury landing site (elevation, -4520 m) [61, 62]. X ray diffraction data from CheMin show that two powdered mudstone samples (John Klein (JK) and Cumberland (CB)) drilled from the Sheepbed member of this formation contain up to 20 wt% clay minerals. Figure 13a shows the bit of the percussion drill that is used to produce the powder, and Figure 13b shows the test drill hole (upper left) and the final drill hole (lower right) of JK (the diameter of the drill hole is 16 mm). Figure 13c shows the sieved powder held in the sample cup. A trioctahedral smectite, characterized as a ferrian saponite [28, 30, 63] is the only clay mineral phase detected in these samples (Figure 14). The mudstones are part of a section of the fluvio-lacustrine YKB formation, derived from erosion of rocks along the Gale crater rim, as confirmed by a bulk K-Ar age of 4.21 ± 0.35 Ga [64]. The stratigraphic relationships between the YKB formation and either the Peace Vallis fan or the strata of lower Mt. Sharp are uncertain. However, strata of the YKB formation, including the clay mineral-bearing Sheepbed member post-date the Noachian-Hesperian boundary (~3.7 Ga) and are younger than the majority of clay minerals documented on Mars from orbit [30, 65, 66].

The clay minerals at YKB are interpreted to have formed *in situ* and indicate that paleoenvironmental conditions within the fluvio-lacustrine system were potentially habitable for life [30, 66]. The relatively low abundance of olivine (note: olivine is considered to be a contaminant from the previously drilled sample (RN) since it was not seen in CB, drilled 1 m away from JK) and enriched level of magnetite in the Sheepbed mudstone, when compared with regional basalt compositions derived from orbital data and directly determined from the Rocknest sand shadow suggest that clay minerals and magnetite formed *in situ* via aqueous alteration of olivine. Mass-balance calculations are permissive of such a reaction [28]. Early diagenetic fabrics (e.g., evidence of soft-sediment deformation, raised ridges in the sediment likely caused by volume expansion during clay mineral formation, hollow sedimentary concretions, etc.) indicate that clay mineral formation occurred prior to lithification [66]. Thermodynamic modeling [28] suggests that the production of authigenic magnetite and Fe-saponite at surficial temperatures requires a moderate supply of oxidants, allowing circum-neutral pH. The sluggish kinetics of olivine alteration at low temperatures imply the presence of fluids for thousands to hundreds of thousands of years.

The mineral assemblage at JK (and CB), as well as the physical sedimentology of the Yellowknife Bay formation were found sufficient by the MSL team to identify a habitable environment in ~3.7 Ga lakebed sediments in Gale crater, the criterion for MSL mission success [66]. Other habitable environments have been discovered and characterized during Curiosity's traverse through lower Mt. Sharp, both in the depositional environment (as in Yellowknife Bay), and in the shallow subsurface diagenetic environment. Indeed, the unexpected abundance and diversity of clay minerals in sedimentary rocks in Gale crater and the apparent longevity of this lacustrine sedimentary system indicate that near-surface aqueous alteration (and habitability) continued into the early Hesperian (~3.5 Ga) on Mars. Examples have also been found of post-depositional diagenetic alteration that would have destroyed evidence of a habitable environment had it existed. The conclusion is that mineralogy, contextualized with sedimentological observations, is quite capable of evaluating habitability in ancient rocks and elucidating post-depositional diagenetic changes that would preserve or destroy such evidence.

### *3.3. Evidence for a Diverse Basalt Mineralogy on Mars*

Curiosity arrived at the Windjana drill site in the Bradbury group on sol 0623. Windjana, (WJ, elevation -4481 m), the fourth sample analyzed by CheMin, is the most potassic alkali-rich rock on Mars to be analyzed for its mineralogy by XRD. The source lithologies for WJ sediments represent a complex igneous province which includes (from their mineralogies) potassic trachyte, plagioclase-rich basalt (i.e., tholeiitic), and mafic basalt (i.e., shergottitic) [67]. This result implies that the northern rim of Gale crater, the source of these sediments, exposes an igneous complex that is at least as diverse as those found in similar-age terranes on Earth.

Curiosity crossed the landing ellipse boundary and began to climb Mt. Sharp on sol 0753. This ascent demarks the boundary between Bradbury Group rocks of the crater floor and the rocks of the Mt. Sharp Group (Fig. 10).

### *3.4. Clay Mineral Diversity in the Sedimentary Strata of Gale crater*

CheMin analyses within Gale crater have documented changes in the amounts and species of environmentally sensitive minerals including pyroxenes, sulfates, clay minerals and Fe-oxides as a function of stratigraphic position [29, 68]. There is also an observed increase in the chemical index of alteration (extent of alteration of mafic detritus) derived from geochemical analysis in the upper part of the Murray Fm. [69]. Coupled with the observed sedimentological changes (e.g., depositional, and early diagenetic features that indicate a shallowing of the lake and episodic lake desiccation [70, 71]), these mineralogical changes document the drying out and oxidation of the local Gale crater environment. Because planet-wide orbital IR observations show similar sequences of mineralogical change, this is thought to be representative of the drying out and oxidation of the planet-wide Martian environment [29].

In lower Mt. Sharp, clay minerals were found in virtually all analyzed samples. For samples in which clay minerals were not detected within the Mt. Sharp Group rocks, evidence of post-depositional diagenetic alteration is sufficient to explain their absence. For all but two clay mineral detections (in which the 02*l* band is either weak or obstructed by diffraction peaks from other minerals), the clay minerals can be identified as trioctahedral smectites, dioctahedral smectites, or mixtures of both. Rare exceptions include the sample Oudam (OU, sol 1363, -4435 m) which exhibited a peak at 9.6 Å, and the samples Kilmarie (KM, sol 2384, elevation -4155 m) and Groken (GR, sol 2912, elevation -4130 m) which exhibited a peak at 9.22 Å (in the case of KM and GR, a robust 10 Å smectite clay peak is present as well). Bristow et al. [29] characterized the 9.6 Å basal spacing clay mineral in OU as ferripyrophyllite, likely exogenous material transported into the crater as sedimentary detritus from older bedrock. However, analyses of samples drilled higher in the section at Vera Rubin Ridge identified clay minerals having a 9.6 Å basal spacing in mineral assemblages that would support *in situ*, diagenetic formation [72]. The 9.22 Å peak observed in the samples KM and GR is assigned to a mixed layer serpentine/talc [32] or minnesotaite/greenalite [33]. Bristow et al. [29, 32] concluded that these clay minerals were likely exogenous material, transported into the crater as sedimentary detritus from older bedrock, whereas [33] postulated that the mixed-layer clay formed via groundwater-lake water mixing.

The clay mineral changes observed going up-section from the Yellowknife Bay Fm. of the Bradbury Group into the Murray Fm. of the Mt. Sharp Group include a transition from trioctahedral to dioctahedral clay minerals. Figure 15 shows diffraction patterns of samples analyzed from JK (elevation -4520 m), Marimba (MB, elevation -4400 m) and Glen Etive 2 (GE, elevation -4120 m), representative of a 400 m thick section of flat-lying sedimentary strata, along with measured patterns for clay mineral standards SAz-1 (dioctahedral), and SapCa-1(trioctahedral) (note: the MSL drill was not available between elevations -4380 m and -4220 m; as a result no CheMin data were recorded from this interval). The position of the 02*l* band shifts from 22.5° to 23.1° $2\theta$ Co$K\alpha$ (4.53 Å to 4.47Å), indicating a shift in the proportion of trioctahedral to dioctahedral smectite. The formation of dioctahedral smectite clays from basaltic precursors or from preexisting trioctahedral smectite clays requires greater elemental mobility and more oxidizing conditions than those of the trioctahedral smectites seen in Yellowknife Bay [29]. In samples like Glen Etive (from the Glen Torridon region), which contain dioctahedral smectites exclusively, the position of the 02*l* band and derived unit cell lengths of smectite crystals along the b axis indicate that approximately half of the octahedral cations are $Fe^{+3}$, with $Al^{+3}$ filling the remaining sites [32]. Similar $Fe^{+3}$-rich dioctahedral smectites are inferred to be mixed (albeit in varying proportions) with Mg-rich trioctahedral smectites in lower strata, based on the modeling of XRD patterns, SAM-EGA analyses of the same samples, and regional orbital IR observations [29]. These authors argue that the observed mineralogical changes are early diagenetic, perhaps occurring in the shallow subsurface prior to lithification. Other mineralogical changes include the removal of some of the more reactive minerals in the original basaltic sediment (i.e., pyroxenes and olivine) and a change in the iron oxide mineralogy from magnetite ($Fe_2^{+3}Fe^{+2}O_4$) to hematite ($Fe_2^{+3}O_3$).

### *3.5. Early- and Late-stage Diagenesis in the Lower Murray Formation*

Curiosity reached Mt. Sharp on sol 0753. The lower Murray formation at the base of Mt. Sharp is comprised of finely laminated mudstone with near-horizontal laminae, deposited in a subaqueous lacustrine environment [73]. Other depositional environments in this interval include sandstones interpreted as distal deltaic facies and fluvial facies discharging into the lake [74]. The lower Murray Formation is time equivalent to and interfingers with coarser-grained strata of the Bradbury group [75]. Primary depositional textures are preserved such as fine-scale laminations in the mudstone facies; however, there is also evidence of early and late-stage diagenesis in the form of crystal molds, secondary crystallization, and calcium sulfate veins. The sediments could not have been deeply buried or heated, as much of the primary mineralogy persists and depositional sedimentary features are preserved. In the Pahrump Hills – Marais Pass region, CheMin documented the loss of mafic igneous phases and clay minerals and the introduction of secondary diagenetic minerals such as jarosite, suggesting the action of weakly acidic fluids [74]. Figure 16 shows diffraction patterns obtained from the drill samples Confidence Hills (CH, sol 0765, elevation -4460 m), Mojave 2 (MJ, sol 0885, elevation 4459 m), Telegraph Peak (TP, sol 0923, elevation -4454 m) and Buckskin (BK, sol 1062, elevation -4447 m). Table 4 (from [74] lists the mineralogical compositions of the four samples. Hematite is seen in abundance for the first time on the mission (and its detection marked Curiosity's arrival at Mt. Sharp), magnetite is present in all samples (and in increased abundance in the TP sample), and pyroxenes are seen to decrease in abundance going up section. Phyllosilicates are present in small amounts in CH and MJ but absent in TP and BK. Relative to the Bradbury Formation rocks, the lower Murray Formation rocks exhibit an overall enrichment in $SiO_2$. Bulk $SiO_2$ abundance (from APXS), the $SiO_2$ abundance of the crystalline component (from CheMin), and the $SiO_2$ abundance of the amorphous component (bulk composition - crystalline composition) all increase going up-section.

Rampe et al. [74] hypothesized that sediments at the base of the Pahrump Hills were deposited in a lake with near pH-neutral waters. Initially deposited sediments contained magnetite. The refined unit cell of the magnetite (~8.35-8.36 Å) is decreased relative to stoichiometric magnetite (8.396 Å; e.g., [76]). The decreased unit cell length can represent vacancies in the structure, for example $3Fe^{+2} = 2Fe^{+3} + [\ ]$ (e.g., [20] their Figure 9). Cation deficient magnetite can occur by leaching of $Fe^{+2}$ from the structure with acidic solutions (pH 2-2.5; [77]). This cation deficiency supports the Rampe et al. (2017) [74] proposed model of diagenesis in acidic groundwater.

Early diagenesis from multiple intrusions of groundwaters resulted in the dissolution/transformation of original minerals and the precipitation of new minerals (oxidation of magnetite to hematite, precipitation of jarosite/natrojarosite $(K,Na)Fe_3(SO_4)_2(OH)_6$ and gypsum). Pore fluids were hypothesized to be mildly acidic and oxic [74] and mobilized minor elements such as Zn and Ni (identified by APXS) were precipitated as sulfate salts (Mg-Ni sulfate concretions) identified by ChemCam. An alternative view is expressed in [78] in which the sequence of observed mineralogical changes is viewed as primary rather than diagenetic, resulting from redox stratification in the lake.

Radiometric K/Ar dating of the jarosite from MJ from the SAM instrument indicates that it was formed at 2.57 ± 0.39 Ga [79], thus documenting a long history of aqueous interactions in Gale crater sediments extending from the deposition of the Yellowknife Bay Formation to the deposition and diagenesis of the Murray Formation (a period of nearly 1 Gy).

At the top of the Pahrump Hills, crystalline silica phases were identified in abundance for the first time. TP and BK each contain significant amounts of the $SiO_2$ polymorph cristobalite, and the BK sample collected at Marais Pass, (surprisingly) contains the $SiO_2$ polymorph tridymite [22]. On Earth, tridymite is found as a high-temperature low-pressure, vapor-deposited mineral associated with silicic volcanism (typical in continental crust settings as a consequence of plate tectonics). It was hypothesized in [22] that this material could have been washed into the lake as exogenous detrital volcanic material from an unknown silicic source (see also Yen et al. [80, 81] which proposes instead an *in situ* hydrothermal, fumarolic mechanism for formation). The mineralogy of the Buckskin sample is consistent with terrestrial fumarolic deposits, and the temperature could have been within tridymite's thermodynamic stability field (>870°C) driven by a yet undetected subsurface volcanic heat source. However, there is no sedimentological evidence in the localized strata indicating extremes of heat and primary bedding is in many cases preserved.

It is clear that a late-stage diagenetic event occurred which involved silica-rich fluids (probably associated with the alteration halos observed in Stimson Fm. aeolian sandstone described in Section 3.6). The petrogenesis of tridymite therefore remains an open question and may be associated with this late-stage diagenetic event in a paragenetic mode not seen on Earth.

### *3.6. Si-rich Alteration Halos in the Stimson Formation Aeolian Sandstone*

In the Marais Pass area at the top of the Pahrump Hills, Curiosity first encountered and drilled the Stimson Formation, an aeolian sandstone overlying the Murray Formation. Where it has not been removed by erosion, the Stimson sandstone is observed as a cap rock that truncates bedding in the Murray formation, thus defining a disconformity between the two units [82-84]. Watkins et al. [82] noted that the discovery of this disconformity reveals what constitutes the rock cycle on Mars, a planet in which plate tectonics is not an active geologic agent: Older lacustrine sediments (Murray Fm.) are deposited, lithified, and eroded. Younger aeolian sediments (Stimson Fm.) are deposited over the eroded Murray Fm. and are then themselves lithified. The entire sequence is then eroded and exhumed by aeolian abrasion over an extended interval of time up to the present. The lithified aeolian sandstones of the Stimson are seen to extend laterally for kilometers, and vertically through nearly 400 meters of flat-lying Murray Formation strata up to the Greenheugh pediment, an erosional remnant of the Stimson [84].

Light-toned, fracture-associated alteration halos crosscut both the Murray Formation and the overlying Stimson Formation in the vicinity of Marais Pass [85], e.g, Figure 17. CheMin performed mineralogical analyses of the parent rock and the fracture-associated alteration halos at Big Sky / Greenhorn (BS, sol 1122 (parent Stimson) / GH, sol 1140 (altered Stimson), elevation -4460 m); and Okoruso / Lubango (OK, sol 1335 (parent Stimpson) / LB, sol 1325 (altered Stimpson), elevation -4450 m). Figure 18 shows the BS and GH diffraction patterns as well as a diffraction pattern from Edinburgh (EB, sol 2715, elevation -4060 (parent Stimson)), a sample drilled from the Greenheugh pediment ~400 m higher in the section than BS. Dotted lines denote the differences between what is likely the most pristine Stimson (ED), slightly altered Stimson (BS) and highly altered Stimson (GH). Major mineralogical changes include the overall loss of pyroxene in altered Stimson, the presence of olivine in EB (likely an original mineral of the parent sandstone) and its absence in BS and GH, and the presence of a major amount of anhydrite in the altered Stimson (GH). Table 5 lists the mineral abundances for each. The mineralogical changes in the fracture-associated halos require multiple aqueous alteration stages with fluid chemistries encompassing a wide range of pH. Significant mineralogical changes include the dissolution of original basaltic mineral components (plagioclase, pyroxenes) resulting in the passive enrichment of silica, but mass-balance calculations from APXS data suggest that additional silica and sulfate were incorporated as well [85]. Amorphous silica enrichment and calcium sulfate veining are pervasive features of the Murray Formation, the former without disruption of original sedimentary features, and the latter commonly crosscutting them. Calcium sulfate veining occurred both before deposition of the Stimson Formation [82] and after the Stimson Formation was deposited and lithified [85]. Silica enrichment appears to be the latest diagenetic change observed by *Curiosity* in Mt. Sharp rocks, occurring after the lithification of the Stimson Formation. The silica-rich fluids must have been introduced at some depth, since the alteration halos seen in the Stimson sandstone at Marais Pass result from exposure of the host Stimson to diagenetic fluids emanating from veins under confining pressure. Yen et al. [81] presents evidence that these halos are hydrothermal in origin, associated with the same fluid system that formed the tridymite in BK. Yen et al. [81] proposes that the high silica crystalline and amorphous components found in the Buckskin drill sample Murray Fm. formed through similar processes involving *in situ* hydrothermal silicification.

### *3.7. Vera Rubin Ridge and the Glen Torridon Region*

The most striking features observed in orbital IR images of Gale crater prior to the arrival of MSL-Curiosity (and indeed, a principal reason for choosing Gale as Curiosity's landing site) are the juxtaposed hematite-rich and phyllosilicate-rich layers on lower Mt. Sharp that transition upslope into a sulfate-rich horizon (Figures 2 and 19). These minerals either require liquid water for their formation or contain water in their structures. Because similar mineral sequences have been observed planet-wide in overfilled and exhumed craters like Gale [5], it was hypothesized that the local conditions that existed in Gale crater during their formation may be representative of planet-wide environmental events. It is noteworthy that CheMin has identified clay minerals and Fe-oxides along Curiosity's entire transect up to this point in Gale crater, not just in regions where these minerals were detected from orbit. Orbital IR spectra can be obscured by a few microns of dust, highlighting the need for *in situ* observations by mineralogy instruments such as CheMin. However, the Fe-oxides in Vera Rubin ridge (the hematite-rich exposure) and the phyllosilicates in Glen Torridon (the phyllosilicate-rich exposure) are present in the highest concentrations measured by CheMin in Gale crater.

#### *3.7.1. Vera Rubin Ridge*

Curiosity arrived at Vera Rubin ridge (VRR), the erosion resistant, hematite-rich feature identified from orbit, and drilled the Stoer sample (ST, sol 2136, elevation -4170 m) at a location near the strongest hematite spectral signature seen from orbit, followed by two other VRR samples, Highfield (HF, sol 2223, elevation -4147 m) and Rock Hall (RH, sol 2261, elevation of -4144 m). A fourth sample, Duluth (DU, sol 2057, elevation -4192 m) was drilled immediately below VRR in a region that lacked the strong orbital hematite spectral signal for comparison. The drill tailings from the four samples are markedly dissimilar in appearance (Figure 20) due to mineralogical differences, compositional differences, and the presence of nanophase hematite. Mineralogical compositions of the four samples are shown in Table 6.

The continuity of primary sedimentary features (e.g., bed forms, fine-scale laminations, etc.) above, below, and within VRR demonstrates that the ridge is part of the Murray Fm. mudstone; diagenetic features that define the ridge are seen to crosscut Murray Fm. depositional features. The differences in $FeO_x$ crystallinity, the composition of the X-ray amorphous component, and the overall mineralogy of VRR samples (ST, HF, RH) vs. "typical" Murray Fm. mudstone directly below the ridge (DU) can be used to constrain the nature of the diagenetic event(s). For example, while hematite is known to form in a variety of thermal and chemical environments on Earth and is present in all four samples, its origin can be constrained based on crystallography. The FWHM resolution of CheMin is

~0.35° 2θ, with the result that the Scherrer equation [27] can be used to determine crystallite sizes smaller than about 40 nm [74]. The FWHM of the hematite (110), (104) and (113) peaks in the VRR samples match the 2θ resolution of the instrument so that the crystallite size must be larger than this (and the gray color of the HF sample suggests that there are localized regions of coarse-grained hematite). However, the FWHM of hematite (104) in DU is 0.66° 2θ, yielding a crystallite size of ~18 nm [74]. Szczerba et al. [86] measured the FWHM of hematite diffraction maxima in 20 drilled samples analyzed with CheMin. The smallest crystallite sizes (~3 nm) were found in drilled samples highest in the section (above VRR), while the largest (~40 nm) were in the lower sections (and in VRR, whose crystallites were too large to be measured by line broadening). Figure 21 shows the 2θ region of the DU and HF patterns that contains hematite (104), hematite (110) and hematite (113) maxima. The smaller hematite crystallite sizes in DU and other Murray Fm samples (exclusive of VRR) implies a nanophase precursor (e.g., ferrihydrite or goethite), typically formed at low temperatures. The coarser hematite crystallite sizes in VRR may have been a result of warmer temperatures involving Ostwald ripening and/or the aggregation of smaller hematite particles in saline solutions.

The compositions of the X-ray amorphous components of these samples provide additional evidence: The X-ray amorphous component of DU contains an especially high concentration of $FeO_t$, suggesting the presence of an X-ray amorphous Fe phase such as ferrihydrite. In the VRR samples, Fe in the X-ray amorphous component is more highly correlated with sulfate and elevated $SiO_2$ concentrations. Indeed, in the ST sample, all Fe is taken up in the crystalline component.

Taken together, mineralogical observations within VRR suggest localized post-lithification diagenesis of the Murray sediments involving acidic or high-salinity groundwater fluids with elevated sulfate content [72]. Alternative hypotheses have been presented, for example the interaction of lake waters with sub-surface ground water in the mixing zone prior to lithification [33], or the dissolution of silicate minerals by dense silica-poor brines [32].

### 3.7.2. *Glen Torridon region*

Globally, a wide variety of clay minerals has been identified from orbit in ancient rocks (e.g., [87, 88]. In some occurrences, clay minerals are associated with what are interpreted to be paleosol sequences (ancient soil horizons), for example at Mawrth Vallis (e.g., [89]), or as detrital or authigenic clays in the distal facies of deltaic sediments and lacustrine deposits [90, 91]. Gale crater was chosen as MSL's landing site in part based on orbital IR detections of clay minerals in the Glen Torridon region that were interpreted to be strata-bound deposits of sedimentary origin. CheMin's *in situ* analyses of Gale crater sediments have in fact shown that clay minerals are ubiquitous throughout at least 400 m of sedimentary rock from Yellowknife Bay in the Bradbury Fm. to Glen Torridon in the Murray and Carolyn Shoemaker Fms., all occurring in lacustrine and fluvial mudstones/sandstones. These observations inform and provide ground truth for earlier studies based on orbital infrared imagery and reflectance spectra that proposed multiple hypotheses for clay mineral paragenesis [65, 92].

Curiosity analyzed eight different drill samples from the Glen Torridon region, both in the Murray Fm. and the overlying and conformal Carolyn Shoemaker Fm. (The Carolyn Shoemaker Fm., which first appeared in the GT region is principally a sandstone, interpreted as a higher energy fluvial or near-shore environment relative to the Murray Fm. mudstone. The primary igneous mineralogy, type and amount of clay minerals present, amount and composition of the X-ray amorphous component, etc. are not strikingly different from other samples of the Murray mudstone, with the exception of phases that appear to be the result of late-stage diagenesis, for example hematite, jarosite, and the silica-rich amorphous component found in the Pahrump Hills – Marias Pass region.

Figure 22a shows four representative diffraction patterns of samples from Glen Torridon: Aberlady (AB, sol 2370, elevation -4160 m), Kilmarie (KM, sol 2384, elevation -4160 m), Mary Anning 3 (MA3, sol 2888, elevation -4130 m) and Groken (GR, sol 2912, elevation -4130 m). Figure 22b shows the $2\theta$ region of the (001) clay mineral maximum in these patterns. In addition to the 10Å (001) maximum due to collapsed smectite, an additional sharp maximum at 9.22 Å is seen in the patterns. The CheMin team searched the entire American Mineralogist Crystal Structure Database [94] but did not find a conclusive match, based on both diffraction data and elemental composition. Two hypotheses have been proposed: Bristow et al. [32] hypothesized a mixed-layer serpentine/talc based on extensive modeling (e.g., [32] supplementary materials) and considered it to be sedimentary detritus transported in from the erosion of older bedrock. Thorpe et al. [33] argued that this phase is a mixed-layer clay mineral (greenalite-minnesotaite, G-M) formed *in situ*, a result of the mixing of lake waters with subsurface fluids. Given the low concentration of this phase in Glen Torridon rocks (2.8 wt % in KM), the resolution of these two models will have to rest on sedimentological interpretations, perhaps augmented by future observations. Figure 22c shows the 02*l* region of these patterns, demonstrating that the predominant clay mineral present in Glen Torridon is fully dioctahedral $Fe^{+3}$-rich smectite.

### *3.7.3. Brine-driven Destruction of Clay Minerals in Vera Rubin Ridge*

As described in Section 3.7.1, sedimentological observations during Curiosity's transect through the VRR and GT regions demonstrate that VRR is diagenetically altered Murray Fm. mudstone. Orbital imagery indicates that the Murray Fm. and Carolyn Shoemaker Fm. are conformably overlain by a ~400 m thick Sulfate-Bearing Unit (SBU) characterized as mono- and poly-hydrated magnesium sulfates (e.g., [6, 95]). Magnesium sulfates are highly soluble and the supernatant brines resulting from Mg sulfate deposition would have been dense and silica-poor. Bristow et al. [32] propose a diagenetic mechanism for the local mobilization and recrystallization of iron from clay minerals in VRR, effected by the influx of dense, oxidizing silica-poor brines descending from the overlying sulfate bearing unit. These descending brines would cause local dissolution of clay minerals and other silicates in VRR, leaving Fe-oxides and oxyhydroxides in their place. It follows that this diagenetic event must have occurred prior to lithification of the Murray Fm. sediments since there does not appear to be an unconformity between the Murray/Carolyn Shoemaker Fm. units and the overlying SBU. This mechanism could also explain calcium sulfate veining and secondary crystallization in the lower Murray Fm. below the VRR.

Bristow et al. [32] suggest that top-down diagenesis of clay minerals by dense, silica-poor brines, while rare on Earth, could be widespread on Mars. Orbital observations have shown that sulfate deposits similar to those seen in Gale crater are distributed planet-wide at a time when Mars was experiencing a shrinking hydrological budget and desiccation of the surface environment [87].

### *3.8. Mineralogical Characterization of the Sulfate Bearing Unit*

One of the principal goals of the MSL mission is to investigate the transition from the phyllosilicate-rich strata of the Glen Torridon region to the overlying sulfate-rich strata of the Sulfate Bearing Unit (SBU) identified from orbital IR imagery [6, updated by [95]. This transition has been observed planet-wide in similar-aged terrains and was hypothesized by Bibring et al. [87] to evidence a change in climate from an early, relatively warm and wet Mars to a present-day cold and dry Mars. The juxtaposition of clay mineral, sulfate mineral and oxide mineral strata in sedimentary sequences on a global scale was seen to correlate with a notional understanding of the geological history of the planet ("Phyllosian," loosely correlated with the Noachian, 4.5-3.6 Ga; "Theiikian," loosely correlated with the Hesperian, 3.6-2.6 Ga, and "Siderikian," loosely correlated with the Amazonian, 2.6 Ga – present [5, 87].

### *3.8.1. The Clay Mineral – Sulfate Mineral Transition Region*

The MSL science team studied the sedimentology and geochemistry / mineralogy of rocks in the clay mineral – sulfate mineral transition region between Glen Torridon and the overlying Sulfate Bearing Unit (SBU) from sols 3052 to 3572. Curiosity collected six drill samples in the transition region: Nontron (NT, sol 3056 elevation -4073.5 m), Bardou (BD, sol 3113 elevation -4066.5 m), Pontours (PT, sol 3171 elevation -4041.2 m), Maria Gordon (MG, sol 3232 elevation -4016.1 m), Zechstein (ZE, sol 3229 elevation -3992.0 m), and Avanavero (AV, sol 3517 elevation -3910.0 m). CheMin documented a decrease in clay minerals (indeed, all samples above PT lacked phyllosilicate), and goethite was detected for the first time in NT and increased in concentration from NT to AV. These mineralogical changes are proposed to be the result of a change from fluvial/lacustrine conditions to dry, aeolian conditions [96].

### *3.8.2. The Sulfate Bearing Unit*

Curiosity is now investigating sulfate-bearing mudstones and sandstones of the SBU. The hydrated magnesium sulfate mineral starkeyite (the four-hydrate of $MgSO_4$) was first identified in the drill sample Canaima (CA, sol 3614 elevation -3879 m) from an aeolian sandstone (Figure 23). Table 7 lists the eight known crystalline Mg-sulfate hydrate minerals, in addition to amorphous $MgSO_4$ (Am-$MgSO_4$). The overall mineralogical composition of CA is shown in Table 8. While the measured amount of starkeyite is low (2.3 wt.% of the total), the sample contains 62% X-ray amorphous material, with the result that starkeyite comprises 8.2% of the crystalline phases present. In the 2nd and 3rd analyses (2 and 12 sols respectively after the first analysis), starkeyite is below CheMin's detection limit (<~0.3 wt %). For the duration of the analysis of CA, the temperature inside the rover body (and inside CheMin) varied from ~6-30° C resulting in a relative humidity (RH) <<0.1% [97]. It is known from experimental studies that many hydrated Mg sulfates lose their waters of hydration, and some revert to an amorphous state under these conditions [98-103]. Gypsum ($CaSO_4{\cdot}2H_2O$) is also seen to decrease with a concomitant increase in bassanite ($CaSO_4{\cdot}0.5H_2O$). This has been observed in previous samples that contain gypsum, and is described in [104, 105]. Rhyolitic glass and Am-$MgSO_4$ were found to best fit the broad mid-range maximum in the pattern, but basaltic glass could also be present, since it has a scattering distribution similar to Am-$MgSO_4$. Disordered silicates (palagonite, allophane and ferrihydrite) were used to fit the low $2\theta$ (<10°) rise in the pattern. Chipera et al. [97] supported this diffraction-based result using mass balance calculations [40] from full-pattern fitting analysis of CheMin mineralogical data using FULLPAT [36, 37] (method fully described in [97] supplementary materials), bulk compositional data measured by APXS [12, 106], and water content from ChemCam [107] i.e., see Table 9. Elevated MgO and $SO_3$ in the amorphous component strongly suggest that Am-$MgSO_4$ is present, with a calculated maximum abundance of ~28 wt%. The first night's analysis of the CA sample occurred after half of a diurnal temperature cycle, and it is likely that the starkeyite abundance was in fact higher, some having reacted to Am-$MgSO_4$ inside the rover before the first analysis was conducted [97].

At summer daytime temperatures on Mars, when the RH remains below a few %, it is likely that starkeyite will transform to Am-$MgSO_4$. At lower temperatures (and higher humidity) such as nighttime and winter conditions, both starkeyite and Am-$MgSO_4$ will be metastable, but the kinetics of transformation to more stable higher-hydrates are sluggish [103]. Starkeyite and Am-$MgSO_4$ will persist for durations longer than a Mars year and are the expected phases on the surface of Mars (see, for example Figure 8 of [97]. Kieserite, the one-hydrate of $MgSO_4$ has been identified from orbit and has also been directly detected by CheMin in Tapo Caparo (TC, sol 3755, elevation -3880 m). The detection of kieserite is puzzling since it should only form at temperatures above 50° C; further analyses as Curiosity continues to climb the lower elevations of Mt. Sharp could provide some clues to its origin.

Mg sulfate hydrates are sensitive environmental indicators. The first Mg sulfate hydrate to form from a concentrated aqueous solution is either meridianiite or epsomite, depending on temperature [97] and would dehydrate stepwise under warmer and drier conditions to produce starkeyite. The Martian environment(s) under which these higher hydrates of $MgSO_4$ were initially deposited (playa lake, efflorescence from subsurface brine, etc.) are not presently known because none of the detected sulfates appear to be primary. Once formed, aeolian weathering could have redeposited the sulfates in the sandstone sampled at Canaima. Mg sulfates are highly soluble; since the eolian sandstone hosting the sulfates is cemented, there must have been a cycle of wetting, drying and cementation prior to the emplacement of the sulfates in their present form.

### *3.9. The Ubiquitous Amorphous Component*

The aqueous dissolution of olivine, pyroxene and basaltic glass should have resulted in significant quantities of amorphous silica (e.g., opal-A) on an early warm and wet Mars [108]. This was validated when opaline silica was discovered by the MER rover Spirit at Meridian Planum in concentrations as high as 20% [109], by the MER rover Opportunity in Gusev Crater [110], and in a variety of locations from visible/near IR orbital data (e.g., [111]). However, it is enigmatic that amorphous materials are seen to persist in 3-3.5 Ga regolith on Mars, since in terrestrial settings, amorphous silica is uncommon in rocks more than a few million years old (e.g., [112]). Tosca and Knoll, (2009) [113] discuss "juvenile precipitates" – precipitates that have undergone little diagenetic modification since their formation on Mars and conclude that the anomalous preservation of silica could result from a water-limited environment following their deposition, or from differences in the styles of tectonism and sedimentation between Earth and Mars.

Curiosity's discovery that nearly all the ~3.5 Ga old sedimentary rocks analyzed to date at Gale Crater contain 15-70 wt.% X-ray amorphous material (e.g., [22, 30, 41, 44, 74, 85, 114-117] only deepens this mystery. These amorphous materials could be glassy materials in the true sense, such as basaltic glass, or nanophase materials having only short-range order. Calculations of the quantity and composition of amorphous components using full pattern fitting (FULLPAT; [36]) and mass balance equations [40] introduce systemic inaccuracies that can affect the resulting values to some extent; nevertheless, ancient amorphous materials appear to be both abundant and ubiquitous on Mars.

The calculated compositions of the amorphous components in Mars soil, and Bradbury Fm., Murray Fm., altered Murray Fm., Stimson Fm, altered Stimson Fm. and Sulfate Bearing Unit (SBU) rocks exhibit distinct differences both within and between formations and lithologic units [97, 116, 118]. The major chemical species common to all amorphous components are $FeO_t$, $SiO_2$ and $SO_3$. Smith et al. [116] calculate the mixing relationship between $FeO_t$ and $SiO_2$ and conclude that the hypothetical compositional endmembers are inconsistent with a volcanic or impact glass origin – they must therefore be the result of aqueous processes. This conclusion is supported by SAM-EGA data in which the volatile release temperatures of $H_2O$ and $SO_2$ indicate that they are associated with the amorphous component (e.g., [60, 119]). Cross-cutting relationships between stratigraphic units suggest that the most $SiO_2$ rich amorphous components result from interactions with localized fluids during late diagenesis. Low to moderate silica enrichments occurred during sediment deposition or early diagenesis. Table 10 lists the compositions of amorphous components in a representative sampling of rocks analyzed by *Curiosity*.

Smith et al., [116] speculates that on Earth, amorphous materials are less likely to accumulate in the source-to-sink sedimentary rock cycle and are less likely to persist after burial (a consequence of plate tectonics). On Mars, conditions that existed during the deposition and diagenesis of amorphous materials appear to be more permissive of their accumulation and preservation. However, the preservation of these amorphous materials for more than 3.5 Ga, a phenomenon unknown in terrestrial settings, remains a mystery.

Smith et al. [118] explore the nature of the amorphous sulfur-bearing phases in Murray Fm. sedimentary rocks. These authors report that 20 to 90% of the $SO_3$ resides in the amorphous component, consistent with Mg-S, Fe-S and possibly Ca-S phases. The SAM evolved gas analyzer (EGA) detects $SO_2$ with release temperatures and peak shapes consistent with Fe- and Mg-sulfur bearing materials in most rocks analyzed prior to Curiosity's arrival at the Sulfate Bearing Unit. Vaniman et al. [104] have shown that Gypsum transforms to Bassanite in the low RH environment of the CheMin instrument over a period of several sols, and Chipera et al. [97] have shown that Starkeyite ($MgSO_4 \cdot 4H_2O$) transforms to amorphous $MgSO_4 \cdot nH_2O$ in a matter of a few hours. Smith et al. [118] argue that the amorphous sulfur-bearing phase(s) were likely crystalline and became amorphous through dehydration in either the current Martian atmosphere or inside the CheMin instrument. The fact that CheMin did not detect these phases means that they are either below CheMin's detection limit (~1%), they were originally X-ray amorphous, or they became X-ray amorphous inside Curiosity prior to analysis by CheMin.

### *4.0. Discussion and Conclusions*

As the first *in situ* crystallography instrument sent to another planet, CheMin has been responsible for a number of discoveries, many of which are described in Section 3. Three that are particularly noteworthy are highlighted below:

1. Discovery and characterization of habitable environments on early Mars: This was one of the principal goals of the MSL mission and was achieved with the first drilled sample at Yellowknife Bay. Requirements for habitability ("life as we know it") include a source of the biogenic elements (H, C, O, N, P, S), a source of energy (minerals with variable redox states), high to moderate water activity, moderate temperatures and moderate to neutral pH. A surprising discovery is that through hundreds of meters of lacustrine mudstones, corresponding to 100's of thousands to millions of years [75], these requirements are satisfied, suggesting that habitable environments were common on early Mars. Mineralogical data are critical to the discovery and characterization of ancient habitable environments, and provide context for the morphologic, isotopic, and chemical data used to evaluate putative evidence of biogenicity. Equally important; post-depositional conditions of pressure, temperature, and chemical composition (P, T, X) – determined with a knowledge of the assemblage of minerals and mineral stability ranges - can through their actions preserve evidence of habitability or erase such evidence entirely.

2. The paragenesis of clay minerals: Prior to Curiosity's arrival in Gale crater, the paragenesis of clay minerals identified from orbital near-infrared reflectance spectra was poorly understood [5, 6, 65, 120]. CheMin mineralogical results in combination with sedimentological observations demonstrate that (in all but two cases, whose origin is a matter of debate) the trioctahedral and dioctahedral smectites found were either authigenic or early diagenetic, formed in place in the sediments. CheMin data provided the ground truth for the orbital clay mineral detections at Glen Torridon, but clay minerals are also found in many areas in Gale crater traversed by *Curiosity* that do not exhibit clay mineral signatures in orbital data.

3. The ubiquitous presence of X-ray amorphous material in Gale crater sedimentary rocks: X-ray amorphous materials, whether they are glasses in the true sense, or nanophase materials that lack long-range order, are found throughout Gale crater's sedimentary rocks. The discovery of amorphous materials in ~3.5 Ga on rocks Mars is confounding, given that amorphous materials, inherently unstable, should crystallize in geologically short time periods. The amount and the elemental chemistry of the amorphous components vary in ways that suggest that they are the product of diagenetic events unique to the formations in which they are found.

In the nearly twelve years that Curiosity has been investigating Gale crater, the MSL science team has studied and documented over 800 vertical meters of flat-lying strata deposited and diagenetically altered on lower Mt. Sharp (e.g., Figure 10 and [75]). The sedimentology of these rocks reveals what in effect constituted the rock cycle on early Mars: in the absence of plate tectonics, sediments were deposited in fluvial, lacustrine and aeolian environments, diagenetically altered and lithified. Subsequent exhumation / erosion by aeolian forces was followed by the deposition of younger sediments which themselves were diagenetically altered, lithified, and eroded [82].

There is uncertainty as to the timing, quantity and mechanism(s) of sediment infilling of Gale crater. Malin and Edgett [4], and Day and Kocurek [121] suggest that the crater had been completely infilled with sediment and later partially exhumed by aeolian forces. Kite et al. [122] propose a model in which the central mound of Gale was the result of aeolian infilling, achieving the approximate shape and size that it is today. This result is supported by the measurement of shallow dips (~3°) of sedimentary layers in directions away from the mound center, suggesting that there were 3 to 4 km of pre-erosional stratigraphic relief in the mound. Borlina et al., [123] utilize predicted thermal gradients and patterns of diagenesis (e.g., lack of evidence of the smectite to illite transition) to suggest that Yellowknife Bay sediments were never buried deeper than ~2 km. However, because the timing of the deposition of Yellowknife Bay sediments is not known with certainty, they could post-date the deposition of Mt. Sharp sediments. Lewis et al. [124] utilized accelerometers on the rover to measure the density of the sedimentary rock in lower Mt. Sharp and compared this result to calculated rock density based on CheMin mineralogy. These authors calculated a porosity of 40 ± 6%, and estimated from this measurement that the upper limit of burial of these sediments was 1600 - 1800 m.

Palucis et al. [125] describe the physical sedimentology of Gale crater using orbital HiRISE (High Resolution Imaging Science Experiment) topographic data. These authors propose that there were at least three major lake stands within Gale crater, each persisting for perhaps $10^4$ to $10^5$ Earth years – all of which occurred after Mt. Sharp had attained its present size and approximate shape. The location and elevation of alluvial fans and deltas originating from the crater rim and from Mt. Sharp suggest that these lakes were as much as 700 meters deep, covering the lower flank of Mt. Sharp and much of the stratigraphy traversed by Curiosity. The absolute ages of the lakes and the depositional events associated with them are not known with certainty, since many of the features are too small for crater counting to be useful. From [125] and references therein, the age of Gale crater is estimated to be ~3.8 to ~3.5 Ga, the age of the deposition of Mt. Sharp sediments and their subsequent erosion ~3.5 to ~3.1 Ga, and the age of deposition of the lacustrine, fluvial and aeolian sediments traversed by Curiosity ~3.3 to 3.2 Ga. The timing of two events known with more certainty are the formation age of the detrital minerals in basaltic sediments of the Yellowknife Bay Fm. (4.21 ± 0.35 Ga, [64]) and the diagenetic age of jarosite in the Murray Fm. (2.12 ± 0.36 Ga, [79]). The latter suggests that subsurface aqueous diagenesis persisted (or recurred) for ~0.5 Ga after the last lake system dried up. Taken together, one can conclude that aqueous habitable environments (confirmed with mineralogical data) existed for hundreds of millions of years, at a time when evidence for primitive microbial life is found in rocks of equivalent age on Earth.

Given the complex depositional and diagenetic history of the sedimentary rocks traversed by Curiosity, it is perhaps not surprising that multiple and sometimes conflicting hypotheses have been put forward to explain the same observations. Nevertheless, there is no evidence that the sediments were ever deeply buried or extensively heated, and in many cases, primary sedimentary structures and original mineralogy remain. By way of comparison: as a consequence of plate tectonics, nearly all terrestrial rocks of this age have either been subducted and destroyed, or metamorphically altered to the extent that little evidence remains of their provenance. Early Mars acts as a surrogate for early Earth in this regard, in the study of environments habitable for, and perhaps inhabited by, early life.

In the solar system, Mars is the only planet (other than Earth) that can be studied in this way. Of the other terrestrial planets, Venus has a surface temperature of ~470 C with the result that any early sedimentary record would have been highly altered. In addition, Venus has been extensively resurfaced so that no heavily cratered (i.e., ancient and unaltered) surfaces remain. The planet Mercury is a geochemical end member among the terrestrial planets, whose surface temperature varies from 430 C to -180 C. Little is known of the mineralogy of Mercury because the surface lacks diagnostic spectral absorption features in the UV-VIS region and spacecraft have never landed there. While future robotic missions are envisioned to each of these planets in the coming decades [126], they will be relatively short-lived landers (not rovers) and the ability to make scientific observations will be limited by the extremes of the environments.

Hazen et al. [127] summarize what is currently known about the diversity and formation modes of Martian minerals and make comparison to the mineral diversity and mineral formation modes of Earth (e.g., [128, 129] and references therein). The Martian data set includes results from both orbital and landed in-situ observations and measurements from Martian meteorites. These authors conclude that the total mineral diversity of Mars is an order of magnitude less than that of the Earth, largely due to the absence of plate tectonics on Mars, and the presence of biologically mediated mineralization on the Earth.

Curiosity's *in-situ* mineralogical analyses with CheMin have shown a wealth of detail not seen from orbit, and future missions of this type would undoubtedly provide more insights into Martian mineral diversity and mineral paragenetic modes. Dozens of geologically diverse and scientifically compelling landing sites have been identified and characterized from orbit as a result of the MER, MSL, and Mars 2020 site selection workshops [130-132]. To characterize the full mineralogical diversity of Mars, its early habitability, and its potential to support *in-situ* resource utilization (ISRU) and eventual human exploration, comprehensive *in-situ* science investigations are required at many diverse sites. A follow-on landed mission to Mars, the Mars 2020 Perseverance rover, arrived in Jezero crater in Feb. 2021 [133]. Perseverance is characterizing and collecting samples of rock and regolith for possible return to Earth. The next proposed *in-situ* mission to Mars is the Mars Life Explorer (MLE), a lander intended to drill and analyze a 2-meter-long core of rock. CheMinX, a next generation powder XRD, is included in the strawman payload of that mission [134, 135].

For the next several decades, pending NASA approval of the MLE mission or Mars Sample Return, CheMin data from MSL Curiosity will be the only *in-situ* quantitative mineralogy available from Mars. CheMin data are archived at the Planetary Data System Geosciences Node (**https://pds-geosciences.wustl.edu/missions/msl/chemin.htm**) as are SAM data (**https://pds-geosciences.wustl.edu/missions/msl/sam.htm**), APXS data (**https://pds-geosciences.wustl.edu/missions/msl/apxs.htm**) and data from the other MSL Curiosity instruments. The "Gale Crater Mineralogy and Geochemistry Sample Database" [19] is a living repository of CheMin, SAM and APXS data for each analyzed sample, from which all raw data, sample descriptions, on-line analysis tools and open access publications from the CheMin team can be downloaded. Figure 24 shows a screenshot of two data fields from a single CheMin data record. QAnalyze (**https://www.qanalyze.com/**) is a cloud-based whole pattern fitting program that can be selected from within each data record or accessed as a standalone application. If chosen from within the database, QAnalyze will uplink the X-ray diffraction pattern for that sample as well as the list of the CheMin team's preferred AMCSD phases chosen for that analysis. The program returns whole pattern fitting results, refined lattice parameters for each mineral, and allows the user to add or subtract phases from the AMCSD database to try to improve the fit.

MSL Curiosity will continue to climb Mt. Sharp for the coming Mars year (equivalent to about two Earth years) and perhaps longer, and we anticipate that there will be eight (or more) additional drilled sample analyses prior to mission's end. Orbital images show that many interesting features remain to be examined in detail on Curiosity's journey. One of Curiosity's ultimate goals is a feature identified in orbital images called the "boxwork structure" [3, 136] comprised of decameter-scale polygonal ridges that appear to be early diagenetic features formed in a subsurface phreatic groundwater zone [137]. The ridges in the boxwork structure, which are on average 5 m in width are cemented fracture systems that are more resistant to erosion than the surrounding rock. The boxwork structures are exposed at an elevation of -3620 ± 50 m and extend along bedding for at least 10 km at this elevation [137]. These structures could be a "Rosetta Stone" for deciphering the late-stage groundwater activity in Gale crater and globally, providing deeper insight into the geology and conditions of habitability of early Mars.

The diffraction geometry of the CheMin instrument is identical to that used by Max von Laue in his discovery of the nature of X-rays and their diffraction by crystals more than a century ago. One could imagine that Dr. von Laue would be pleased (and very surprised!) by how far his discovery has taken us.

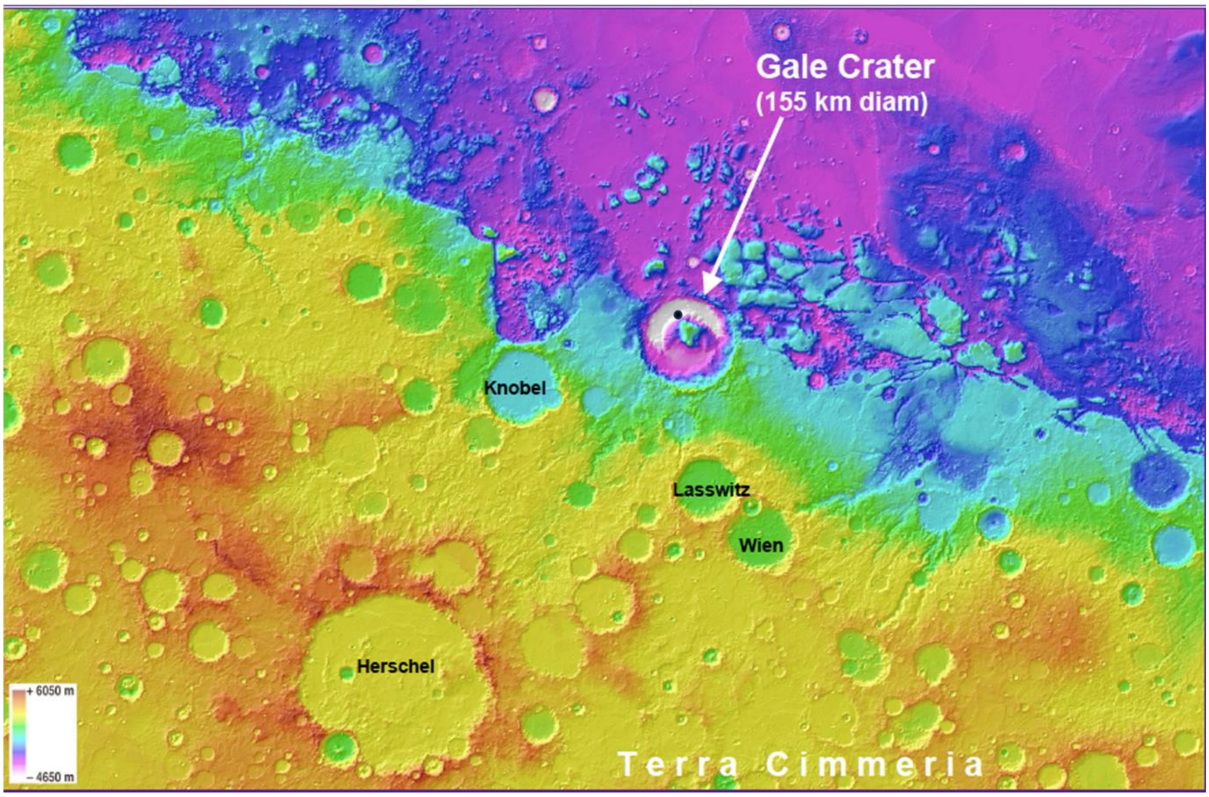

**Figure 1.** Color-coded topographic map of Gale crater, located near the Mars equator and sitting astride the Mars dichotomy boundary. The floor of the crater is -4650 m relative to the Mars datum (average elevation on Mars). MSL-Curiosity landed in the white area north of the central mound. A black dot marks the approximate position of the landing site.

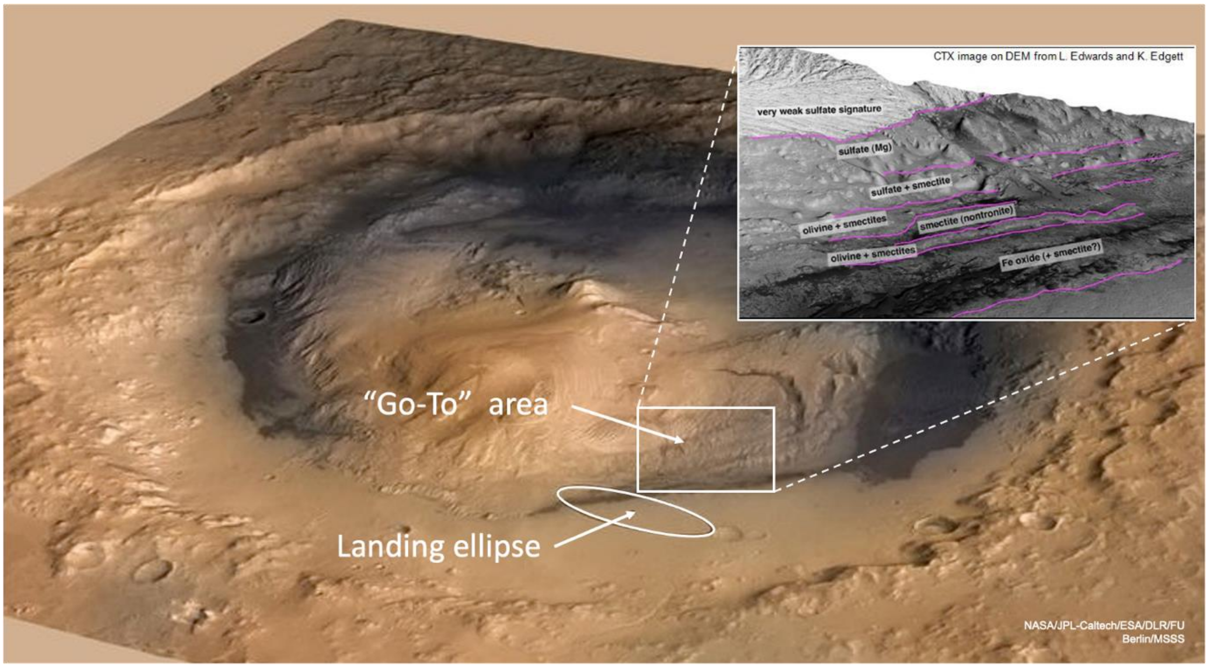

**Figure 2.** Oblique view, looking down on Gale crater from the North. The landing ellipse is 20 x 6 km and represents the predicted landing area (Curiosity landed within 2 km of the center of the ellipse). While several CheMin analyses were performed within the landing ellipse, the rectangle south and west of the site shows the area of most interest during the mission, and the inset shows the mineral signals as seen from orbit.

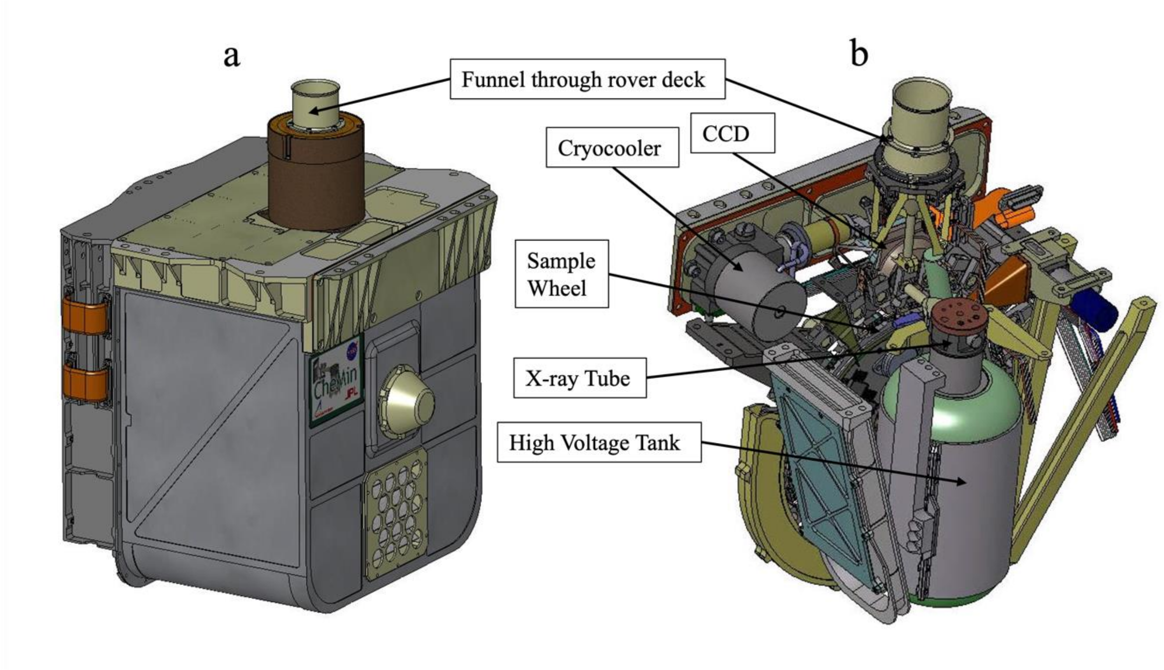

**Figure 3.** The CheMin XRD/XRF instrument, 30x30x30 cm, 10 kg. (a). The SA/SPaH delivers a sieved aliquot of powdered rock or soil through the funnel located at the top of the instrument, which penetrates the upper deck of the rover. (b). Internal components of the instrument (the image is rotated 180° about the vertical axis from (a) for clarity).

1112

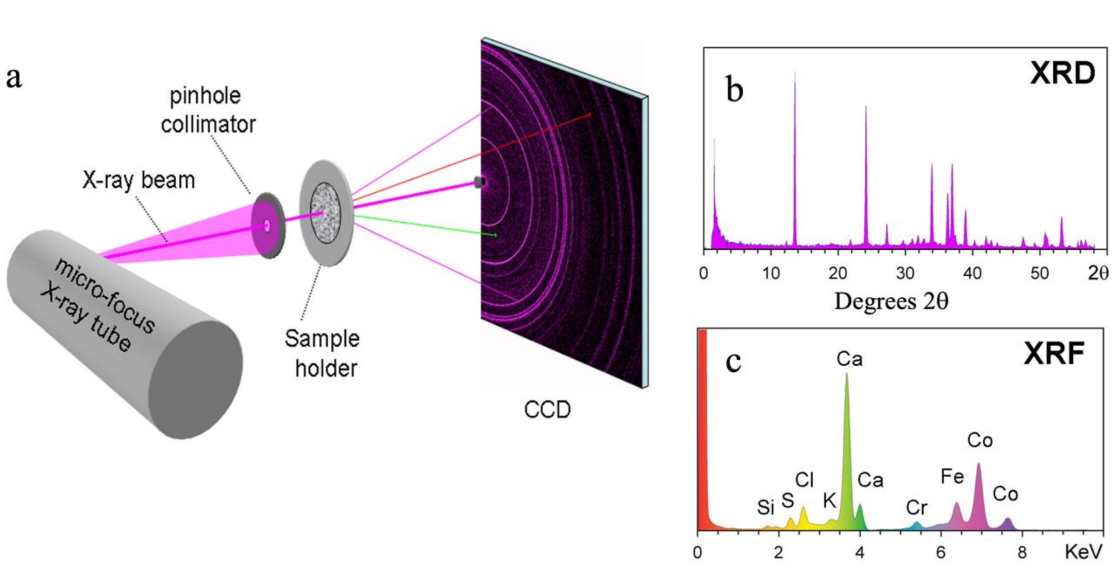

1113

**Figure 4.** Geometry of the CheMin instrument. (a). Overall geometry of CheMin. (b). XRD 2θ plot obtained by summing diffracted photons from the characteristic Kα line of the X-ray source (CoKα X-rays colored magenta in (a). (c). X-ray energy-dispersive histogram (EDH) obtained by summing all X-ray photons detected by the CCD, with fluoresced photons from the sample shown schematically in green and red in (a). 1114 1115 1116 1117 1118

1119

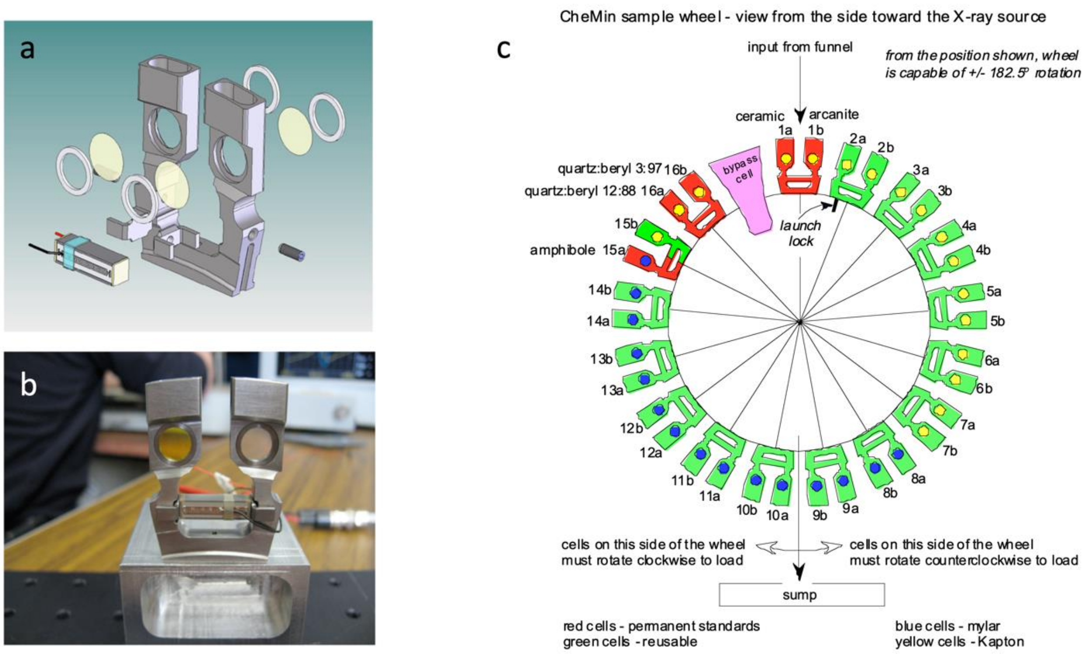

**Figure 5.** CheMin cell geometry. (a). Exploded view of dual-cell assembly, showing windows, tuning-fork assembly and piezodriver. (b). Assembled cell, ready for testing (Yellow Kapton window on left, clear mylar window on right). (c). The CheMin sample wheel, showing the location of sealed standard cells and open cells used for powder samples delivered by the SA/SPaH system. The cells are filled and analyzed at the top, then rotated 180° and emptied into a sump at the bottom of the instrument.

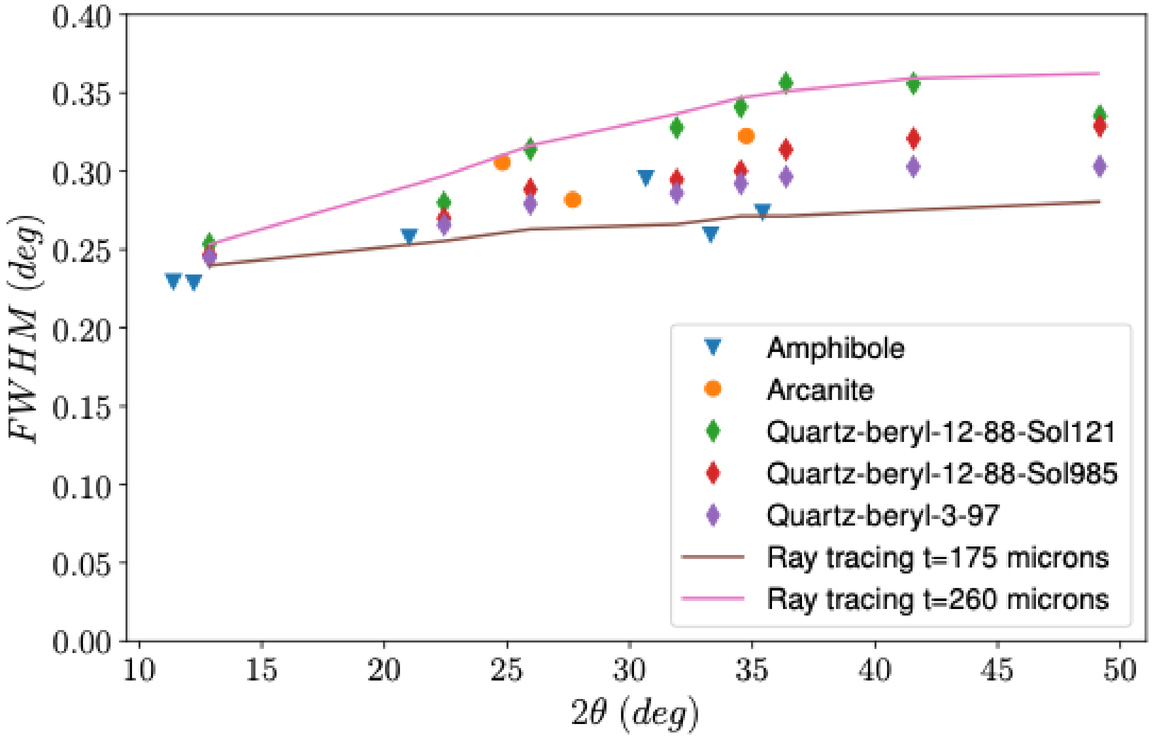

**Figure 6.** Measured FWHM peak widths for CheMin's five standards (symbols) vs. ray-tracing results for 175 µm and 260 µm sample widths that best bracket the measured data. Cell windows are mounted on either side of a 170 µm spacer in the cell, yielding a nominal sample thickness of 170 µm. However, piezovibration during analysis causes the windows beat like a drum, which increases the effective sample thickness in some cases.

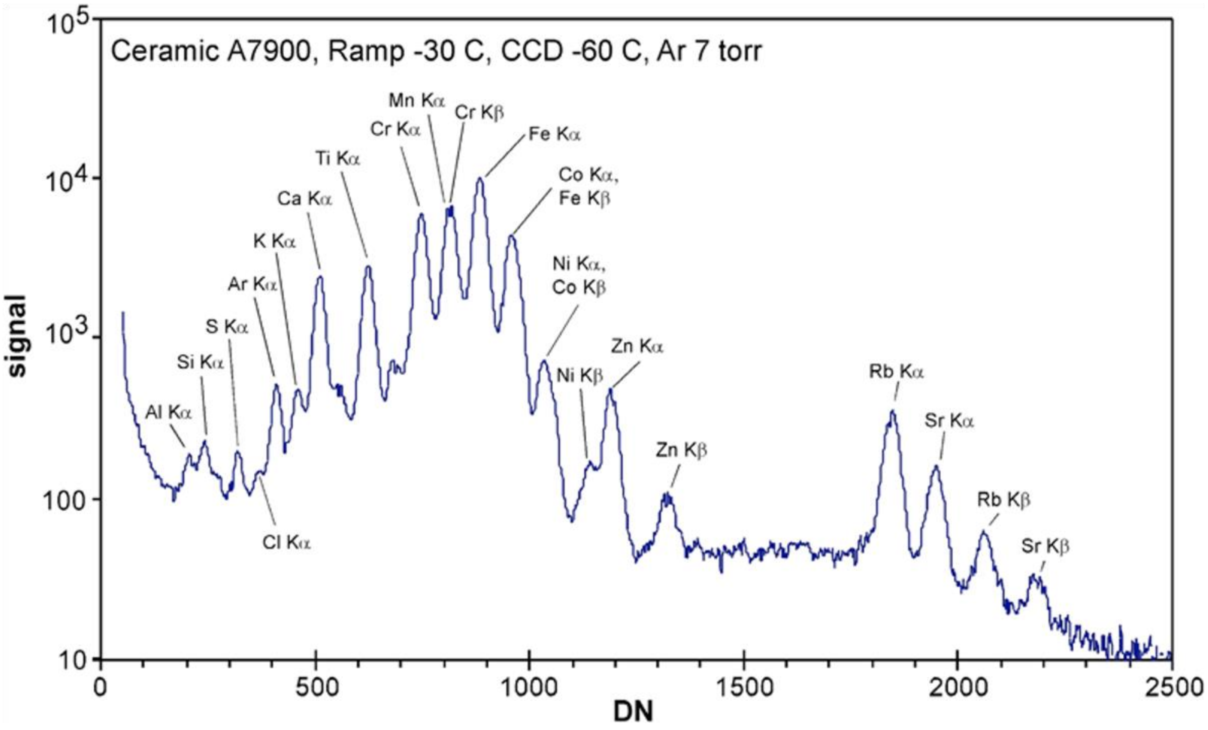

**Figure 7.** Energy-dispersive histogram (EDH) of the ceramic standard analyzed during Cryo-Vac testing of the CheMin instrument on Earth. RAMP (Rover Avionics Mounting Platform) held at -30° C and CCD at -60° C, 7 torr of Argon used to simulate the Mars atmosphere.

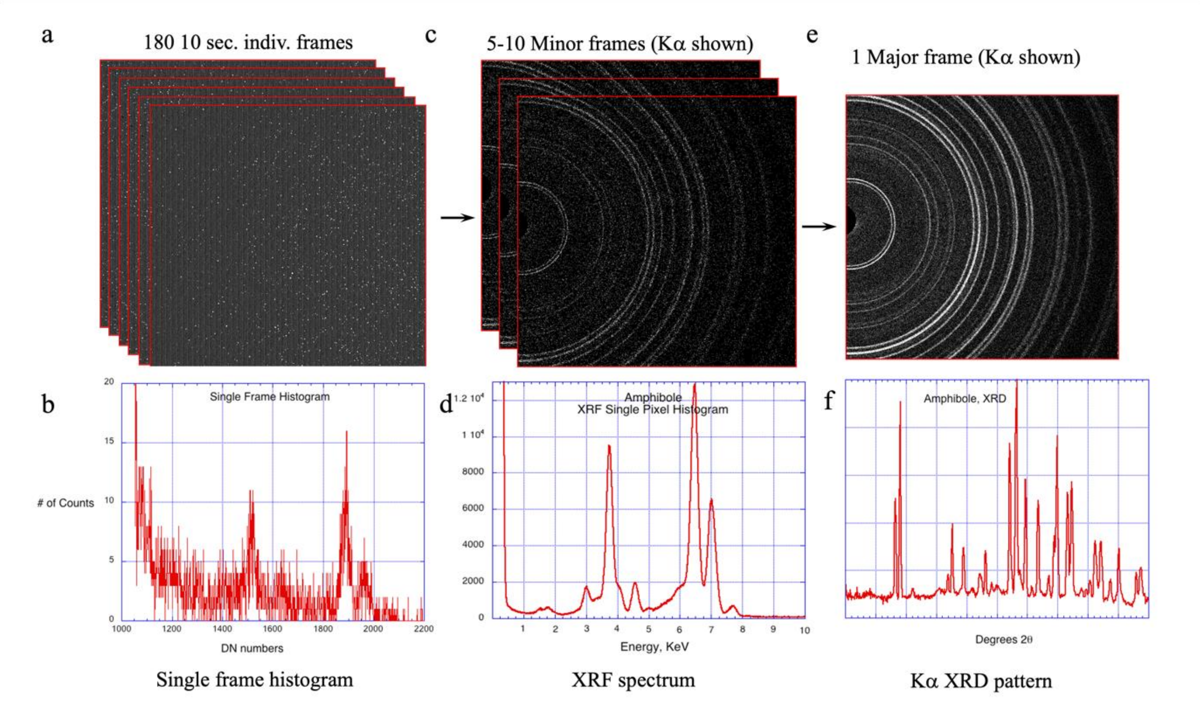

**Figure 8.** 2D diffractograms of the Gore Mountain amphibole standard (analyzed during CryoVac testing of the CheMin instrument on Earth. (a). Stack of 180 individual 10 second frames of data. (b). EDH from a single 10-second frame of data. (c). Stack of 10 minor frames of energy selected CoKα data. (d). XRF spectrum from 10 minor frames of data. (e). Major frame of 10 summed minor frames of energy selected CoKα data. (f). 1D diffractogram from (e).

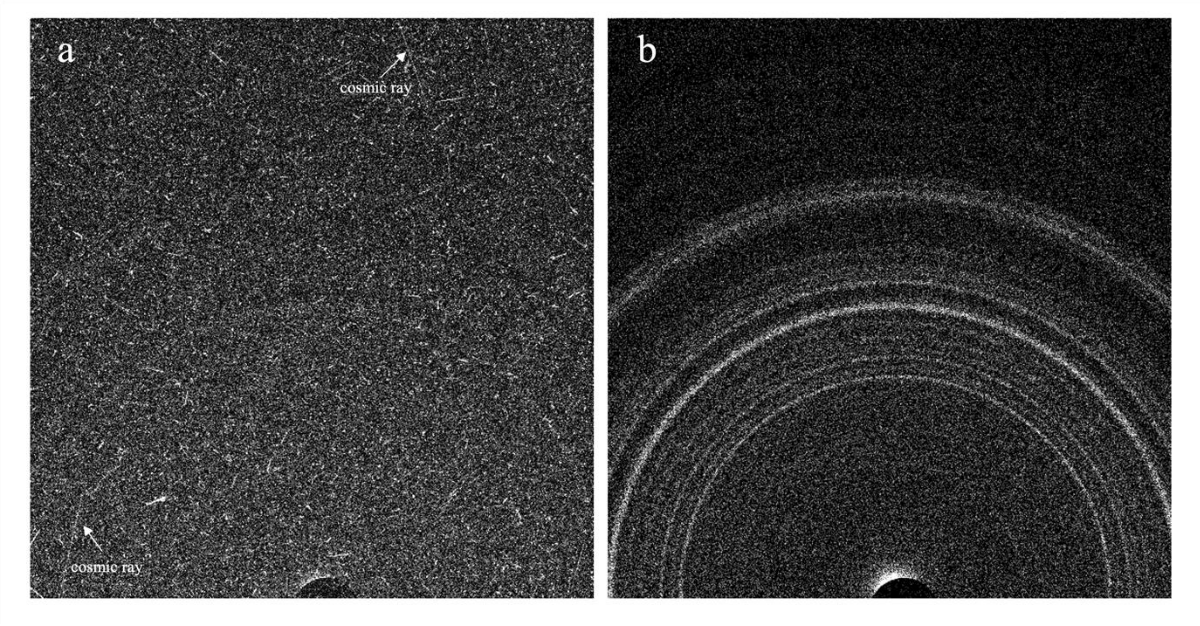

**Figure 9.** Comparison of Film mode vs. energy selected CoKα mode CheMin 2D data. (a) Minor frame (sum of 180 10-second images) of raw energy data. (b). Sum of 6 minor frames of energy selected CoKα data.

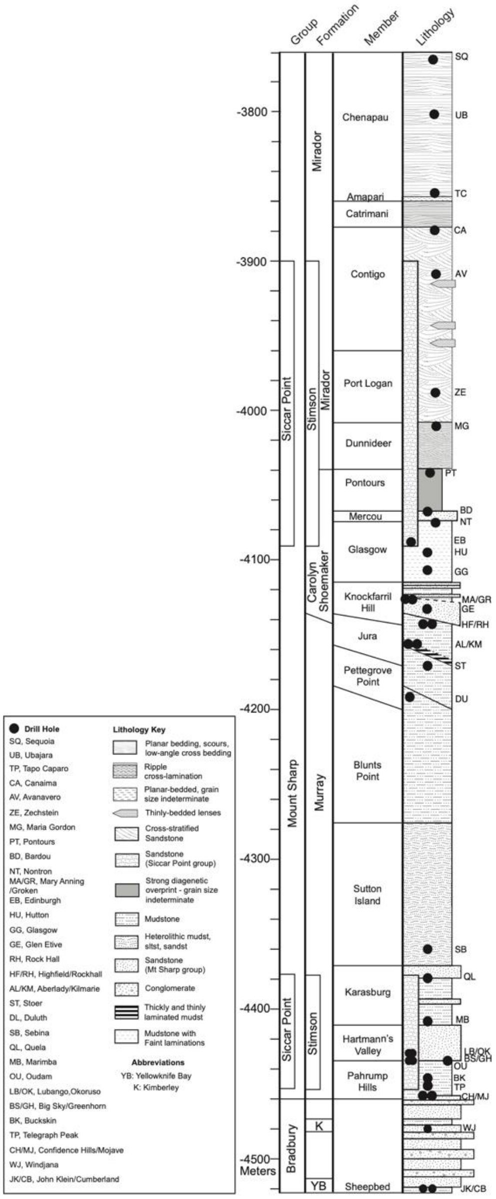

**Figure 10.** Stratigraphic column of units investigated by Curiosity from Yellowknife Bay to the Sulfate Bearing Unit. Black dots denote drilled samples (Table S-1 lists the attributes of all samples analyzed to date). Figure credit: the MSL sedimentology and stratigraphy working group.

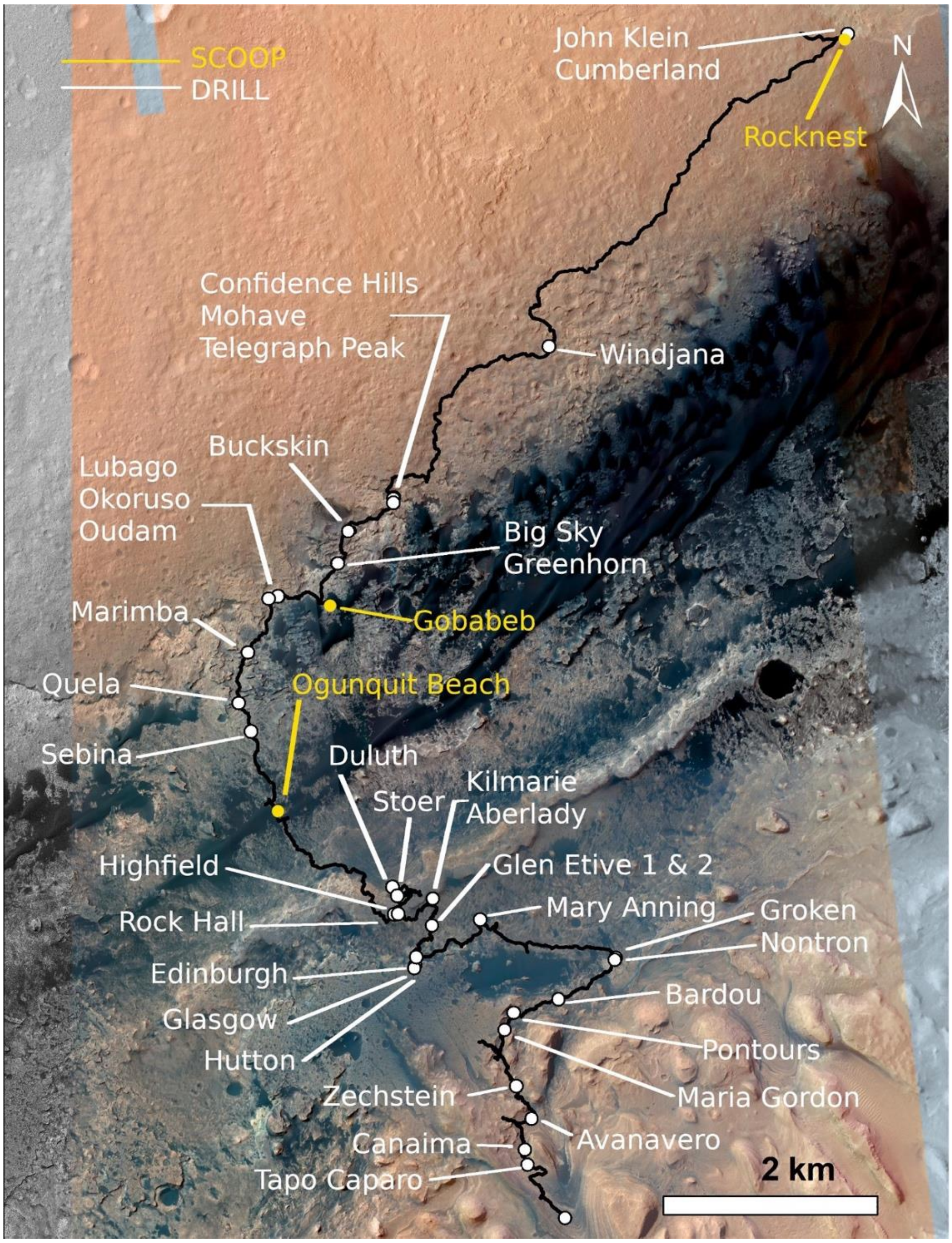

**Figure 11.** Plan view of Curiosity's 12-year journey across Gale crater. Drilled rock samples are shown in white, scooped aeolian soil samples are shown in yellow.

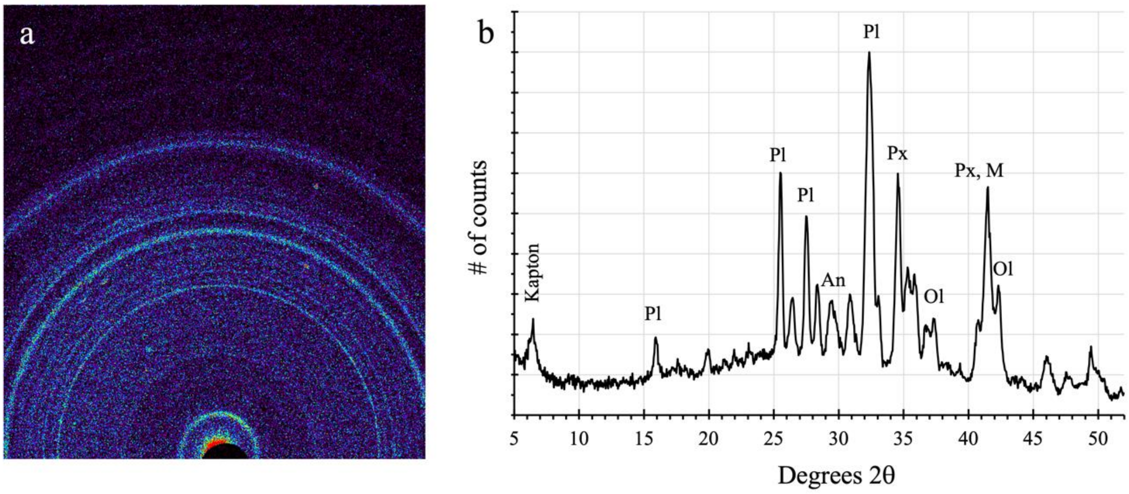

**Figure 12.** First X-ray diffraction pattern to be returned from Mars. (a). colorized 2-D pattern. (b). 1-D pattern obtained from (a), most intense peaks of major minerals shown (Pl = plagioclase feldspar, An = anhydrite, Px = pyroxene, Ol = olivine, M = magnetite).

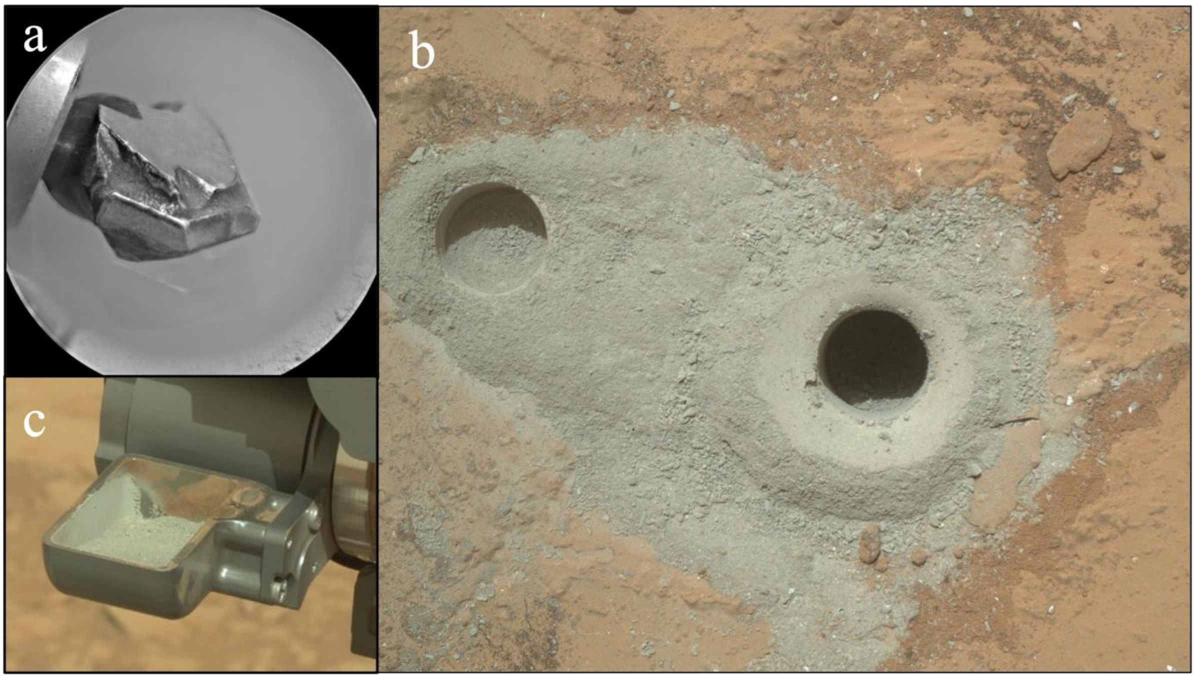

**Figure 13.** (a). Percussion drill bit used to drill and collect samples (16 mm dia.). Powdered material is retained in the drill stem and transferred to the SA/SPaH system for sieving. (b). Image of shallow (1 cm deep) test drill hole (left) and the sampled drill hole (6.5 cm deep) from John Klein. (c). John Klein drill sample in the scoop reservoir before sieving to <150 µm (note red residue powder in the scoop which is contamination from the previous sample (Rocknest)). The delivered samples typically contain ~3% contamination from the previously drilled sample [30].

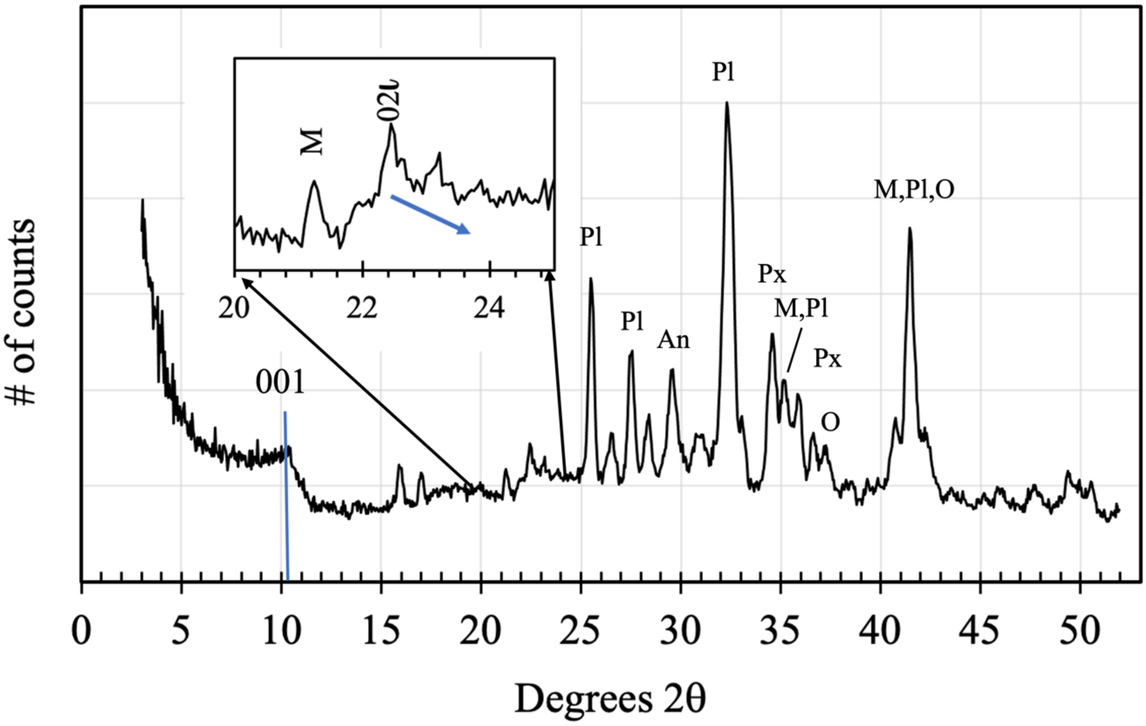

**Figure 14.** Diffraction pattern of John Klein, showing the position of the (001) reflection of smectite. Inset: portion of the pattern that contains the (02*l*) diffraction band of smectite. The maximum at 22.5° 2θ indicates that the clay mineral is trioctahedral. Blue arrow denotes the turbostratic nature of the 02*l* band, extending beyond the band maximum. Phase assignments labeled for major peaks (Pl = plagioclase feldspar, An = anhydrite, Px = pyroxene, M = magnetite, Ol = olivine) (redrawn from [28] and [30]).

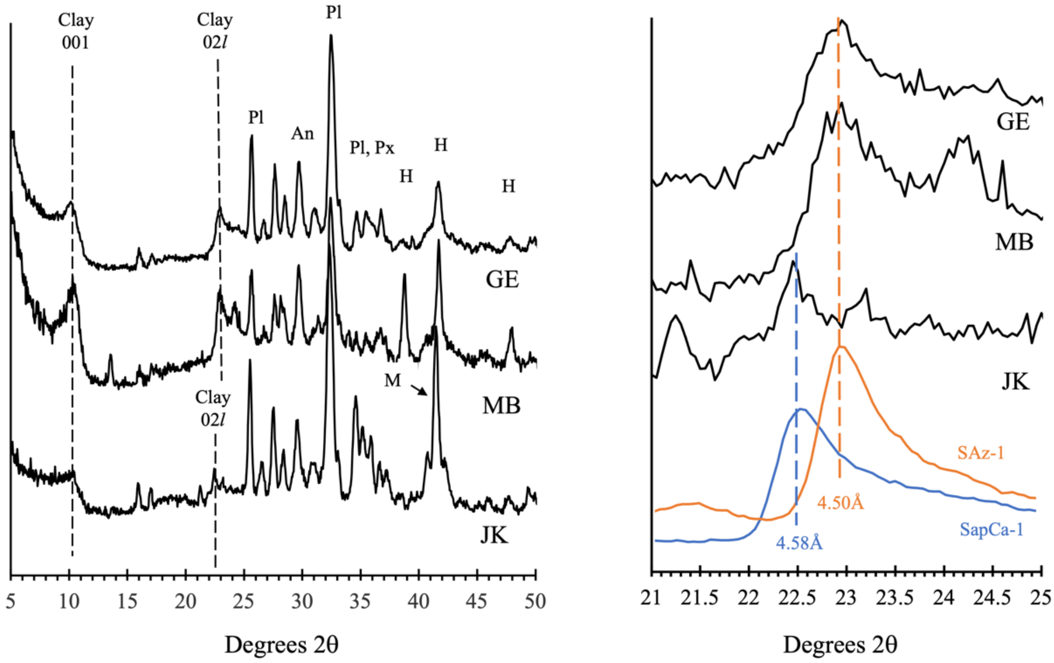

**Figure 15.** Diffraction patterns of John Klein, Marimba and Glen Etive 2, showing transition from trioctahedral smectite to dioctahedral smectite. (a). Overall diffraction patterns showing clay mineral (001) reflection and 02*l* diffraction band. Major mineral peaks labelled (Pl = plagioclase feldspar, An = anhydrite, Px = pyroxene, M = magnetite, H = hematite). b). 21° to 25° 2θ region of the pattern, showing transition from trioctahedral to dioctahedral occupancy. Clay mineral standards SAz-1 (dioctahedral) and SapCa-1(trioctahedral) shown for comparison.

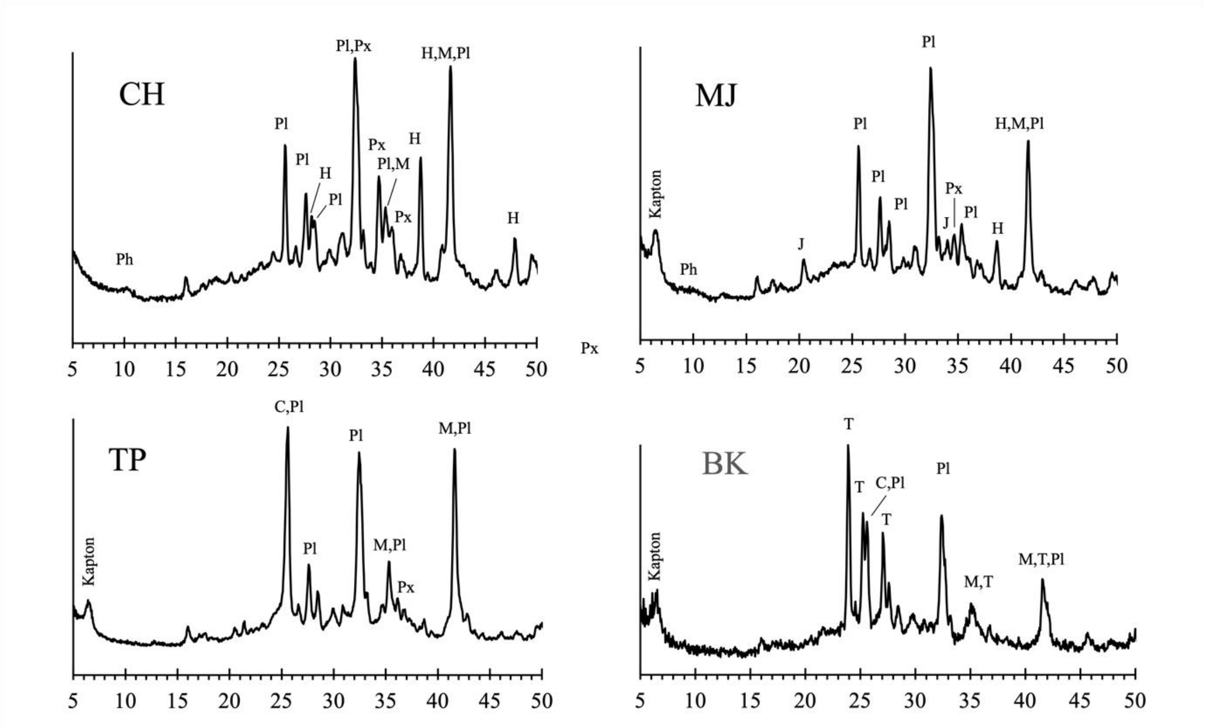

**Figure 16.** CheMin 1-D X-ray diffraction patterns of drill samples Cumberland Hills (CH), Mojave (MJ), Telegraph Peak (TP) and Buckskin (BK) from the lower Murray formation. Major peaks are labelled (C = cristobalite, H = hematite, J = jarosite, M = magnetite, Ph = phyllosilicate, Pl = plagioclase, Px = pyroxene, T = tridymite).

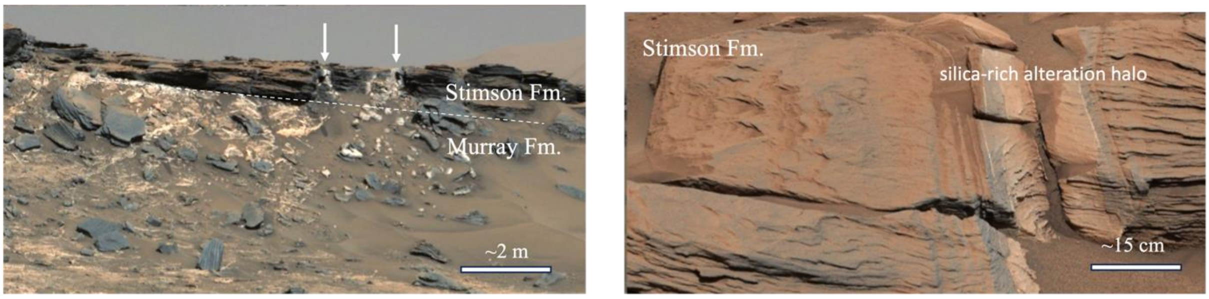

**Figure 17.** (a). MastCam image of the disconformal boundary between Murray Fm. mudstone (lower slope-forming unit) and Stimson Fm. aeolian sandstone (upper cliff-forming unit). A white dashed line marks the approximate position of the disconformity. Light-toned material in the figure is of two types: Anhydrite veins (light reddish-brown) that are terminated and crosscut by the disconformity, and Si-rich alteration halos (white, marked with arrows) that extend through the boundary (albeit with differing manifestations in the two units). (b). Silica-rich alteration halo in the Stimson sandstone. CheMin mineralogical analyses of the alteration halo and the parent sandstone provide information as to the nature of the late-stage diagenetic fluids that produced the alteration.

1201

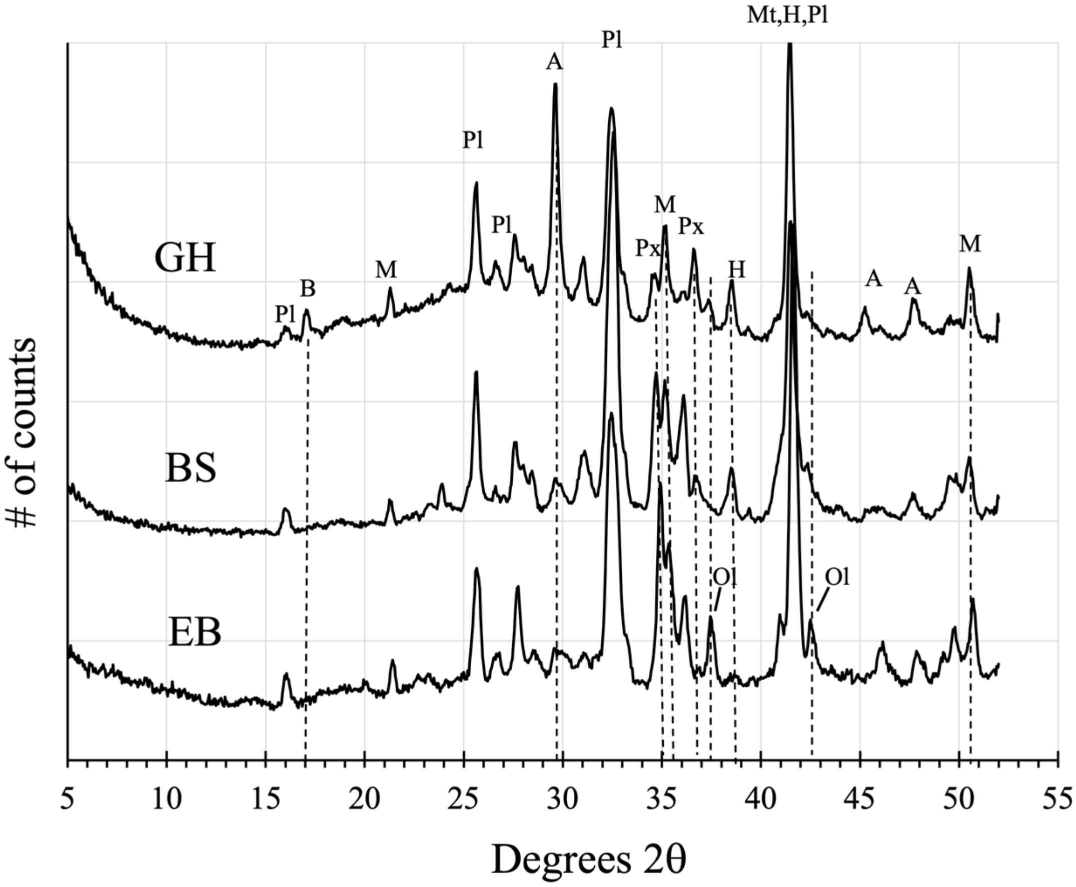

**Figure 18.** Diffraction patterns of Stimson Fm. sandstone. Edinburg (EB), likely the least altered Stimson sandstone, Big Sky (BS), slightly altered Stimson and Greenhorn (GH) pervasively altered Stimson in the light-toned alteration halo. Dotted lines identify major mineralogical changes to the Stimson due to late-stage diagenetic alteration (Pl = plagioclase feldspar, B = bassanite, M = magnetite, A = anhydrite, Px = pyroxene, H = hematite, Ol – olivine). 1202 1203 1204 1205 1206

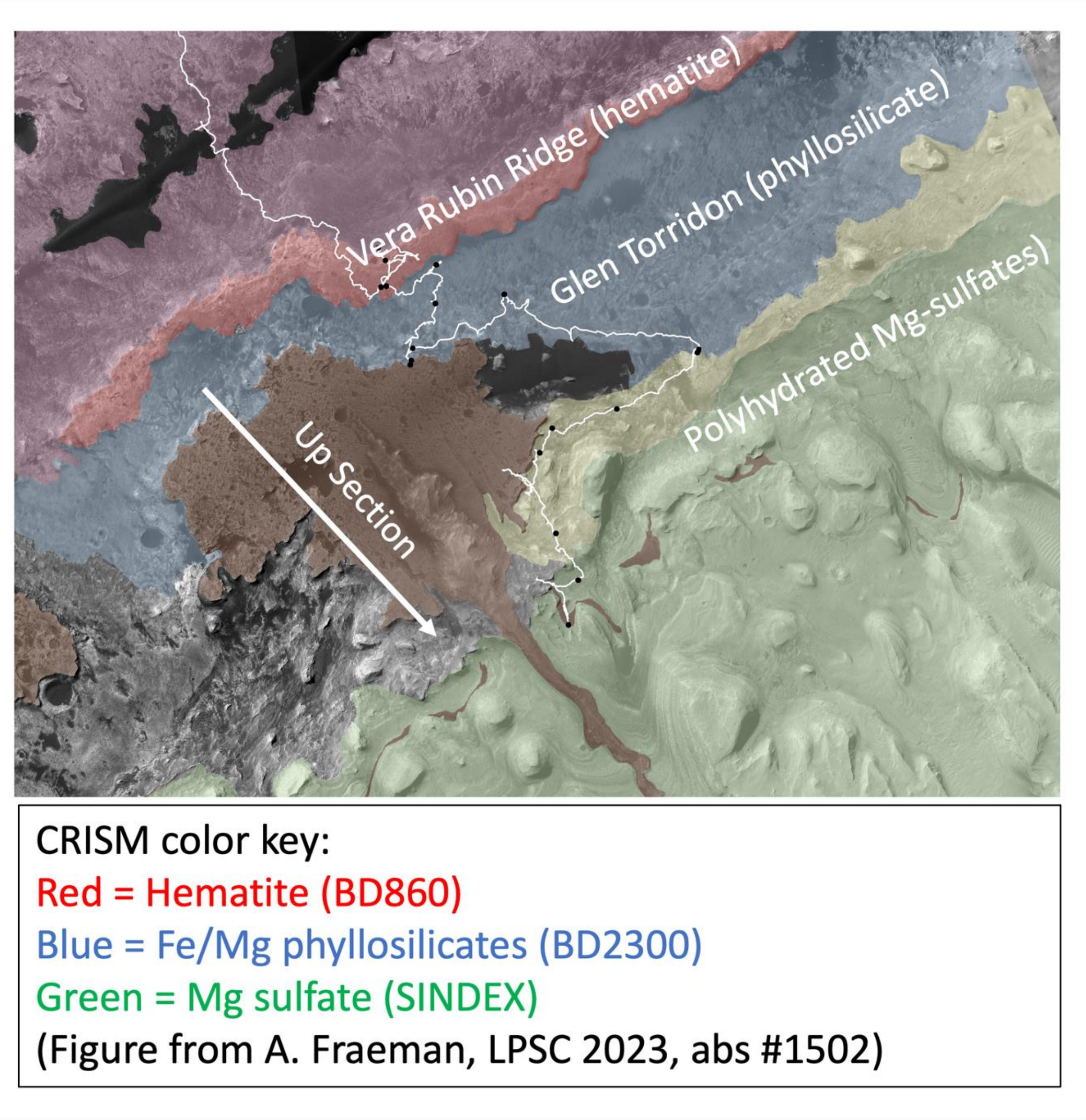

**Figure 19.** CRISM (Compact Reconnaissance Imaging Spectrometer for Mars) image of the Vera Rubin Ridge-Glen Torridon region of Mt. Sharp.

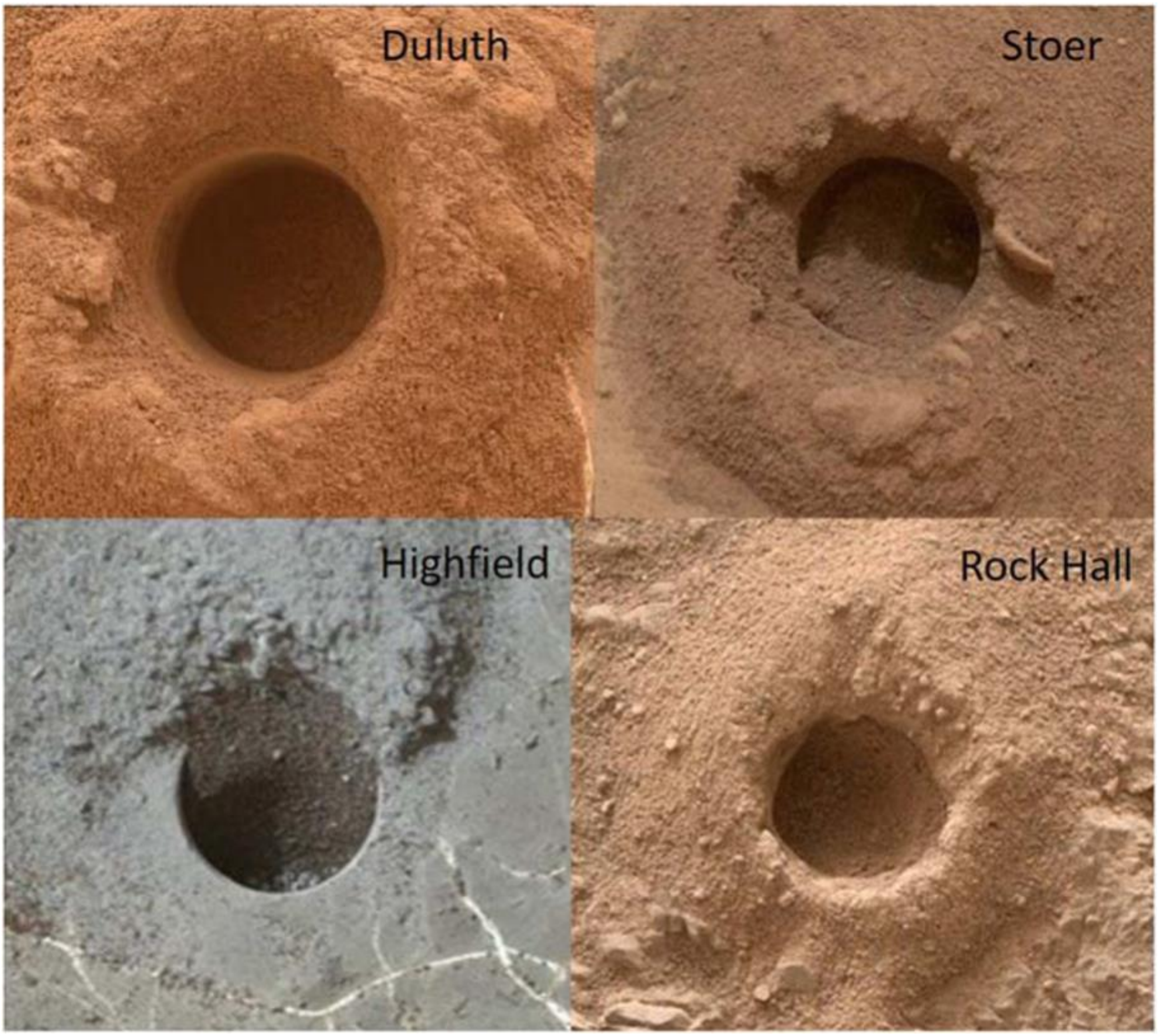

**Figure 20.** Drill holes for Duluth (DU), Stoer (ST), Highfield (HF), and Rock Hall (RH). ST, HF, and RH were drilled from Vera Rubin ridge, a hematite-rich ridge-forming feature seen from orbit, and DU, which lacks the orbital hematite signature was drilled immediately below the ridge for comparison.

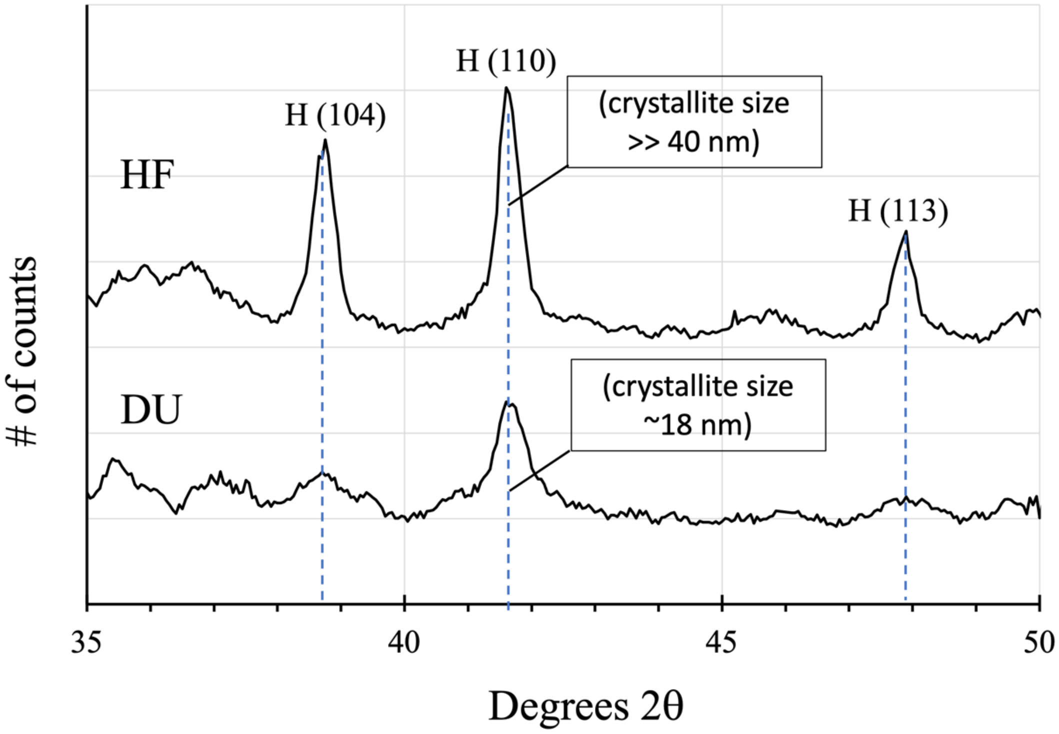

**Figure 21.** Comparison of hematite (104), (110) and (113) diffraction maxima (marked as "H") between DU, (Murray Fm. mudstone below VRR) and HF (altered Murray Fm. mudstone within VRR).

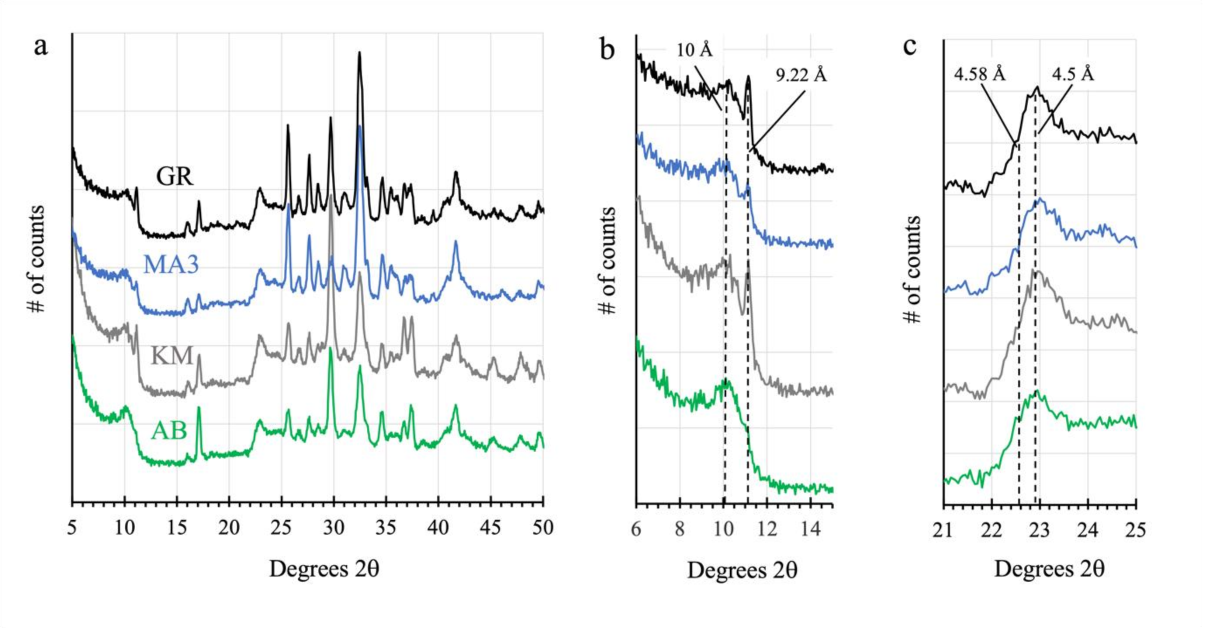

**Figure 22.** Diffraction patterns of four of the eight samples drilled from the Glen Torridon region of Gale crater. (a). Overall patterns of Aberlady (AB), Kilmarie (KM), Mary Anning 3 (MA3) and Groken (GK). (b). Low 2θ region showing the (001) maxima of clay minerals identified in Glen Torridon. All samples have the 10 Å (001) maximum typical of a collapsed smectite clay. KM, MA3 and GR also exhibit a sharp peak at 9.2 Å (the origin of which is a matter of debate; see discussion in the text). (c). 2θ region of the 02*l* diffraction band of smectite clay minerals. All clay minerals are dioctahedral.

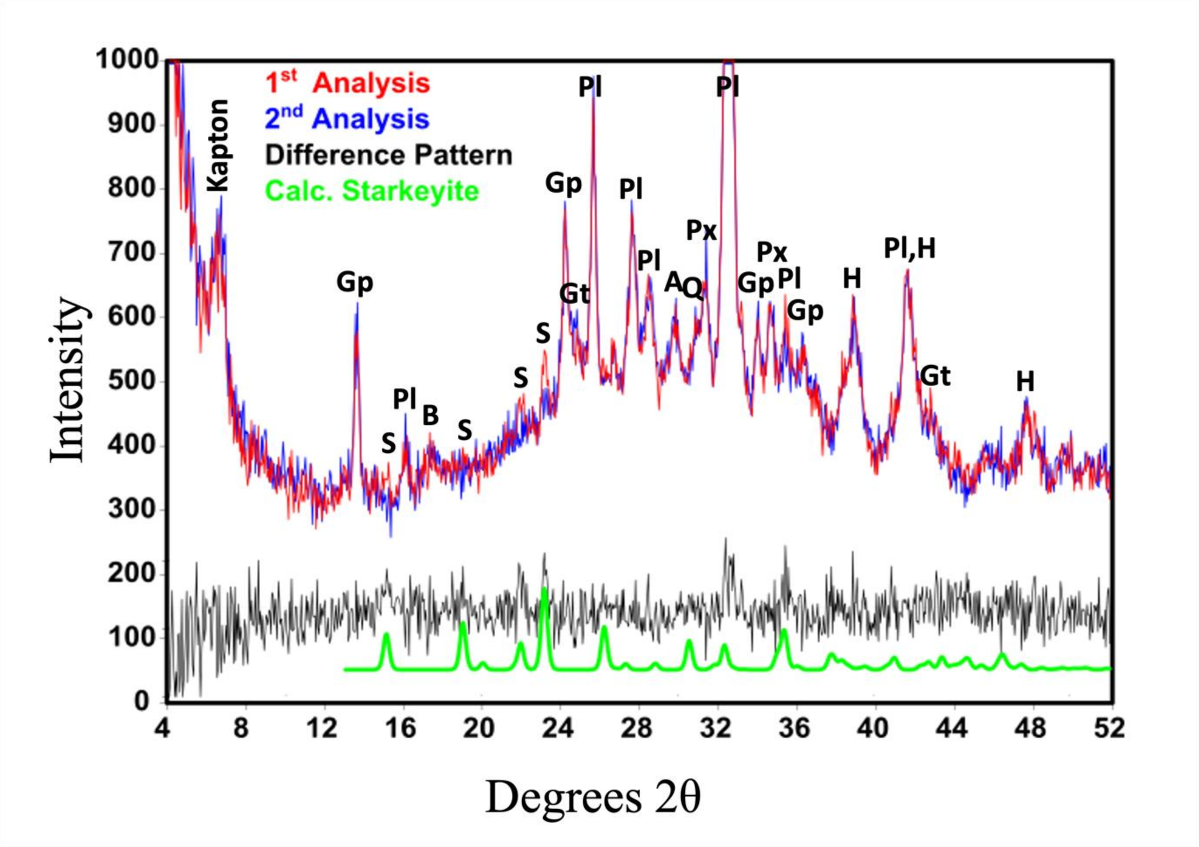

**Figure 23.** Diffraction pattern from the first night of analysis of Canaima, in the Sulfate Bearing Unit. Low angle peak labelled Kapton is due to the cell window material. Gp = gypsum, S = starkeyite, Pl = plagioclase feldspar, B = bassanite, A = anhydrite, Px = pyroxene, H = hematite. Broad scattering peak between 15° and 45° 2θ and low angle rise below 10° 2θ are due to X-ray amorphous material which accounts for 62% of the sample (redrawn from [97]).

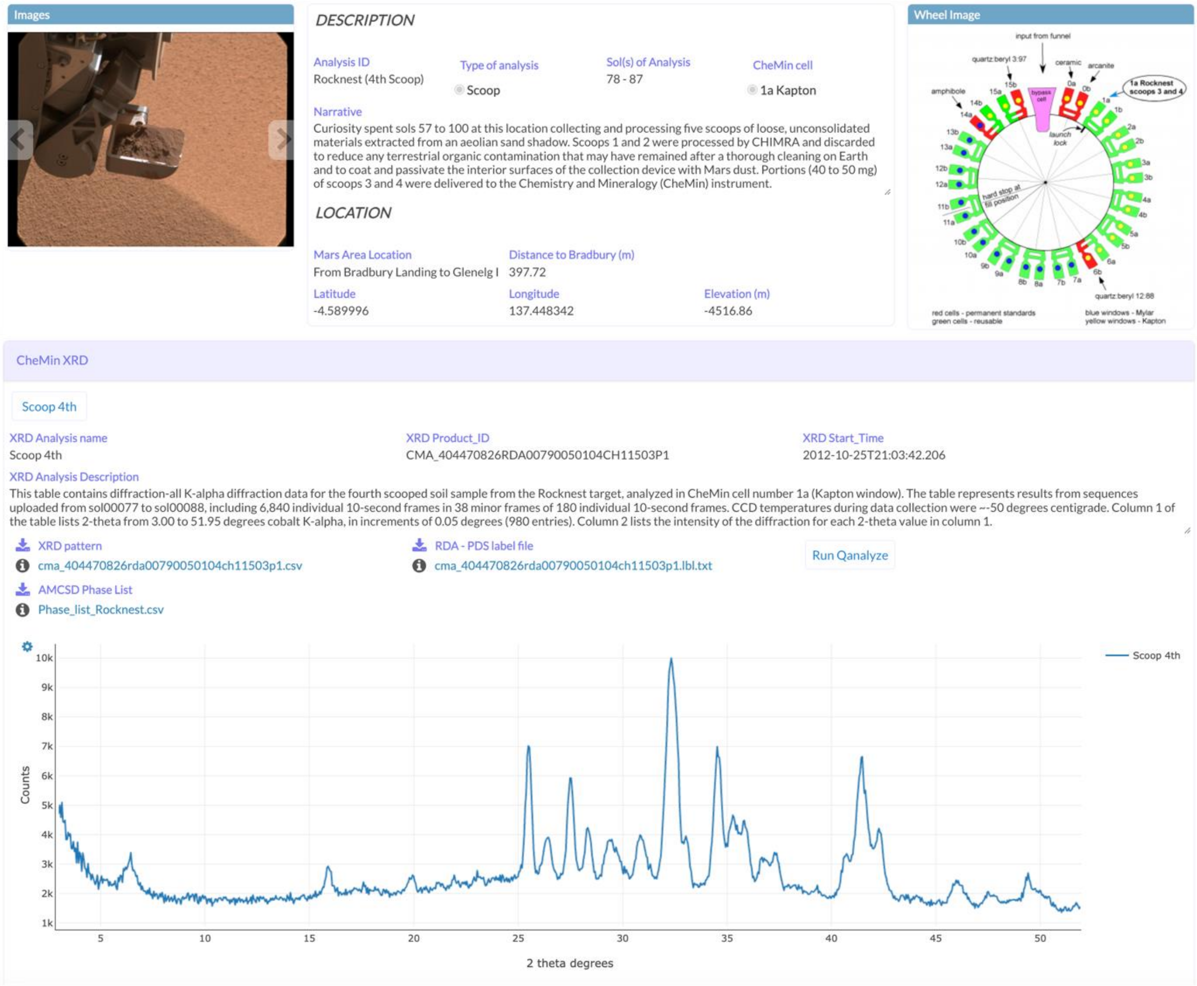

Images

DESCRIPTION

Analysis ID
Rocknest (4th Scoop)

Type of analysis
○ Scoop

Sol(s) of Analysis
78 - 87

CheMin cell
○ 1a Kapton

Narrative
Curiosity spent sols 57 to 100 at this location collecting and processing five scoops of loose, unconsolidated materials extracted from an aeolian sand shadow. Scoops 1 and 2 were processed by CHIMRA and discarded to reduce any terrestrial organic contamination that may have remained after a thorough cleaning on Earth and to coat and passivate the interior surfaces of the collection device with Mars dust. Portions (40 to 50 mg) of scoops 3 and 4 were delivered to the Chemistry and Mineralogy (CheMin) instrument.

LOCATION

Mars Area Location
From Bradbury Landing to Glenelg I

Distance to Bradbury (m)
397.72

Latitude
-4.589996

Longitude
137.448342

Elevation (m)
-4516.86

Wheel Image

CheMin XRD

Scoop 4th

XRD Analysis name
Scoop 4th

XRD Product_ID
CMA_404470826RDA00790050104CH11503P1

XRD Start_Time
2012-10-25T21:03:42.206

XRD Analysis Description
This table contains diffraction-all K-alpha diffraction data for the fourth scooped soil sample from the Rocknest target, analyzed in CheMin cell number 1a (Kapton window). The table represents results from sequences uploaded from sol00077 to sol00088, including 6,840 individual 10-second frames in 38 minor frames of 180 individual 10-second frames. CCD temperatures during data collection were ~-50 degrees centigrade. Column 1 of the table lists 2-theta from 3.00 to 51.95 degrees cobalt K-alpha, in increments of 0.05 degrees (980 entries). Column 2 lists the intensity of the diffraction for each 2-theta value in column 1.

XRD pattern
cma_404470826rda00790050104ch11503p1.csv

RDA - PDS label file
cma_404470826rda00790050104ch11503p1.lbl.txt

Run Qanalyze

AMCSD Phase List
Phase_list_Rocknest.csv

**Figure 24.** A screenshot of a portion of a sample data record from the Gale Crater Mineralogy and Geochemistry database ([19]).

**Table 1.** APXS compositions of modern basaltic soils in Gale crater, Meridiani Planum, and Gusev crater normalized to 100% totals[1] (after [41]).

| | **Gale[2]** | | **Meridiani** | **Gusev** |
|---|---|---|---|---|
| | Rocknest | Gobabeb | Average[3] | Average[3] |
| $SiO_2$ | 43.02 | 47.90 | 45.7 ± 1.3 | 46.1 ± 0.9 |
| $TiO_2$ | 1.19 | 0.88 | 1.03 ± 0.12 | 0.88 ± 0.19 |
| $Al_2O_3$ | 9.38 | 9.78 | 9.25 ± 0.50 | 10.19 ± 0.69 |
| $FeO_T$ | 19.20 | 17.92 | 18.8 ± 1.2 | 16.3 ± 1.1 |
| MnO | 0.42 | 0.37 | 0.37 ± 0.02 | 0.32 ± 0.03 |
| MgO | 8.70 | 7.57 | 7.38 ± 0.29 | 8.67 ± 0.60 |
| CaO | 7.27 | 7.30 | 6.93 ± 0.32 | 6.3 ± 0.29 |
| $Na_2O$ | 2.70 | 2.75 | 2.21 ± 0.18 | 3.01 ± 0.30 |
| $K_2O$ | 0.49 | 0.49 | 0.48 ± 0.05 | 0.44 ± 0.07 |
| $P_2O_5$ | 0.95 | 0.79 | 0.84 ± 0.06 | 0.91 ± 0.31 |
| $Cr_2O_3$ | 0.49 | 0.39 | 0.41 ± 0.06 | 0.33 ± 0.07 |
| Cl | 0.69 | 0.50 | 0.65 ± 0.09 | 0.70 ± 0.16 |
| $SO_3$ | 5.48 | 3.36 | 5.83 ± 1.04 | 5.78 ± 1.25 |
| Ni | 456 | 504 | 457 ± 97 | 476 ± 142 |
| Zn | 327 | 190 | 309 ± 87 | 270 ± 90 |
| Br | 34 | 37 | 100 ± 111 | 53 ± 46 |

[1] Oxides and Cl are reported in wt. % and normalized to 100 %; Ni, Zn, and Br are reported as ppm.

[2] Values from [20].

[3] Values from [106].

**Table 2.** Adirondack, Rocknest, and Gobabeb mineral abundances (crystalline phases only) from normative APXS data and Rietveld refinement and FULLPAT analyses of CheMin XRD data[2] (after [20,41].

| Location | Gusev[1] | Gale[2] | |
|---|---|---|---|
| Sample | Adirondack | Rocknest | Gobabeb |
| Plagioclase | 39 | 40.7(5) | 36.5(8) |
| Olivine | 20 | 20.5(4) | 25.8(4) |
| Augite | 15 | 18.1(13) | 22.0(4) |
| Pigeonite | 15 | 12.3(12) | 10.6(4) |
| Magnetite | 6 | 2.8(5) | 2.1(2) |
| Anhydrite | ---- | 1.4(3)[c] | 1.3(1)[3] |
| Hematite | ---- | 1.6(1)[c] | 0.9(1)[3] |
| Quartz | 0 | 1.3(3)[c] | 0.8(1)[3] |
| Ilmenite | 1 | ---- | 1.3(5)[3] |
| Mg# [4] | ---- | 57(5) | 56(6) |
| Ca# [5] | ---- | 50(4) | 63(5) |

[1] Normative calculation from APXS data

[2] Abundances in wt. %; uncertainties reported as 1σ

[3] At or below detection limit

[4] Percent Mg in forsterite/fayalite

[5] Percent Ca in plagioclase feldspar

**Table 3.** Mineral formulas and associated errors (1σ) for the major minerals present in the Rocknest and Gobabeb aeolian dunes (after [20, 138]).

| Mineral | Rocknest | Gobabeb |
|---|---|---|
| Plagioclase | $Ca_{0.49(4)}Na_{0.51(4)}Al_{1.49}Si_{2.51}O_8$ | $Ca_{0.63(6)}Na_{0.37(6)}Al_{1.63}Si_{2.37}O_8$ |
| Olivine | $Mg_{1.14(3)}Fe_{0.86(3)}SiO_4$ | $Mg_{1.08(3)}Fe_{0.92(3)}SiO_4$ |
| Augite | $Mg_{0.94(9)}Ca_{0.72(4)}Fe_{0.34(10)}Si_2O_6$ | $Mg_{0.89(8)}Ca_{0.73(3)}Fe_{0.38(9)}Si_2O_6$ |
| Pigeonite | $Mg_{0.97(8)}Fe_{1.03(9)}Si_2O_6$ | $Mg_{0.95(12)}Fe_{0.99(17)}Ca_{0.06(8)}Si_2O_6$ |

**Table 4.** Mineral and amorphous abundances of samples in the lower Murray formation measured by CheMin, $2\sigma$ errors are denoted in parentheses (after [74]).

| Mineral | Confidence Hills | Mojave 2 | Telegraph Peak | Buckskin[1] |
|---|---|---|---|---|
| Plagioclase | 20.4(2.3) | 23.5(1.6) | 27.1(2.8) | 17.1(1.2) |
| Sanidine | 5.0(0.7) | -- | 5.2(2.2) | 3.4(0.7) |
| Forsterite | 1.2(0.7) | 0.2(0.8) | 1.1(1.2) | -- |
| Augite | 6.4(2.2) | 2.2(1.1) | -- | -- |
| Pigeonite | 5.3(1.7) | 4.6(0.7) | 4.2(1.0) | -- |
| Orthopyroxene | 2.1(3.1) | -- | 3.4(2.6) | -- |
| Magnetite | 3.0(0.7) | 3.0(0.6) | 8.2(0.9) | 2.8(0.3) |
| Hematite | 6.8(1.5) | 3.0(0.6) | 1.1(0.5) | -- |
| Quartz | 0.7(0.5) | 0.8(0.3) | 0.9(0.4) | -- |
| Cristobalite | -- | -- | 7.3(1.7) | 2.4(0.3) |
| Tridymite | -- | -- | -- | 13.6(0.8) |
| ($H_3O^+$, $K^+$, $Na^+$) Jarosite | 1.1(0.7) | 3.1(1.6) | 1.5(1.8) | -- |
| Anhydrite | -- | -- | -- | 0.7(0.2) |
| Fluorapatite | 1.3(1.5) | 1.8(1.0) | 1.9(0.5) | -- |
| Phyllosilicate[2] | 7.6 | 4.7 | -- | -- |
| Amorphous | 39.2±15 [2] | 53 [3] | 38.1±15 [2] | 60 [3] |

[1] Values from [22].

[2] Values from FULLPAT analyses alone

[3] Values from amorphous component calculations using CheMin and APXS results

**Table 5.** Mineralogical composition of Edinburgh (least altered Stimson sandstone), Big Sky (slightly altered Stimson sandstone) and Greenhorn (highly altered Stimson sandstone within the light-toned alteration halos, e.g., see Figure 17). The large amorphous component in Greenhorn includes a passive enrichment of silica from dissolution of pyroxene and the addition of silica from the invading diagenetic fluid.

| | Edinburgh | Big Sky | Greenhorn |
|---|---|---|---|
| plagioclase | 39.6 | 45.7 | 42.1 |
| tot. Px | 27.6 | 30.2 | 12.3 |
| sanidine | 04.6 | 1.7 | -- |
| magnetite | 14.0 | 12.6 | 17.3 |
| hematite | 00.5 | 3.6 | 6.0 |
| quartz | | 1.6 | 2.2 |
| forsterite | 11.5 | -- | -- |
| fluorapatite | 00.02 | 1.4 | -- |
| anhydrite | | 1.5 | 16.1 |
| tridymite [1] | -- | 1.8 [1] | -- |
| basanite | | -- | 4.0 |
| Total xtal. | 100% | 100% | 100% |
| % amorphous | 20% | 20% | 65% |

[1] Contamination from previous sample (Buckskin)

**Table 6.** Mineralogical composition of Murray Fm. mudstone (Duluth) and diagenetically altered Murray Fm. mudstone in the Vera Rubin ridge (Stoer, Highfield and Rock Hall).[1]

| | Drilled Sample | | | |
|---|---|---|---|---|
| Phase | Duluth | Stoer | Highfield | Rock hall |
| Plagioclase | 27.1 (6) | 23.2 (10) | 19.9 (9) | 20.2 (22) |
| K-spar | 3.2 (4) | 1.6 (13) | 1.6 (5) | --- |
| Pyroxene | 4.5 (11) | 3.3 (9) | 4.2 (15) | 9.1 (10) |
| Hematite | 6.1 (10) | 14.7 (8) | 8.5 (5) | 2.9 (2) |
| Magnetite | 0.7 (4) | 0.3 (3) | 0.5 (5) | --- |
| Akaganeite | --- | 1.2 (7) | --- | 6.0 (5) |
| Jarosite | --- | 1.0 (3) | --- | 2.3 (5) |
| Anhydrite | 1.7 (4) | 3.1 (3) | 3.5 (5) | 11.2 (4) |
| Bassanite | 3.5 (3) | 0.5 (2) | 1.1 (3) | --- |
| Gypsum | 0.1 (1) | 2.4 (8) | 2.2 (5) | --- |
| Quartz | 1.0 (4) | 0.7 (4) | 0.5 (3) | --- |
| Fluorapatite[a] | --- | --- | --- | 1.3 (4) |
| Phyllosilicate | 15 (4) | 10 (3) | 5 (1) | 13 (3) |
| Opal-CT | --- | --- | 4 (1) | --- |
| Amorphous | 37[2] | 38[2] | 49[2] | 38 (8)[3] |

[1] $1\sigma$ errors reported in parenthesis, applied to the last decimal place

[2] Minimum amorphous abundance based on mass balance calculations.

[3] Amorphous abundance based on FULLPAT analysis.

**Table 7.** Known $MgSO_4$ hydrate minerals and their formulae.

| Mineral | **Formula** |
|---|---|
| Kieserite | $MgSO_4 \cdot H_2O$ |
| Sanderite | $MgSO_4 \cdot 2H_2O$ |
| Starkeyite | $MgSO_4 \cdot 4H_2O$ |
| Cranswickite | $MgSO_4 \cdot 4H_2O$ |
| Pentahydrite | $MgSO_4 \cdot 5H_2O$ |
| Hexahydrite | $MgSO_4 \cdot 6H_2O$ |
| Epsomite | $MgSO_4 \cdot 7H_2O$ |
| Meridianiite | $MgSO_4 \cdot 11H_2O$ |
| Amorphous $MgSO_4$ | $MgSO_4 \cdot nH_2O$ (n varies from ~1 to 2) |

**Table 8.** Mineralogical composition of Canaima. Amorphous abundances obtained using full pattern fitting ([36], data from [97].

| Phase | 1st night | 3rd night | 13th night |
|---|---|---|---|
| Starkeyite | 2.3 ± 0.3 | 0.1 ± 0.2 | --- |
| Andesine | 16.9 ± 0.6 | 15.5 ± 0.6 | 18.0 ± 0.5 |
| Gypsum | 4.0 ± 0.2 | 4.1 ± 0.2 | 1.5 ± 0.2 |
| Bassanite | 0.4 ± 0.3 | 0.8 ± 0.4 | 1.76 ± 0.3 |
| Anhydrite | 0.6 ± 0.3 | 1.0 ± 0.4 | 0.9 ± 0.5 |
| Hematite | 4.7 ± 0.4 | 4.7 ± 0.6 | 4.8 ± 0.5 |
| Goethite | 2.2 ± 0.6 | 2.2 ± 0.7 | 2.2 ± 0.6 |
| Quartz | 0.5 ± 0.2 | 0.5 ± 0.3 | 0.5 ± 0.2 |
| Sanidine | 3.2 ± 0.4 | 2.7 ± 0.6 | 3.4 ± 0.4 |
| Pyroxene | 3.2 ± 1.1 | 3.4 ± 0.8 | 3.7 ± 1.1 |
| Amorphous $MgSO_4 \cdot nH_2O$ | 19.4 ± 3.5 | 20.9 ± 3.5 | 20.0 ± 3.5 |
| Other Amorphous | 29.5 ± 7.4 | 28.5 ± 7.1 | 28.7 ± 7.2 |
| Palagonite-Like Material | 13.0 ± 3.2 | 13.0 ± 3.2 | 14.3 ± 3.6 |
| Total | 100.0 | 100.0 | 100.0 |

**Table 9.** Oxide wt% composition of Canaima (bulk, crystalline component and amorphous component) from [97].

| Oxide | Chemical analysis (Wt%)[1,4] | Crystalline component (Wt%)[2,4] | Amorphous component (Wt %)[3,4] |
|---|---|---|---|
| $SiO_2$ | 29.35 ± 0.37 | 14.1 ± 5.9 | 15.2 ± 5.7 |
| $TiO_2$ | 0.77 ± 0.03 | --- | 0.77 ± 0.03 |
| $Al_2O_3$ | 5.67 ± 0.16 | 5.3 ± 2.2 | 0.4 ± 2.1 |
| $Cr_2O_3$ | 0.25 ± 0.01 | --- | 0.25 ± 0.01 |
| $FeO_{(T)}$ | 15.5 ± 0.17 | --- | 8.7 ± 2.6 |
| FeO | --- | 0.4 ± 0.4 | --- |
| $Fe_2O_3$ | --- | 6.7 ± 2.9 | --- |
| MnO | 0.18 ± 0.01 | --- | 0.18 ± 0.01 |
| MgO | 9.16 ± 0.21 | 1.2 ± 0.6 | 7.9 ± 0.6 |
| CaO | 4.25 ± 0.05 | 3.6 ± 1.5 | 0.7 ± 1.4 |
| $Na_2O$ | 1.88 ± 0.12 | 1.2 ± 0.6 | 0.7 ± 0.5 |
| $K_2O$ | 0.58 ± 0.02 | 0.3 ± 0.3 | 0.3 ± 0.2 |
| $P_2O_5$ | 0.75 ± 0.04 | --- | 0.75 ± 0.04 |
| $SO_3$ | 16.48 ± 0.19 | 3.4 ± 1.4 | 13.0 ± 1.5 |
| Cl | 1.09 ± 0.03 | --- | 1.09 ± 0.03 |
| $H_2O$ | 14.20 ± 2.3 | 2.0 ± 0.8 | 12.1 ± 2.4 |

[1] Oxide wt% from APXS measurement of dump pile ([106]); $H_2O$ wt% from ChemCam ([107]).

[2] Oxide wt% calculated from CheMin diffraction data using refined lattice parameter vs. composition equations from [26].

[3] Oxide wt % of bulk sample, crystalline component and amorphous component, calculated using mass balance calculations. The composition of the amorphous component is obtained by subtracting the composition of the crystalline component is subtracted from the bulk composition ([40]).

[4] Precision errors are 1σ values.

**Table 10.** Composition of the amorphous components of selected aeolian soil, Bradbury Fm., Murray Fm., Stimson Fm. and Sulfate Bearing Unit samples analyzed by CheMin. RN = Rocknest, CB = Cumberland, MJ2 = Mojave 2, BK = Buckskin, BS = Big Sky, GH = Greenhorn, Ca = Canaima.

| Oxide % | Soil Avg. (RN, GB) | Bradbury Fm (CM) | Murray Fm (MJ 2) | Altered Murray Fm (BK) | Stimson Fm (BS) | Altered Stimson Fm (GH) | Sulfate Bearing Unit (CA) |
|---|---|---|---|---|---|---|---|
| $SiO_2$ | 37.50 | 25.557 | 55.725 | 75.9 | 24.133 | 63.525 | 30.5 |
| $TiO_2$ | 2.711 | 3.659 | 2.487 | 2.18 | 6.587 | 1.537 | 1.54 |
| $Al_2O_3$ | 4.253 | 0.000 | 7.196 | 0 | 0.123 | 0.000 | 0.8 |
| $Cr_2O_3$ | 1.765 | 1.700 | 0.773 | 0.179 | 3.359 | 0.692 | 0.5 |
| $FeO_T$ | 19.80 | 18.033 | 12.269 | 4.796 | 17.478 | 10.159 | 17.42 |
| MnO | 1.568 | 1.086 | 0.831 | 0.161 | 2.641 | 0.211 | 0.4 |
| MgO | 0.000 | 17.534 | 5.794 | 1.467 | 14.676 | 1.462 | 15.8 |
| CaO | 4.085 | 11.119 | 0.000 | 2.145 | 0.000 | 5.470 | 1.4 |
| $Na_2O$ | 4.387 | 1.658 | 1.819 | 1.15 | 6.030 | 2.076 | 1.4 |
| $K_2O$ | 1.903 | 0.532 | 1.111 | 0.847 | 1.402 | 0.461 | 0.6 |
| $P_2O_5$ | 3.469 | 3.179 | 0.754 | 2.237 | 1.686 | 1.767 | 1.5 |
| $SO_3$ | 16.13 | 11.544 | 10.342 | 7.75 | 17.076 | 11.934 | 26 |
| Cl | 2.418 | 4.398 | 0.899 | 0.52 | 4.809 | 0.707 | 2.2 |
| F | -- | 0.000 | 0.159 | 0 | 0.049 | 0.000 | --- |
| Proportion[1] | 0.28 | 0.26 | 0.47 | 0.558 | 0.14 | 0.64 | |

[1] Proportion of X-ray amorphous material in the sample

**Supplementary Materials:** CheMin data as well as companion data from the SAM and APXS instruments on MSL Curiosity are archived in and downloadable from the Gale crater Mineralogy and Geochemistry Sample Database (doi: https://doi.org/10.48484/JN48-YW52 [19]), as well as sample descriptions, open access publications, mineralogical analysis tools, CIF files, etc. Figure S1 shows images of each of the drill holes and scooped samples analyzed by CheMin. Table S1 lists the names of all samples and descriptive data for each. This is a living repository of CheMin data and additional drill samples and analyses will be included as they are obtained.

**Author Contributions:** The review paper summarizes the findings of numerous studies from the MSL team, instrument teams, and in the laboratory. All co-authors were involved with at least one of the following individual projects reviewed in this paper: conceptualization, methodology, formal analysis, investigation, data curation. Conceptualization, D.B., V.M.T., T.B., E.B.R., D.V., S.C., P.S., R.M., S.M., A.Y., R.D., R.H., A.T., D.M., G.D., C.A., N.C., T.P., D.D.M., P.C., B.L., B.T., E.H., S.S., R.W., M.T., J.M., A.P., M.G., P.D., J.B., L.T., A.M., C.O.-C., B.S., J.M.M., A.F., J.G., K.S., S.M., A.V. methodology, D.B., V.M.T., T.B., E.B.R., D.V., S.C., P.S., R.M., S.M., A.Y., R.D., R.H., A.T., D.M., G.D., C.A., N.C., T.P., D.D.M., P.C., B.L., B.T., E.H., S.S., R.W., M.T., J.M., A.P., M.G., P.D., J.B., L.T., A.M., C.O.-C., B.S., J.M.M., A.F., J.G., K.S., S.M., A.V. investigation, D.B., V.M.T., T.B., E.B.R., D.V., S.C., P.S., R.M., S.M., A.Y., R.D., R.H., A.T., D.M., G.D., C.A., N.C., T.P., D.D.M., P.C., B.L., B.T., E.H., S.S., R.W., M.T., J.M., A.P., M.G., P.D., J.B., L.T., A.M., C.O.-C., B.S., J.M.M., A.F., J.G., K.S., S.M., A.V. formal analysis, D.B., V.M.T., T.B., E.B.R., D.V., S.C., P.S., R.M., S.M., A.Y., R.D., R.H., A.T., D.M., G.D., C.A., N.C., T.P., D.D.M., P.C., B.L., B.T., E.H., S.S., R.W., M.T., J.M., A.P., M.G., P.D., J.B., L.T., A.M., C.O.-C., B.S., J.M.M., A.F., J.G., K.S., S.M., A.V. investigation, D.B., V.M.T., T.B., E.B.R., D.V., S.C., P.S., R.M., S.M., A.Y., R.D., R.H., A.T., D.M., G.D., C.A., N.C., T.P., D.D.M., P.C., B.L., B.T., E.H., S.S., R.W., M.T., J.M., A.P., M.G., P.D., J.B., L.T., A.M., C.O.-C., B.S., J.M.M., A.F., J.G., K.S., S.M., A.V. data curation, D.B., T.B., E.R. writing-original draft preparation, D.B. writing-review and editing, D.B., V.T. visualization, D.B. All authors have read and agreed to the published version of the manuscript.

**Funding:** Some of this research was carried out at the Jet Propulsion Laboratory, California Institute of Technology under a contract with the National Aeronautics and Space Administration (NASA).

**Data Availability Statement:** Publicly available datasets were analyzed in this study. This data can be found here: [https://pds.nasa.gov], accessed on 23 July 2021. Additional contextual information can be found in the publicly available CheMin Database found here: [https://odr.io/chemin].

**Acknowledgments:** We acknowledge the support of the Jet Propulsion Laboratory engineering and management teams and the MSL science team members who participated in tactical and strategic operations, without whom the data presented here could not have been collected.

**Conflicts of Interest:** The authors declare no conflicts of interest.

## Appendix A

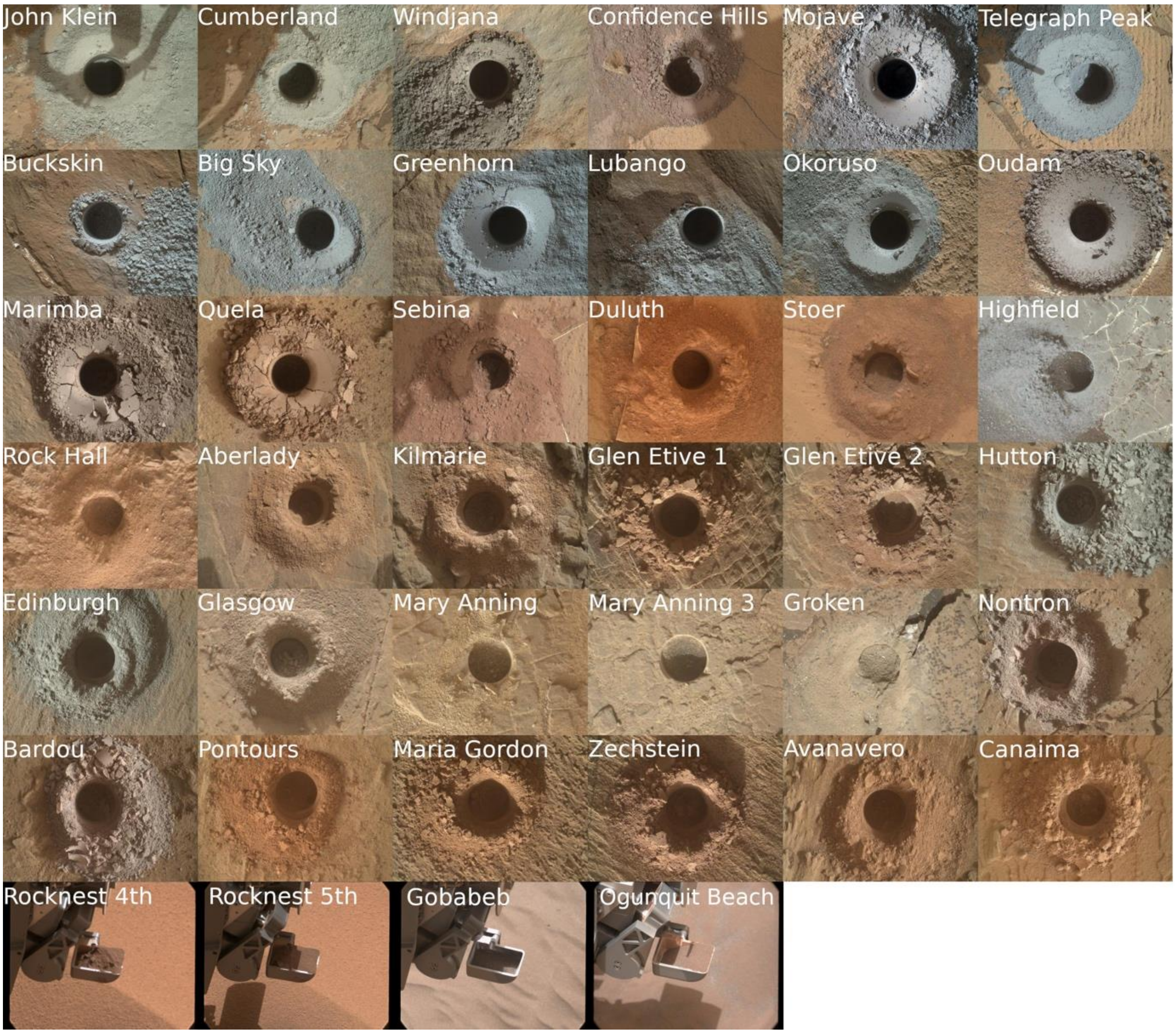

**Figure S1.** Images of drill holes and scooped aeolian material analyzed by CheMin to date.

Table S1- Details of CheMin drill samples and scooped aeolian soil during the 12-year deployment of MSL Curiosity on Mars.

| **Analysis ID** | **Mars area location** | **Analysis type** | **CheMin cell** | **XRD Sol(s) of Analysis** | **Drill Sol** | **Elevation (m)** |
|---|---|---|---|---|---|---|
| Rocknest (4th Scoop) | From Bradbury Landing to Glenelg Intrigue | Scoop | 1a Kapton | 78 – 87 | 74 | -4516.86 |
| Rocknest (5th scoop) | From Bradbury Landing to Glenelg Intrigue | Scoop | 7a mylar | 94 – 119 | 93 | -4516.86 |

| | | | | | | |
|---|---|---|---|---|---|---|
| John Klein | Yellowknife Bay | Drill | 13b mylar | 195 - 272, 473-488 | 182 | -4520.46 |
| Cumberland | Yellowknife Bay | Drill | 12b mylar | 282-432 | 279 | -4520.24 |
| Windjana | Kimberley | Drill | 13a mylar | 623 – 694 | 621 | -4478.55 |
| Confidence Hills | Pahrump Hills, Murray formation | Drill | 12a mylar | 765 – 785 | 756 | -4460.62 |
| Mojave2 | Pahrump Hills, Murray formation | Drill | 6a Kapton | 884 – 894 | 867 | -4459.71 |
| Telegraph Peak | Pahrump Hills, Murray formation | Drill | 5b Kapton | 922 – 949 | 905 | -4453.51 |
| Buckskin | Pahrump Hills, Murray formation | Drill | 14b Kapton | 1061 – 1078 | 1060 | -4447.04 |
| Big Sky | Naukluft Plateau | Drill | 7b mylar | 1121 – 1131 | 1116 | -4434.42 |
| Greenhorn | Naukluft Plateau | Drill | 8a mylar | 1139 – 1148 | 1134 | -4434.23 |
| Gobabeb | Bagnold Dune Field | Scoop | 7a mylar | 1227 – 1280 | 1224 | -4423.76 |
| Lubango | Naukluft Plateau | Drill | 8a mylar | 1323 – 1330 | 1320 | -4429.04 |
| Okoruso | Naukluft Plateau | Drill | 7b mylar | 1334 – 1346 | 1332 | -4429.17 |
| Oudam | Hartmann’s Valley member, Murray formation | Drill | 12a mylar | 1362 – 1369 | 1361 | -4435.68 |
| Oudam 13a | Hartmann’s Valley member, Murray formation | Drill | 13a mylar | 1375- 1387 | 1375 | -4435.59 |
| Marimba2 | Karasburg member, Murray formation | Drill | 8b mylar | 1425 – 1436 | 1422 | -4410.68 |
| Quela | Karasburg member, Murray formation | Drill | 5a Kapton | 1470 - 1480 | 1464 | -4379.26 |
| Sebina | Sutton Island member, Murray formation | Drill | 4b Kapton | 1496 - 1507 | 1495 | -4360.89 |
| Ogunquit Beach | Bagnold Dune | Scoop | 1a Kapton | 1832-1931 | 1829? | -4299.95 |

| | | | | | | |
|---|---|---|---|---|---|---|
| Duluth | Blunts Point member, Vera Rubin ridge | Drill | 13b mylar | 2068-2095 | 2057 | -4191.63 |
| Stoer | Pettegrove Point member, Vera Rubin ridge | Drill | 10a mylar | 2141-2151 | 2136 | -4170.39 |
| Highfield | Jura member, Vera Rubin ridge | Drill | 10a mylar | 2226-2242 | 2224 | -4146.75 |
| Rock Hall | Jura member, Vera Rubin ridge | Drill | 7b mylar | 2264-2284 | 2261 | -4143.69 |
| Aberlady | Clay-bearing unit - Glen Torridon | Drill | 8a mylar | 2373-2384 | 2370 | -4157.79 |
| Kilmarie | Clay-bearing unit - Glen Torridon | Drill | 9b mylar | 2388-2400 | 2384 | -4157.93 |
| Glen Etive 1 | Glen Torridon | Drill | 8b mylar | 2492-2503 | 2486 | -4132.99 |
| Glen Etive 2 | Glen Torridon | Drill | 8a mylar | 2543-2555 | 2527 | -4132.95 |
| Hutton | Glen Torridon | Drill | 12a mylar | 2672-2678 | 2668 | -4095.84 |
| Edinburgh | Glen Torridon | Drill | 7b mylar | 2715-2723 | 2711 | -4088.44 |
| Glasgow | Glen Torridon | Drill | 7b mylar | 2758-2774 | 2754 | -4107.93 |
| Mary Anning | Glen Torridon | Drill | 7a mylar | 2842-2854 | 2828? | -4128.06 |
| Mary Anning 3 | Glen Torridon | Drill | 7a mylar | 2888-2894 | 2870 | -4128.06 |
| | | | | | | |
| Groken | Glen Torridon | Drill | 9a mylar | 2912-2930 | 2910 | -4127.91 |
| Nontron | Clay mineral - Sulfate mineral transition region | Drill | 9a mylar | 3058-3077 | 3056 | -4072.91 |
| Bardou | Clay mineral - Sulfate mineral transition region | Drill | 4a Kapton | 3097-3113 | 3094 | -4066.48 |
| Pontours | Clay mineral - Sulfate mineral transition region | Drill | 1a Kapton | 3172 | 3170 | -4041.25 |

| | | | | | | |
|---|---|---|---|---|---|---|
| Maria Gordon | Clay mineral - Sulfate mineral transition region | Drill | 1a Kapton | 3232 | 3229 | -4015.23 |
| Zechstein | Clay mineral - Sulfate mineral transition region | Drill | 1a Kapton | 3292 | 3289 | -3991.11 |
| Avanavero | Clay mineral - Sulfate mineral transition region | Drill | 15a Kapton | 3517-3520 | 3512 | -3920 |
| Canaima | Sulfate Bearing Unit | Drill | 15a Kapton | 3614 | 3612 | -3880 |
| Tapo Caparo | Sulfate Bearing Unit | Drill | 15a Kapton | 3755 | 3752 | -3860 |
| Ubajara | Sulfate Bearing Unit | Drill | 15a Kapton | 3825-3827 | 3823 | -3800 |
| Sequoia | Sulfate Bearing Unit | Drill | 1b Kapton | 3982-3991 | 3982 | -3760 |
| Mineral King | Sulfate Bearing Unit | Drill | 2a Kapton | 4113 | 4110 | |

## References

1. Anderson, R. C., Jandura, L., Okon, A. B., Sunshine, D., Roumeliotis, C., Beegle, L. W., Hurowitz, J., Kennedy, B., Limonadi, D., McCloskey, S., Robinson, M., Seybold, C., Brown, K. Collecting Samples in Gale Crater, Mars; an Overview of the Mars Science Laboratory Sample Acquisition, Sample Processing and Handling System. *Space Sci. Rev.* **2012**, 170 (1–4), 57–75. doi: https://doi.org/10.1007/s11214-012-9898-9
2. Blake, D., Vaniman, D., Achilles, C., Anderson, R., Bish, D., Bristow, T., Chen, C., Chipera, S., Crisp, J., Des Marais, D. J., Downs, R.T., Farmer, J., Feldman, S., Fonda, M., Gailhanou, M. Ma, H. Ming, D.W., Morris, R.V., Sarrazin, P., Stolper, E., Treiman, A. and Yen, A. Characterization and Calibration of the CheMin Mineralogical Instrument on Mars Science Laboratory. *Space Sci. Rev.* **2012**, 170 (1-4), 341–399. doi: https://doi.org/10.1007/s11214-012-9905-1
3. Thomson, B. J., Bridges, N. T., Milliken, R., Baldridge, A., Hook, S. J., Crowley, J. K., Marion, G. M. de Souza Filho, C. R., Brown, A. J., Weitz, C.M. Constraints on the origin and evolution of the layered mound in Gale Crater, Mars using Mars Reconnaissance Orbiter data. *Icarus.* **2011**, 214 (2), 413–432. doi: https://doi.org/10.1016/j.icarus.2011.05.002
4. Malin, M. C. and Edgett, K. S. Sedimentary rocks of early Mars. *Science.* **2000**, 290(5498),1927-1937. doi: http://doi.org/10.1126/science.290.5498.1927
5. Grotzinger, J. P., Crisp, J., Vasavada, A. R., Anderson, R. C., Baker, C. J., Barry, R., Blake, D. F., Conrad, P., Edgett, K. S., Ferdowski, B., Gellert, R., Gilbert, J. B., Golombek, M., Gomez-Elvira, J., Hassler, D. M., Jandura, L., Litvak, M., Mahaffy, P., Maki, J., Meyer, M., Malin, M. E., Mitrofanov, I., Simonds, J. J., Vaniman, D., Welch, R. V., and Wiens, R. C. Mars Science Laboratory Mission and Science Investigation. *Space Sci*. **2012**, Rev. 170 (1-4), 5–56. doi: https://doi.org/10.1007/s11214-012-9892-2
6. Milliken, R. E., Grotzinger, J. P., Thomson, B. J. Paleoclimate of Mars as captured by the stratigraphic record in Gale Crater. *Geophys. Res. Lett*. **2010**, 37 (4). doi: https://doi.org/10.1029/2009GL041870
7. Fraeman, A. A., Arvidson, R. E., Catalano, J. G., Grotzinger, J. P., Morris, R. V., Murchie, S. L., Stack, K. M., Humm, D. C., McGovern, J. A., Seelos, F. P., Seelos, K. D. and Viviano, C. E. A hematite-bearing layer in Gale Crater, Mars: Mapping and implications for past aqueous conditions. *Geology*, **2013**, 41(10), 1103–1106. doi: https://doi.org/10.1130/G34613.1
8. Fraeman, A. A., Ehlmann, B. L., Arvidson, R. E., Edwards, C. S., Grotzinger, J. P., Milliken, R. E., Quinn, D. P. and Rice, M. S. The stratigraphy and evolution of lower Mount Sharp from spectral, morphological, and thermophysical orbital data sets. *Journal of Geophysical Research Planets*, **2016**, 121(9):1713-1736. doi: 10.1002/2016jE005095
9. Grotzinger, J. P., Crisp, J., Vasavada, A. R., Anderson, R. C., Baker, C. J., Barry, R., Blake, D. F., Conrad, P., Edgett, K. S., Ferdowski, B., Gellert, R., Gilbert, J. B., Golombek, M., Gomez-Elvira, J., Hassler, D. M., Jandura, L., Litvak, M., Mahaffy, P., Maki, J., Meyer, M., Malin, M. E., Mitrofano, I., Simonds, J. J., Vaniman, D., Welch, R. V., and Wiens, R. C. Mars Science Laboratory Mission and Science Investigation. *Space Sci. Rev.* **2012**, 170 (1-4), 5–56. doi: https://doi.org/10.1007/s11214-012-9892-2
10. Edgett, K. S., Yingst, R. A., Ravine, M. A., Caplinger, M.A., Maki, J. N., Ghaemi, F. T., Schaffner, J. A., Bell, J. F., Edwards, L. J., Herkenhoff, K. E. and Heydari, E., Curiosity's Mars Hand Lens Imager (MAHLI) Investigation. *Space Sci. Rev*. 2012 170, 259-317. doi: https://doi.org/10.1007/s11214-012-9910-4.
11. Malin, M. C., Caplinger, M. A., Edgett, K. S., Ghaemi, F. T., Ravine, M. A., Schaffner, J. A., Baker, J. M., Bardis, J. D., DiBiase, D. R., Maki, J. N., Willson, R. G., Bell, J. F. III, Dietrich, W. E., Edwards, L. J., Hallet, B., Herkenhoff, K. E., Heydari, E, Kah, L. C., Lemmon, M. T., Minitti, M. E., Olson, T. S., Parker, T. J., Rowland, S. K., Schieber, J., Sullivan, R. J., Sumner, D. Y., Thomas, P. C. and Yingst, R. A., The Mars Science Laboratory (MSL) Mast-mounted Cameras (Mastcams) Flight Instruments. Lunar and Planetary Science Conf, Houston, Texas, USA, 2010, 41, abstr. #1123. Available at: https://www.lpi.usra.edu/meetings/lpsc2010/pdf/1123.pdf
12. Gellert R., Rieder R., Bruckner J., Clark, B. C., Dreibus, G., Klingelhofer, G., Lugmair, G., Ming, D. W., Wanke, H., Yen, A., Zipfel, J. and Squyres, S. W. *J. Geophys. Res.* **2006**, 111, E02S05. doi: https://doi.org/10.1029/2005JE002555

13. Campbell, J. L., Perrett, G. M., Gellert, R., Andrushenko S. M., Boyd, N. I., Maxwell, J.A., King, P. L. and Schofield, C.D. *Space Sci. Rev.* **2012**, 170 pp. 319–340. doi: https://doi.org/10.1007/s11214-012-9873-5
14. Maurice et al., 2012 - Maurice S., Wiens R.C., Saccoccio, M., Barraclough, B., Gasnault, O., Forni, O., Mangold, N., Baratoux, D., Bender, S., Berger, G., Bernardin, J., Berthe, M., Bridges, N., Blaney, D., Bouye, M. Cais, P., Clark, B., Clegg, S., Cousin, A., Cremers, D., Cros, A., DeFlores, L., Derycke, C., Dingler, B., Dromart, G., Dubois, B., Dupieux, M., Durand, E., d'Uston, L., Fabre, C., Faure, B., Gaboriaud, A., Gharsa, T., Herkenhoff, K., Kan, E., Kirkland, L., Kouach, D., Lacour, J. -L., Langevin, Y., Lasue, J., Le Mouelic, S., Lescure, M., Lewin, E., Limonadi, D., Manhes, G., Mauchien, P., McKay, C., Meslin, P. -Y., Michel, Y., Miller, E., Newsom, H. E., Orttner, G., Paillet, A., Pares, L., Parot, Y., Perez, R., Pinet, R., Poitrasson, F., Quertier, B., Salle, B., Sotin, C., Sautter, V., Seran, H., Simmonds, J. J., Sirven, J. -B., Stiglich, R., Striebig, N., Thocaven, J. -J., Toplis, M., J., and Vaniman, D. ChemCam Activities and Discoveries during the Nominal Mission of Mars Science Laboratory in Gale crater, Mars. *Space Sci Rev*. **2012**, 170 pp. 95-166. doi: https://doi.org/10.1007/s11214-012-9912-2
15. Wiens, R.C., Maurice, S., Barraclough, B., Saccoccio, M., Barkley, W.C., Bell III, J. F., Bender, S., Bernardin, J., Blaney, D., Blank, J., Bouyé, M., Bridges, N., Cais, P., Clanton, R.C., Clark, B., Clegg, S., Cousin, A., Cremers, D., Cros, A., DeFlores, L., Delapp, D., Dingler, R., d'Uston, C., Dyar, M.D., Elliott, T., Enemark, D., Fabre, C., Flores, M., Forni, O., Gasnault, O., Hale, T., Hays, C., Herkenhoff, K., Kan, E., Kirkland, L., Kouach, D., Landis, D., Langevin, Y., Lanza, N., LaRocca, F., Lasue, J., Latino, J., Limonadi, D., Lindensmith, C., Little, C., Mangold, N., Manhes, G., Mauchien, P., McKay, C., Miller, E., Mooney, J., Morris, R.V., Morrison, L., Nelson, T., Newsom, H., Ollila, A., Ott, M., Pares, L., Perez, R., Poitrasson, F., Provost, C., Reiter, J.W., Roberts, T., Romero, F., Sautter, V., Salazar, S., Simmonds, J.J., Stiglich, R., Storms, S., Striebig, N., Thocaven, J.-J., Trujillo, T., Ulibarri, M., Vaniman, D., Warner, N., Waterbury, R., Whitaker, R., Witt, J., Wong-Swanson, B. The ChemCam Instrument Suite on the Mars Science Laboratory (MSL) Rover: Body Unit and Combined System Tests. *Space Sci. Rev.* **2012**, 170(1-4), 167-227. doi: http://doi.org/10.1007/s11214-012-9902-4.
16. Mahaffy P. R., Webster, C. R., Cabane, M. , Conrad, P. G., Coll, P., Atreya, S. K., Arvey, R., Barciniak, M., Benna, M., Bleacher, L., Brinkerhoff, W. B., Eigenbrode, J. L., Carignan, D., Cascia, M., Chalmers, R. A., Dworkin, J. P., Errigo, T., Everson, P., Franz, H., Farley, R., Feng, S., Frazier, G., Freissinet, C., Glavin, D. P., Harpold, D. N., Hawk, D., Holmes, V., Johnson, C. S., Jones, A., Jordan, P., Kellogg, J., Lewis, J., Luness, E., Malespin, C. A., Martin, D. K., Mauer, J., McAdam, A., C., Mclennan, D., Nolan, T. J., Noriega, M., Pavlov A. A., Prats, B., Raaen, E., Sheinman, O., Sheppard, D., Smith, J., Stern, J. C., Tan, F., Trainer, M., Ming, D. W., Morris, R. V., Jones, J., Gundersen, C., Steele, A., Wray, J., Botta, O., Leshin, L. A., Owen, T., Battel, S., Jakosky, B. M., Manning, H., Squyres, S., Navarro-Gonzalez, R., McKay, C. P., Raulin, F., Sternberg, R., Buch, A., Sorrensen, Pl, Klein-Schoder, R., Coscia, D., Szopa, C., Teinturier, S., Baffes, C., Feldman, J., Flesch, G., Forouhar, S., Garcia, R., Keymeulen, D., Woodward, S., Block, B. P., Arenett, K., Miller R., Edmonson, C., Gorevan, S., and Mumm, E. The Sample Analysis at Mars Investigation and Instrument Suite. *Space Sci Rev.* 2012, 170 pp. 401-478. doi: https://doi.org/10.1007/s11214-012-9879-z
17. Gailhanou, M., 2023 unpublished.
18. Johnson, D. L., Carroll, B. C., Leland, R. S. MSL/CheMin Cryocooler System Requirements and Characterization Tests. 15th International Cryocooler Conference Long Beach, California, June 9-12, 2008, In Cryocoolers 15, pp. 621-630.
19. Lafuente, B., Blake, D., Bristow, T., Rampe, E., Downs, R., Sarrazin, P., Downs, G., Stone, N., Pires, A., Vaniman, D., Yen, A., Franz, H., Lyness, E., & Fraeman, A. (2021). Gale Crater Mineralogy and Geochemistry Sample Database (GCMGS). [Data set]. Open Data Repository. https://doi.org/10.48484/JN48-YW52.
20. Morrison, S.M., Downs, R.T., Blake, D.F., Vaniman, D.T., Ming, D.W., Hazen, R.M., Treiman, A.H., Achilles, C.N., Yen, A.S., Morris, R.V., Rampe, E.B., Bristow, T.F., Chipera, S.J., Sarrazin, P.C., Gellert, R., Fendrich, K.V., Morookian, J.M., Farmer, J.D., Des Marais, D.J., Craig, P.I. Crystal chemistry of martian minerals from Bradbury Landing through Naukluft Plateau, Gale crater, Mars. *Am. Mineral*. **2018**, 103 (6), 857–871.

21. Lafuente B., Downs R. T., Yang H. and Stone, N. In: Highlights in Mineralogical Crystallography, T Armbruster and R M Danisi, eds. Berlin, Germany, W. De Gruyter. 2015, pp 1-30. doi: https://rruff.info/about/downloads/HMC1-30.pdf .
22. Morris, R.V., Vaniman, D.T., Blake, D.F., Gellert, R., Chipera, S.J., Rampe, E.B., Ming, D.W., Morrison, S.M., Downs, R.T., Treiman, A.H., Yen, A.S., Grotzinger, J.P., Achilles, C.N., Bristow, T.F., Crisp, J.A., Des Marais, D.J., Farmer, J.D., Fendrich, K.V., Frydenvang, J., Graff, T.G., Morookian, J.M., Stolper, E.M., Schwenzer, S.P. Silicic volcanism on Mars evidenced by tridymite in high-SiO2 sedimentary rock at Gale crater. *P. Natl. Acad. Sci.* **2016,** 113 (26), 7071–7076.
23. Dera, P., Zhuravlev, K., Prakapenka, V., Rivers, M.L., Finkelstein, G.J., Grubor-Urosevic, O., Tschauner, O., Clark, S.M., Downs, R.T. High pressure single-crystal micro-X-ray diffraction analysis with GSE_ADA/RSV software. *High Pressure Res.* **2013,** 33 (3), 466–484.
24. Bish, D.L., Howard, S.A. Quantitative phase analysis using the Rietveld method. *J. Appl. Crystallogr.* **1988**, 21 (2), 86–91.
25. Bish, D. L. and Post, J. E. Quantitative mineralogical analysis using the Rietveld full-pattern fitting method. *Am. Mineral.* **1993,** 78 (9-10), 932–942.
26. Morrison, S.M., Downs, R.T., Blake, D.F., Prabhu, A.E., Vaniman, D.T., Ming, D.W., Rampe, E.B., Hazen, R.M., Achilles, C.N., Treiman, A.H., Yen, A.S., Morris, R.V., Bristow, T.F., Chipera, S.J., Sarrazin, P.C., Fendrich, K.V., Morookian, J.M., Farmer, J.D., Des Marais, D.J., Craig, P.I. Relationships between unit-cell parameters and composition for rock-forming minerals on Earth, Mars, and other extraterrestrial bodies. Am. Mineral. **2018**, 103 (6), 848–856.
27. Patterson, A. L. The Diffraction of X-rays by Small Crystalline Particles. *Physical Review*, **1939,** 56(10), 978. doi: https://doi.org/10.1103/PhyRev.56.978.
28. Bristow, T.F., Bish, D.L., Vaniman, D.T., Morris, R.V., Blake, D.F., Grotzinger, J.P., Rampe, E.B., Crisp, J.A., Achilles, C.N., Ming, D.W., Ehlmann, B.L., King, P.L., Bridges, J.C., Eigenbrode, J.L., Sumner, D.Y., Chipera, S.J., Morookian, J.M., Treiman, A.H., Morrison, S.M., Downs, R.T., Farmer, J.D., Des Marais, D., Sarrazin, P., Floyd, M.M., Mischna, M.A., McAdam, A.C. The origin and implications of clay minerals from Yellowknife Bay, Gale crater, Mars. *Am. Mineral.* **2015**, 100 (4), 824–836.
29. Bristow, T.F., Rampe, E.B., Achilles, C.N., Blake, D.F., Chipera, S.J., Craig, P., Crisp, J.A., Des Marais, D.J., Downs, R.T., Gellert, R., Grotzinger, J.P., Gupta, S., Hazen, R.M., Horgan, B., Hogancamp, J.V., Mangold, N., Mahaffy, P.R., McAdam, A.C., Ming, D.W., Morookian, J.M., Morris, R.V., Morrison, S.M., Treiman, A.H., Vaniman, D.T., Vasavada, A.R., Yen, A.S. Clay mineral diversity and abundance in sedimentary rocks of Gale crater, *Mars. Sci. Adv(6)* **2018**, eaar3330.
30. Vaniman, D.T., Bish, D.L., Ming, D.W., Bristow, T.F., Morris, R.V., Blake, D.F., Chipera, S.J., Treiman, A.H., Rampe, E.B., Rice, M., Achilles, C.N., Grotzinger, J.P., McLennan, S.M., Williams, J., Bell III, J.F., Newsom, H.E., Downs, R.T., Maurice, S., Sarrazin, P., Yen, A.S., Morookian, J.M., Farmer, J.D., Stack, K., Milliken, R.E., Ehlmann, B.L., Sumner, D.Y., Berger, G., Crisp, J.A., Hurowitz, J.A., Anderson, R., Des Marais, D.J., Stolper, E.M., Edgett, K.S., Gupta, S., Spanovich, N., MSL Science Team. Mineralogy of a mudstone at Yellowknife Bay, Gale crater, Mars. *Science*. **2014**, 343 (6169), 1243480.
31. Moore, D. M., and Reynolds, R. C., Jr. X-ray Diffraction and the Identification and Analysis of Clay Minerals. Oxford University Press, 400 pp., published 13 Feb. 1997. ISBN: 9780195087130.
32. Bristow, T. F., Grotzinger, J. P., Rampe, E. B., Cuadros, J., Chipera, S. J., Downs, G. W., Fedo, C. M., Frydenvang, J., McAdam, A. C., Morris R. V., Achilles, C. N., Blake, D. F., Castle, N., Craig, P., Des Marais, D. J., Downs, R. T., Hazen, R. M., Ming, D. W., Morrison, S. M., Thorpe, M. T., Treiman, A. H., Tu, V., Vaniman, D. T., Yen, A. S., Gellert, R., Mahaffy, P. R., Wiens, R. C., Byrk, A. B., Bennett, K. A., Fox, V. K., Milliken, R. E., Fraeman, A. A. and Vasvada, A. R. Brine Driven Diagenesis of Clay Minerals in Gale Crater, Mars. *Science.* **2021**, 373 (6551), 198-204; doi: https://doi.org/10.1126/science.abg5449
33. Thorpe, M. T., Bristow, T. F., Rampe, E. B., Tosca, N. J., Grotzinger, J. P., Bennett, K. A., Achilles, C. N., Blake, D. F., Chipera, S. J., Downs, G., Downs, R. T., Morrison, S. M., Tu, V., Castle, N., Craig, P., Des Marais, D. J., Hazen, R. M., Ming, D. W., Morris, R. V., Treiman, A. H., Vaniman, D. T., Yen, A. S., Vasavada, A. R., Dehouck, E., Bridges, J. C., Berger, J., McAdam, A., Peretyazhko, T., Siebach, K. L., Byrk, A. B., Fox, V. K. and Fedo, C. M. Mars Science Laboratory CheMin data from the Glen Torridon region

and the significance of lake-groundwater interactions in interpreting mineralogy and sedimentary history. *JGR Planets.* **2022**, 127 (11) doi: https://doi.org/10.1029/2021JE007099.

34. Bergmann, J. Rietveld analysis program BGMN manual. 2005, http://www.bgmn.de/BGMN_manual_2005.pdf.
35. McAdam, A. C., Sutter, B., Archer, P. D. Jr., Franz, H. B., Wong, G. M., Lewis, J. M. T., Eigenbrode, J. L., Stern, J. C., Knudson, C. A., Clark, J. V., Andrejkovicova, S., Ming, D. W., Morris, R. V., Achilles, C. N., Rampe, E. B., Bristow, T. F., Navarro-Gonzalez, R., Mahaffy, P. R., Thompson, L. M., Gellert, R., Williams, A. J., House, C. H., Johnson, S. S. Constraints on the mineralogy and geochemistry of Vera Rubin ridge, Gale crater, Mars, from Mars Science Laboratory Sample Analysis at Mars evolved gas analyses. *J. Geophys., Res.: Planets, 125*. **2020**, doi: https://doi.org/10.1029/2019JE006309.
36. Chipera, S.J., Bish, D.L. FULLPAT: a full-pattern quantitative analysis program for X-ray powder diffraction using measured and calculated patterns. *J. Appl. Crystallogr. 35.* 2002, (6), 744–749.
37. Chipera, S.J., Bish, D.L. Fitting full X-ray diffraction patterns for quantitative analysis: a method for readily quantifying crystalline and disordered phases. *Adv. Mater. Phys. Chem.* **2013,** 3 (01), 47.
38. Achilles C. N., Morris R. V., Chipera S. J., Ming D. W. and Rampe E. B. Lunar and Planetary Science Conference 44. X-ray diffraction reference intensity ratios of amorphous and poorly crystalline phases: Implications for CheMin on the Mars Science Laboratory Mission. Houston, Texas, USA, March 18-22, 2013, Abstr. # 3072. Available at: https://www.lpi.usra.edu/meetings/lpsc2013/pdf/3072.pdf
39. Rampe E.B. Bish D.L. Chipera S.J. Morris R.V. Achilles C.N. Ming D.W. Blake D.F. Anderson R.C. Bristow T.F. Crisp J.A. Des Marais D.J. Downs R.T. Farmer J.D. Morookian J.M. Morrison S.M. Sarrazin P.C. Spanovich N. Stolper E.M. Treiman A.H. Vaniman D.T. Yen A.S. and the MSL Science Team. Detecting Nanophase Weathering Products with CheMin: Reference Intensity Ratios of Allophane, Aluminosilicate Gel, and Ferrihydrite. Lunar and Planetary Science Conference 44, abstr. # 1188. Houston, Texas, USA, March 18th through 22nd, 2013. Available at: https://www.lpi.usra.edu/meetings/lpsc2013/pdf/1188.pdf.
40. Smith, R. J., Rampe, E. B., Horgan, B. H. N., & Dehouck, E. Deriving amorphous component abundance and composition of rocks and sediments on Earth and Mars. *Journal of Geophysical Research: Planets*. **2018**, 123(10), 2485–2505. doi: https://doi.org/10.1029/2018JE005612.
41. Blake, D. F., Morris, R. V., Kocurek, G., Morrison, S. M., Downs, R. T., Bish, D. L., Ming, D. W., Edgett, K. S., Rubin, D., Goetz, W., Madsen, M. B., Sullivan, R., Gellert, R., Campbell, I., Treiman, A. H., McLennan, S. M., Yen, A. S., Grotzinger, J., Vaniman, D. T., Chipera, S. J., Achilles, C. N., Rampe, E. B., Sumner, D., Meslin, P.-Y., Maurice, S., Forni, O., Gasnault, O., Fisk, M., Schmidt, M. Mahaffy, P., Leshin, L. A., Glavin, D., Steele, A., Freissinet, C., Navarro-Gonzalez, R., Yingst, R. A., Kah, L. C., Bridges, N., Lewis, K.W., Bristow, T.F., Farmer, J.D., Crisp, J. A., Stolper, E. M., Des Marais, D. J., Sarrazin, P. and the MSL Science Team. Characterization and analysis of the Rocknest sand shadow. *Science.* **2013,** 341, doi: https://doi.org/10.1126/science.1239505.
42. Bish, D. L., Blake, D. F., Vaniman, D. T., Chipera, S. J., Morris, R. V., Ming, D. W., Treiman, A. H., Sarrazin, P., Morrison, S. M., Downs, R. T., Achilles, C., N., Yen, A. S., Bristow, T. F., Crisp, J. A., Morookian, J. M., Farmer, J. D., Rampe, E. B., Stolper, E. M., Spanovich, N. and the MSL Science Team. X-ray diffraction results from Mars Science Laboratory: Mineralogy of Rocknest at Gale crater. *Science.* **2013**, 341, 1238932. doi: https://doi.org/10.1126/science.1238932.
43. Bish, D .L., Blake, D. F., Vaniman, D. T., Sarrazin, P., Bristow, T. F., Achilles, C. N., Dera, P., Chipera, S. J., Crisp, J., Downs, R. T., Farmer, J., Gailhanou, G., Ming, D., Morookian, J. M., Morris, R., Morrison, S., Rampe, E., Treiman, A. and Yen, A. The first X-ray diffraction measurements on Mars. *IUCrJ.* **2014**, 1, 514-522. doi: https://doi.org/10.1107/S2052252514021150.
44. Achilles, C. N., Downs, R. T., Ming, D. W., Rampe, E. B., Morris, R. V., Treiman, A. H., Morrison, S. M., Blake, D. F., Vaniman, D. T., Ewing, R. C., Chipera, S. J., Yen, A. S., Bristow, T. F., Ehlmann, B. L., Gellert, R., Hazen, R. M., Fendrich, K.V., Craig, P. I., Grotzinger, J. P., Des Marais, D. J., Farmer, J. D., Sarrazin, P. C., Morookian, J. M. Mineralogy of an active eolian sediment from the Namib dune, Gale crater, Mars. *J. Geophys. Res. Planets.* **2017**, 122, 2344-2361. doi: https://doi.org/10.1002/2017JE005262.

45. Ehlmann, B. L., Edgett, K. S., Sutter, B., Achilles, C. N., Litvak, M. L., Lapotre, M. G. A., Sullivan, R., Fraeman, A. A., Arvidson, R. E., Blake, D. F., Bridges, N. T., Conrad, P. G., Cousin, A., Downs, R. T., Grabriel, T. S. J., Gellert, R., Hamilton, V. E., Hardgrove, C., Johnson, J. R., Kuhn, S., Mahaffy, P. R., Maurice, S., McHenry, M., Meslin, P. -Y., Ming, D. W., Minitti, M. E., Morookian, J. M., Morris, R. V., O'Connell-Cooper, C. D., Pinet, P. C., Rowland, S. K., Shhroeder, S., Siebach, K. L., Stein, N. T., Thompson, L. M., Vaniman, D. T., Vasvada, A. R. and Wellington, D. F. Chemistry, mineralogy, and grain properties at Namib and High dunes, Bagnold dune field, Gale crater, Mars: A synthesis of Curiosity rover observations. *J. Geophys. Res. Planets*. **2017**, 122, 2510-2543. doi: https://doi.org/10.1002/2017JE005267.
46. Lapotre, M. G. A., and Rampe, E. B. Curiosity's Investigation of the Bagnold Dunes, Gale Crater: Overview of the Two-Phase Scientific Campaign and Introduction to the Special Collection. *Geophys. Res. Lett.* **2018**, 45. doi: https://doi.org/10.1029/2018GL079032.
47. Rampe, E. B., Lapotre, M. G. A., Bristow, T. F., Arvidson, R. E., Morris, R. V., Achilles, C. N., Weitz, C., Blake, D. F., Ming, D. W., Morrison, S. M. Vaniman, D. T., Chipera, S. J., Downs, R. T., Grotzinger, J. P., Hazen, R. M., Peretyazhko, T. S., Sutter, B., Tu, V., Yen, A. S., Horgan, B., Castle, N., Craig, P. I., Des Marais, D. J., Farmer, J., Gellert, R., McAdam, A. C., Morookian, J. M., Sarrazin, P. C. and Treiman, A. H. *J. Geophys. Res. Planets*. **2018**, 45. doi: https://doi.org/10.1029/2018GL079073.
48. Herkenhoff, K. E., Grotzinger, J., Knoll A. H., McLennan, S. M., Weitz, C., Yingst, A., Anderson, R., Archinal, B. A., Arvidson, R. E., Barrett, J. M., Becker, K. J., Bell III, J. F., Budney, C., Chapman, M. G., Cook, D., Ehlmann, B., Franklin, B., Gaddis, L. R., Galuszka, D. M., Garcia, P. A., Geissler, P., Hare, T. M., Howington-Kraus, E., Johnson, J. R., Keszthelyi, L., Kirk, R. L., Lanagan, P., Lee, E. M., Leff, C., Maki, J. M., Mullins, K. F., Parker, T., J., Redding, B. L., Roseik, M. R., Sims, M. H., Soderblom, L. A., Spanovich, N., Springer, R., Squyres, S. W., Stolper, D., Sucharski, R. M., Sucharski, T., Sullivan, R. and Torsoon, J. M. Surface processes recorded by rocks and soils on Meridiani Planum, Mars: Microscopic Imager observations during Opportunity's first three extended missions. *J. Geophys. Res*. **2008**, 113(E12). doi: https://doi.org/10.1029/2008JE003100.
49. Sullivan, R., Banfield, D., Bell, J.F. III, Calvin, W., Fike, D., Golombek, M., Greeley, R., Grotzinger, J., Herkenhoff, K., Jerolmack, D., Malin, M., Ming, D., Soderblom, L. A., Squyres, S. W., Thompson, S., Watters, W. A., Weitz, C. M. and Yen, A. Aeolian processes at the Mars exploration rover Meridiani Planum landing site. *Nature.* **2005**, 436, 58–61. doi: https://doi.org/10.1038/nature03641
50. Sullivan, R., Arvidson, R., Bell, J. F. III, Gellert, R., Golombek, M., Greeley, R., Herkenhoff, K., Johnson, J., Thompson, S., Whelley, P. and Wray, J. Wind‐driven particle mobility on Mars: Insights from Mars Exploration Rover observations at "El Dorado" and surroundings at Gusev Crater. *J. Geophys. Res*. **2008**, 113, E06S07. doi: https://doi.org/10.1029/2008JE003101
51. Solderblom, L. A., Anderson, R. C., Arvidson, R. E., Bell, J. F. III, Cabrol, N. A., Calvin, W., Christensen P. R., Clark, B. C., Economou, T., Ehlmann, B. L., Farrand, W. H., Fike, D., Gellert, R., Glotch, T. D., Golombek, M. B., Greeley, R., Grotinger, J. P. Herkenhoff, K. E., Jerolmack, D. J. Johnson, J. R., Joliff, B., Klingelhoffer, G., Knoll, A. H., Learner, Z. A., Li, R., Malin, M. C., McLennan, S. M., McSween, H. Y., Ming, D. W., Morris, R. V., Rice, J. W. Jr, Richer, L., Rieder, R., Rodionov, D., Schroder, C., Seelos, F. P. IV, Soderblom, J. M., Squyres, S. W., Sullivan, R., Watters, W. A., Weitz, C. M., Wyatt, M. B., Yen, A. and Zipfel, J. *Science.* **2004**, 306, 1723–1726. doi: https://doi.org/10.1126/science.1105127
52. Golombek, M., Robinson, K., McEwen, A., Bridges, N., Ivanov, B., Tornabene, L. and Sullivan, R. Constraints on ripple migration at Meridiani Planum from Opportunity and HiRISE observations of fresh craters. *J. Geophys. Res*. **2010**, 115, E00F08. doi: https://doi.org/10.1029/2010JE003628.
53. Ward, W. R. Large-scale variations in the obliquity of Mars. *Science*. **1973**, 181(4096), 260-262. doi: http://doi.org/10.1126/science.181.4096.260
54. Laskar, J., Levrard, B and Mustard, J. F. Large-scale variations in the obliquity of Mars. *Nature.* **2002**, 419, 375-377. doi: https://doi..org/10.1038/nature01066

55. Laue, M., Friedrich, W. and Knipping, P. Die Wellentheorie der Röntgenstrahlen. **1912**, Sitzungsb. k. Bayer. Akad. Wiss., math.-phys. Klasse 303-322
56. Ming, D.W., Gellert, R., Morris, R. V., Arvidson, R. E., Bruckner, J., Clark, B. C., Cohen, B. A., d'Uston, C., Economou, T., Fleischer, I., Klingelhofer, G., McCoy, T. J., Mittlefehldt, D. W., Schmidt, M. E., Schroder, C., Squyers, S. W., Treguier, E., Yen, A. S., Ipfel, A.S. Geochemical properties of rocks and soils in Gusev crater, mars: results of the alpha particle X - ray spectrometer from Cumberland Ridge to home plate. *J. Geophys. Res.* **2008**, 113, E12S39. doi: https://doi.org/10.1029/2008JE003195
57. Morris, R.V., Klingelhoffer, G., Schroder, C., Fleischer, I., Ming, D. W., Yen, A. S., Gellert, R., Arvidson, R. E., Rodionov, D. S., Crumpler, L. S., Clark, B. C., Cohen, B. A., McCoy, T. J., Mittlefehldt, D. W., Schmidt, M. E., de Souza, P. A. Jr., Squyres, S. W. Iron mineralogy and aqueous alteration from Husband Hill through Home Plate at Gusev crater, Mars: Results from the Mössbauer instrument on the Spirit Mars Exploration Rover. *J. Geophys. Res.* **2008**, 113, E12S42. doi: https://doi.org/10.1029/2008JE003201.
58. McSween, H. Y. Jr., Taylor, G. J. and Wyatt, M. B. Elemental composition of the Martian crust. *Science*. **2009**, 324, 736–739. doi: https://doi.org/10.1126/science.1165871
59. Taylor, S. R. and McLennan, S. M. Planetary Crusts: Their Composition, Origin and Evolution. Cambridge Univ. Press, Cambridge. **2009,** 378 p.
60. Leshin, L.A., P.R. Mahaffy, C.R. Webster, M. Cabane, P. Coll, P.G. Conrad, P.D. Archer Jr., S.K. Atreya, S.K., A.E. Brunner, A. Buch, J.L. Eigenbrode, G.J. Flesch, H.B. Franz, C. Freissinet, D.P. Glavin, A.C. McAdam, K.E. Miller, D.W. Ming, R.V. Morris, R. Navarro-González, P.B. Niles, T. Owen, R.O. Pepin, S. Squyres, A. Steele, J.C. Stern, R.E. Summons, D.Y. Sumner, B. Sutter, C. Szopa, S. Teinturier, M.G. Trainer, J.J. Wray, J.P. Grotzinger, and the MSL Science Team. Volatile, isotope, and organic analysis of martian fines with the Mars Curiosity rover. *Science*. **2013**, 341, 1238937. doi: http://doi.org/10.1126/science.1238937
61. Rice, M. S., Gupta, S., Treiman, A. H., Stack, K. M., Calef, F., Edgar, L. A., Grotzinger, J., Lanza, N., Le Deit, L., Lasue, J., Siebach, K. L., Vasavada, A., Wiens, R. C. and Williams, J. Geologic overview of the Mars Science Laboratory rover mission at the Kimberley, Gale crater, Mars. Journal of *Geophys. Res. Planets*. **2017**, 122(1):2-20. doi: https://doi.org/10.1002/2016JE005200
62. Williams, R.M.E., Grotzinger, J. P., Dietrich, W. E., Gupta, S., Sumner, D. Y., Wiens, R. C., Mangold, N., Malin, M. C., Edgett, K. S., Maurice, S., Forni, O., Gasnault, O., Ollila, A., Newsom, H. E., Dromart, G., Palucis, M. C., Yingst, R. A., Anderson, R. B., Herkenhoff, K. E., Le Mouélic, S., Goetz, W., Madsen, M. B., Koefoed,, A., Jensen,, J. K., Bridges, J. C., Schwenzer, S. P., Lewis, K. W., Stack, K. M., Rubin, D., Kah, L. C., Bell, J. F. III, Farmer, J. D., Sullivan, R., Van Beek, T., Blaney, D. L., Pariser, O., Deen, R. G. and MSL Science Team. Variability in martian sinuous ridge form: Case study of Aeolis Serpens in the Aeolis Dorsa, Mars, and insight from the Mirackina paleoriver, South Australia *Science*. **2013**, 340(6136):1068-1072. doi: https://doi.org/10.1126/science.1237317.
63. Treiman, A. H., Morris, R. V., Agresti, D. G., Graff, T. G., Achilles, C. N., Rampe, E. B., Bristow, T. F., Ming, D. W., Blake, D. F., Vaniman, D. T., Bish, D. L., Chipera, S. J., Morrison, S. M., Downs, R. T. Ferrian saponite from the Santa Monica Mountains (California, USA, Earth): Characterization as an analog for clay minerals on Mars with application to Yellowknife Bay in Gale Crater. *Am. Min.* **2014**, 99, 2234-2250. doi: https://doi.org/10.2138/am-2014-4763.
64. Farley, K.A., Malespin, C., Mahaffy, P., Grotzinger, J. P., Vasconcelos, P., Milliken, R.E., Malin, M., Edgett, K. S., Pavlov, A. A., Hurowitz, J. A., Grant, J. A., Miller, H. B., Arvidson, R., Beegle, L., Calef, F., Conrad, P. G., Dietrich, W. E., Eigenbrode, J., Gellert, R., Gupta, S., Hamilton, V., Hassler, D. M., Lewis, K. W., McLennan, S. M., Ming, D. M., Navarro-González, R., Schwenzer, S. P., Steele, A., Stolper, E. M., Sumner, D. Y., Vaniman, D., Vasavada, A., Williford, K., Wimmer-Schweingruber, R. F. and the MSL Science Team. In situ radiometric and exposure age dating of the Martian surface. *Science*. **2014**, 343(6169), 1247166. doi: 10.1126/science.1247166.

65. Ehlmann, B. L., Mustard, J. F., Murchie, S. L., Bibring, J-P., Meunier, A., Fraeman, A. A. and Langevin, Y. Evidence for low-grade metamorphism, hydrothermal alteration, and diagenesis on Mars from phyllosilicate mineral assemblages. *Nature*. **2011**, 479 53-60. doi: https://doi.org/10.1038/nature10582.
66. Grotzinger, J.P., Sumner, D.Y., Kah, L.C., Stack, K., Gupta, S., Edgar, L., Rubin, D., Lewis, K., Schieber, J., Mangold, N. and Milliken, R. A habitable fluvio-lacustrine environment at Yellowknife Bay, Gale Crater, Mars. *Science*. **2014**, 343(6169), p.1242777.
67. Treiman, A. H., Bish, D. L., Vaniman, D. T., Chipera, S. J., Blake, D. F., Ming, D. W., Morris, R. V., Bristow, T. F., Morrison, S. M., Baker, M. B., Rampe, E. B., Downs, R. T., Filiberto, J., Glazner, A. F., Gellert, R., Thompson, L. M., Schmidt, M. E., Le Deit, L., Wiens, R. C., McAdam, A. C., Achilles, C. N., Edgett, K. S., Farmer, J. D., Fendich, K. V., Grotzinger, J. P., Gupta, S., Morookian, J. M., Newcombe, M. E., Rice, M. S., Spray, J. G., Stolper, E. M., Sumner, D. Y., Vasavada, A. R. and Yen, A. S. Mineralogy and genesis of the Windjana sandstone, Kimberley area, Gale Crater, Mars. *JGR Planets*. **2015**, 121(1), 75-106. doi: https://doi.org/10.1002/2015JE004932
68. Tu, V.M., Rampe, E. B., Bristow, T. F., Thorpe, M. T., Clark, J. V., Castle, N., Fraeman, A. A., Edgar, L. A., McAdam, A., Bedford, C., Achilles, C. N., Blake, D., Chipera, S. J., Craig, P. I., Des Marais, D. J., Downs, G. W., Downs, R. T., Fox, V., Grotzinger, J. P., Hazen, R. M., Ming, D. W., Morris, R. V., Morrison, S. M., Pavri, B., Eigenbrode, J., Peretyazhko, T. S., Sarrazin, P., Sutter, B., Treiman, A. H., Vaniman, D. T., Vasavada, A. R., Yen, A. S., and Bridges, J. C. A Review of the Phyllosilicates in Gale Crater as Detected by the CheMin Instrument on the Mars Science Laboratory, Curiosity Rover. *Minerals.* **2021**, (8). doi: https://doi.org/10.3390/min11080847
69. Mangold, N. M., Dehouck, E., Forni, O., Fedo, C., Achilles, C., Bristow, T., Frydevang, J., Gasnault, O., Haridon, J. L., Le Deit, L., Maurice, S., McLennan, S. M., Meslin, P. Y., Morrison, S., Newsom, H. E., Rampe, E., Rivera-Hernandez, F., Salvatore, M., Wiens, R. C. Chemical alteration of fine-grained sedimentary rocks at Gale crater. Fourth International Conference on Early Mars, Flagstaff, ZA, USA, 10/2-10/2017, abstr. #3013. Bibcode 2017LPICo2014,3013M
70. Fedo, C., Grotzinger, J., Gupta, S., Stein, N. T., Watkins, J., Banham, S., Edgett, K. S., Minitti, M., Schieber, J., Sebach, K., Stack-Morgan, K., Newsom, H., Lewis, K. W., House, C., Vasavada, A.R. Facies Analysis and Basin Architecture of the Upper Part of the Murray Formation, Gale Crater, MarsLunar and Planetary Science Conference 48. 2017, Abstr. #1689. Available at: https://www.hou.usra.edu/meetings/lpsc2017/pdf/1689.pdf
71. Stein, N., Grotzinger, J. P., Schieber, J., Mangold, N., Newsom, H., Minitti, M., Sumner, D., Edgett, K. S., Stack, K., Fedo, C., Gupta, S., Hallet, B., Vasavada, A. and Fey, D. Facies Analysis and Basin Architecture of the Upper Part of the Murray Formation, Gale Crater, Mars. Lunar and Planetary Science Conference. 2017, 48, abstr. # 2387. Available at: https://www.hou.usra.edu/meetings/lpsc2017/pdf/2387.pdf
72. Rampe, E. B., Bristow, T. F., Morris, R. V., Morrison, S. M., Achilles, C. N., Ming, D. W., Vaniman, D. T., Blake, D. F., Tu, V. M., Chipera, S. J., Yen, A. S., Peretyazhko, T. S., Downs, R. T., Hazen, R. M., Treiman, A. H., Grotzinger, J. P., Castle, N., Craig, P. I., Des Marais, D. J., Thorpe, M. T., Walroth, R. C., Downs, G. W., Fraeman A. A., Siebach, K. L., Gellert, R., Lafuente, B., McAdam, A. C., Meslin, P. -Y., Sutter, B and Salvatore, M. R. *J. Geophys. Res*: *Planets*. 2020, 125, e2019JE006306. doi: https://doi.org/10.1029/2019JE006306
73. Stack, K. M., Grotzinger, J. P., Lamb, M. P., Gupta, S., Rubin, D. M., Kah, L. C., Edgar, L. A., Fey, D. M., Hurowitz, J. A., McBride, M., Rivera-Hernandez, F., Sumner, D. Y., Van Beek, J. K., Williams, R. M. E., Yingst, R. A. Evidence for plunging river plume deposits in the Pahrump Hills member of the Murray formation, Gale crater, Mars. *Sedimentology*. **2019**, 66(5), 1768-1802. doi: https://doi.org/10.1111/sed.12558
74. Rampe, E. B., Ming, D. W., Blake, D. F., Bristow, T. F., Chipera, S. J., Grotzinger, J. P., Morris, R. V., Morrison, S. M., Vaniman, D. T., Yen, A. S., Achilles, C. N., Craig, P. I., Des Marais, D. J., Downs, R. T., Farmer, J. D., Fendrich, K. V., Gellert, R., Morookian, J. M., Peretyazhko, T. S., Sarrazin, P., Treiman, A. H., Berger, J. A., Eigenbrode, J. L., Fairén, A. G., Forni, O., Gupta, S., Hurowitz,

J. A., Kah, L. C., Lanza, N. L., Schmidt, M. E., Siebach, K., Sutter, B., and Thompson, L. C. *Earth and Planetary Science Letters*. **2017**, 471, pp 172-185. doi: https://doi.org/10.1016/j.epsl.2017.04.021

75. Grotzinger, J.P., Gupta, S., Malin, M. C., Rubin, D. M., Schieber, J., Siebach, K., Sumner, D. Y., Stack, K. M., Vasavada, A. R., Arvidson, R. E., Calef, F. III, Edgar, L., Fischer, W. F., Grant, J. A., Griffes, J., Kah, L. C., Lamb, M. P., Lewis, K. W., Mangold, N., Minitti, M. E., Palucis, M., Rice, M., Williams, R. M. E., Yingst, R. A., Blake, D., Blaney, D., Conrad, P., Crisp, J., Dietrich, W. E., Dromart, G., Edgett, K. S., Ewing, R. C., Gellert, R., Hurowitz, J. A., Kocurek, G., Mahaffy, P., McBride, M. J., McLennan, S. M., Mischna, M., Ming, D., Milliken, R., Newsom, H., Oehler, D., Parker, T. J., Vaniman, D., Wiens, R. C., and Wilson, S. A. *Science*. **2015**, 350(6257):aac7575. doi: https://doi.org/10.1126/science.aac7575
76. Murad, E. and Cashion, J. Mössbauer spectroscopy of environmental materials and their industrial utilization. *Springer, New York, NY*. **2004**, doi: https://doi.org/10.1007/978-1-4419-9040-2
77. Jolivet, J.-P. and Tronc, E. J. Interfacial electron transfer in colloidal spinel iron oxide. Conversion of Fe3O4-γFe2O3 in aqueous medium. *Colloid Interf. Sci.* **1988**, 125, 688–701. https://dx.doi.org/10.1016/0021-9797(88)90036-7
78. Hurowitz, J.A., Grotzinger, J. P., Fischer, W. W., McLennan, S. M., Milliken, R. E., Stein, N., Vasavada, A. R., Blake, D. F., Dehouck, E., Eigenbrode, J. L., Fairén, A. G., Frydenvang, F., Gellert, R., Grant, J. A., Gupta, S., Herkenhoff, K. E., Ming, D. W., Rampe, E. B., Schmidt, M. E., Siebach, K. L., Stack-Morgan, K. Sumner, D. Y. and Wiens, R. C. Redox stratification of an ancient lake in Gale crater, Mars. *Science.* **2017**, 356(6341):eah6849. doi: https://doi.org/10.1126/science.aah6849
79. Martin, P. E., Farley, K. A., Baker, M. B., Malespin, C.A., Schwenzer, S. P., Cohen, B. A., Mahaffy, P. R., McAdam, A. C., Ming, D. W., Vasconcelos P. M. and Navarro-Gonzalez, R. A two‐step K‐Ar experiment on Mars: Dating the diagenetic formation of jarosite from Amazonian groundwaters. *J. Geophys. Res. – Planets*. **2017**, 122 (12), 2803–2818. doi: https://doi.org/10.1002/2017JE005445
80. Payré, V., Siebach, K. L., Thorpe, M. T., Antoshechkina, P. and Rampe, E. B. Tridymite in a lacustrine mudstone in Gale Crater, Mars: Evidence for an explosive silicic eruption during the Hesperian. *EPSL.* **2022,** 594, article 117694. doi: https://doi.org/10.1016/j.epsl.2022.117694
81. Yen, A. S., Morris, R. V., Ming, D. W., Schwenzer, S. P., Sutter, B., Vaniman, D. T., Treiman, A. H., Gellert, R., Achilles, C. N., Berger, J. A., Blake, D. F., Boyd, N. I., Bristow, T. F., Chipera, S., Clark, B. C., Craig, P. I., Downs, R. T., Franz, H. B., Gabriel, T., McAdam, A. C., Morrison, S. M., O'Connell-Cooper, C. D., Rampe, E. B., Schmidt, M. E., Thompson, L., M. and VanBommel. Formation of tridymite and evidence for a hydrothermal history at gale crater, Mars. *S. J. Journal of Geophysical Research:Planets*. **2021**, 126, e2020JE006569. https://doi.org/10.1029/2020JE006569
82. Watkins, J. A., Grotzinger, J. P., Stein, N.T., Banham, S. G., Gupta, S., Rubin, D.M., Stack-Morgan, K., Edgett, K. S., Frydenvang, J., Siebach, L., Lamb, M. P., Sumner, D. Y., and Lewis, K. W. Journal of *Geophys. Res. Planets*. **2022**, 127, e2022JE007293. doi: https://doi.org/10.1029/2022JE007293
83. Banham, S. G., Gupta, S., Rubin, D. M., Watkins, J. A., Sumner, D. Y., Edgett, K. S., Grotzinger, J. P., Lewis, K. W., Edgar, L. A., Stack-Morgan, K. M., Barnes, R., Bell J. F. III , Day, M. D., Ewing, R. C., Mathieu, G. A., Lapotre, N. T., Riviera-Hernandez, F. and Vasavada, A. R. Ancient Martian aeolian processes and palaeomorphology reconstructed from the Stimson formation on the lower slope of Aeolis Mons, Gale crater, Mars. *Sedimentology.* **2018**, 65(4), 993–1042. doi: https://doi.org/10.1111/sed.12469
84. Banham, S. G., Gupta, S., Rubin, D. M., Bedford, C. C., Edgar, L. A., Bryk, A. B., Dietrich, W. E., Fedo, C. M., Williams, R. M., Caravaca, G., Barnes, R., Paar, G., Ortner, T. and Vasada, A. R. *Journal of Geophys. Res. Planets.* **2022,** 127, e2021JE007023. doi: https://doi.org/10.1029/2021JE007023
85. Yen, A. S., Ming, D. W., Vaniman, D. T., Gellert, R., Blake, D. F., Morris, R. V., Morrison, S. M., Bristow, T. F., Chipera, S. J., Edgett, K. S., Treiman, A. H., Clark, B. C., Downs, R. T., Farmer, J. D., Grotzinger, J. P., Rampe, E. B., Schmidt, M.

E., Sutter, B. and Thompson, L. M. Multiple stages of aqueous alteration along fractures in mudstone and sandstone strata in Gale Crater, Mars. *EPSL.* **2017**. 471, 186-198. doi: http://dx.doi.org/10.1016/j.epsl.2017.04.033

86. Szczerba, M., Rampe, E. B., Peretyazhko, T. S., Bristow, T. F., Morris, R. V., Blake, D. F., Vaniman, D. T., Chipera, S. J., Downs, R. T., Hazen, R. M., Ming, D. W., Morrison, S. M., Treiman, A. H., Yen, A. S., Tu, V. M., Thorpe, M. T., Achilles, C. N., Des Marais, D. J., Grotzinger, J. P, Castle, N., Craig, P., C., Hausrath, E. M., Simpson, S. L. and Tutolo, B. Hematite Formation and Growth in Gale crater Seen Through MSL CheMin X-ray Diffraction Data. LPSC 54. 2023, abstr. # 1959. Available at: https://www.hou.usra.edu/meetings/lpsc2023/pdf/1956.pdf
87. Bibring, J. P., Langevin, Y., Mustard, J. F., Poulet, F., Arvidson, R., Gendrin, A., Gondet, B., Mangold, N., Pinet, P., Forget, F., Berthe, M., Gendrin, A., Gomez, C., Gondet, B., Jouglet, D., Poulet, F., Soufflot, A., Vincendon, M., Combes, M., Drossart, P., Encrenaz, T., Fouchet, T., Merchiorri, R., Belluci, G., Alteieri, F., Formisano, V., Capaccioni, F., Cerroni, P., Coradini, A., Fonti, S., Korablev, O., Kottsov, V., Ignatiev, N., Moroz, V., Titov, D., Zasova, L., Loiseau, D., Mangold, N.,Pinet, P., Soute, S., Schmitt, B., Sotin, C., Hauber, E., Hoffmann, H., Jaumann, R., Keller, U., Arvidson, R., Mustard, J.F., Duxbury, T. and Neukum, G. Global mineralogical and aqueous Mars history derived from OMEGA/Mars Express data. *Science.* **2006**, 312 (5772), 400–404. doi: https://doi.org/10.1126/science.1122659
88. Ehlmann, B. L. and Edwards, C. S. Mineralogy of the Martian surface. Annual Review of *EPSL*. **2014,** 42:1, 291-315. doi: https://doi.org/10.1146/annurev-earth-060313-055024
89. Bishop, J. L., Lane, M. D., Dyar, M. D., and Borwn, A. J. Reflectance and emission spectroscopy study of four groups of phyllosilicates: Smectites, kaolinite-serpentines, chlorites and mica. *Clay Minerals.* **2008**, 43(1), 35-54. doi: https://doi.org/10.1180/claymin.2008.043.1.03
90. Grant, J. A., Irwin, R. P. III, Grotzinger, J. P., Milliken, R. E., Tornabene, L. L., McEwen, A. S., Weitz, C. M., Squyres, S. W., Glotch, T. D. and Thompson, B. J. HiRISE imaging of impact megabreccia and sub-meter aqueous strata in Holden Crater, Mars. *Geology.* **2008**, 36(3), 195-198. Doi: https://doi.org/10.1130/G24340A.1
91. Milliken, R.E. and Bish, D.L. Sources and sinks of clay minerals on Mars. *Philosophical Magazine.* **2010**, 90(17-18), pp.2293-2308.
92. Murchie, S. L., Mustard, J. F., Ehlmann, B. L., Milliken, R. E., Bishop, J. L., McKeown, N. K., Noe Dobrea, E. Z., Seelos, F. P., Buczkowski, D. L., Wiseman, S. M., Arvidson, R. E., Wray, J. J., Swayze, G., Clark, R. N., Des Marais, D. J., McEwen, A. S. and Bibing, J.-P. A synthesis of Martian aqueous mineralogy after 1 Mars year of observations from the Mars Reconnaissance Orbiter. *JGR Planets*. **2009,** 114, E2. doi: https://doi.org/10.1029/2009JE003342
93. Fedo, C. M., Bryk, A. B., Edgar, L. A., Bennett, K. A., Fox, V. K., Dietrich, W. E., Banham, S. G., Gupta, S., Stack, K. M., Williams, R. M. E., Grotzinger, J. P., Stein, N. T., Rubin, D. M., Caravaca, G., Arvidson, R. E., Hughes, M. N., Fraeman, A. A., Vasavada, A. R., Schieber, J., Sutter, B. Geology and stratigraphic correlation of the Murray and Carolyn Shoemaker formations across the Glen Torridon region, Gale crater, Mars. *J. Geophys. Res. Planets.* **2022,** 127(9). doi: https://doi.org/10.1029/2022JE007408.
94. Downs, R.T. and Hall-Wallace, M. The American Mineralogist crystal structure database. *Am Mineral.* **2003**, 95, 247-250. doi: https://doi.org/10.2138/am.2010.3470
95. Sheppard, R. Y., Milliken, R. E., Parente, M., and Itoh, Y. Updated perspectives and hypotheses on the mineralogy of lower Mt. Sharp, Mars, as seen from orbit. *J. Geophys. Res. Planets*. **2021**, 126, e2020JE006372. doi: https://doi.org/10.1029/2020JE006372
96. Rampe, E. B., Bristow, T. F., Blake, D. F., Chipera, S. J., Vaniman, D. T., Achilles, C. N., Downs, R. T., Ming, D. W., Morris, R. V., Morrison, S. M., Simpson, S. L., Tu, V. M., Thorpe, M. T., Yen, A. S., Des Marais, D. J., Downs, G.1, Grotzinger, J. P., Hazen, R. M., Treiman, A. H., Castle, N., Craig, P. I., Hausrath, E. M., Peretyazhko, T. S., Tutolo, B., M. Szczerba, M., Berger, J.A., Clark, J. V., Edgar, L. A., Rapin, W., B. Sutter, B. Mineralogical Evidence for Environmental Change in the Clay-Sulfate Transition at Gale crater, Mars. LPSC, Houston, Texas, USA. 3/13-3/17 2023, 54, Abstr. #1554. Available at: https://www.hou.usra.edu/meetings/lpsc2023/pdf/1554.pdf

97. Chipera, S. J., Vaniman, D. T., Rampe, E. B., Bristow, T. F., Martínez, G., Tu, V. M., Peretyazhko, T. S., Yen, A. S., Gellert, R., Berger, J. A., Rapin, W., Morris, R. V., Ming, D. W., Thompson, L. M., Simpson, S., Achilles, C. N., Tutolo, B., Downs, R. T., Fraeman, A. A., Fischer, E., Blake, D. F., Treiman, A. H., Morrison, S. M., Thorpe, M. T., Gupta, S., Dietrich, W. E., Downs, G., Castle, N., Craig, P. I., Des Marais, D. J., Hazen, R. M., Vasavada, A. R., Hausrath, E., Sarrazin, P. and Grotzinger, J. P. Mineralogical Investigation of Mg‐Sulfate at the Canaima Drill Site, Gale Crater, Mars. *JGR Planets*. **2023,** 128, e2023JE008041. doi: https://doi.org/10.1029/2023JE008041
98. Chipera, S. J. and Vaniman, D. T. Experimental stability of magnesium sulfate hydrates that may be present on Mars. *GCA,* **2007**, 71(1), 241–250. doi: https://doi.org/10.1016/j.gca.2006.07.044
99. Vaniman, D. T. and Chipera, S. J. Transformations of Mg-and Ca-sulfate hydrates in Mars regolith. *Am. Min.* **2006**, 91(10), 1628–1642. doi: https://doi.org/10.2138/am.2006.2092
100. Vaniman, D. T., Chipera, S. J., Bish, D. L. and Peterson, R. C. The Todilto Formation and Science Goals at North Meridiani. 7th International Conference on Mars. LPI Contribution No. 1353, 2007, Abstract #3156. Houston, Texas, USA. Bibcode: 2007LPICo1353.3156V
101. Wang, A., Freeman, J. J., & Jolliff, B. L. Formation Rate of Amorphous Magnesium Sulfates at Low Temperatures Approaching the Current Surface Conditions on Mars. LPSC 38. 3/12-3/16, 2007 Houston, Texas, USA, Abstr. #1195. Available at: https://www.lpi.usra.edu/meetings/lpsc2007/pdf/1195.pdf
102. Wang, A., Freeman, J. J. and Jolliff, B. L. (2009). Phase transition pathways of the hydrates of magnesium sulfate in the temperature range 50°C to 5°C: Implication for sulfates on Mars. *JGR.* **2009**, 114(E4), E04010. doi: https://doi.org/10.1029/2008JE003266
103. Wang, A., Freeman, J. J., Chou, I.-M. and Jolliff, B. L. Stability of Mg-sulfates at −10°C and the rates of dehydration/rehydration processes under conditions relevant to Mars *JGR.* **2011**, 116(E12), E12006. doi: https://doi.org/10.1029/2011JE003818
104. Vaniman, D. T., Martinez, G. M., Rampe, E. B., Bristow, T. F., Blake, D. F., Yen, A. S, Ming, D. W., Rapin, W., Meslin, P.-Y., Morookian, J. M., Downs, R. T., Chipera, S. J., Morris, R. V., Morrison, S. M., Treiman, A. H., Achilles, C. N., Robertson, K., Grotzinger, J. P., Hazen, R. M., Wiens, R. C. and Sumner, D. Y. Gypsum, bassanite, and anhydrite at Gale crater, Mars. *Am. Min.* **2018,** 103(7), 1011–1020. doi: https://doi.org/10.2138/am-2018-6346
105. Vaniman, D. T., Chipera, S. J., Martinez, G., Rapin, W., Rampe, E. B., Bristow, T., Blake, D. F., Meusberger, J., Ming, D. W., Downs, R. T., Craig, P., Castle, N., Morris, R. V., Pandey, A., Yen, A. S., Achilles, C., Morrison, S. M., Simpson, S., Thorp, M., Tu, V., Tutolo, B. M., Treiman, A. H., Downs, G., Berger, J., Hazen, R. M., Des Marais, D. J., Hausrath, E., Gabriel, T. and Grotzinger, J. Near-Surface Dehydration of Salt Hydrates at Gale Crater, Mars. 55. 2024, Abstr. #1327, Houston, Texas, USA, 3/11-3/15, 2024, available at: https://www.hou.usra.edu/meetings/lpsc2024/pdf/1327.pdf
106. Gellert, R., Clark, B. C., III., and the MER Science Teams. In Situ Compositional Measurements of Rocks and Soils with the Alpha Particle X-ray Spectrometer on NASA's Mars Rovers. *Elements.* **2015**, 11(1), 39–44. doi: https://doi.org/10.2113/gselements.11.1.39
107. Rapin, W., Meslin, P.-Y., Maurice, S., Wiens, R. C., Laporte, D., Chauvir, B., Gasnault, O., Schroder, S., Beck, P., Bender, S., Beyssac, O., Cousin, A., Dehouck, E., Drouet, C., Forni, O., Nachon, M., Melikechi, N., Rondeau, B., Mangold, N. and Thomas, N. H. Quantification of water content by laser induced breakdown spectroscopy on Mars. *Spectrochimica Acta Part B: Atomic Spectroscopy*, 2017, 130, 82–100. doi: https://doi.org/10.1016/j.sab.2017.02.007
108. McLennan. Sedimentary silica on Mars. *Geology.* **2003**, 31 (4): 315–318. doi: https://doi.org/10.1130/0091-7613(2003)031%3C0315:SSOM%3E2.0.CO;2
109. McLennan, S. M., Bell III, J. F., Calvin, W. M., Christensen, P. R., Clark, B. C., deSouza, P. A., Farmer, J., Farrand, W. H., Fike, D. A., Gellert, R., Gosh, A., Glotch, T. D., Grotzinger, J. P., Hahn, B., Herkenhoff, K. E., Hurrowitz, J. A., Johnson, J. R., Johnson, S. S., Joliff, B., Klingelhofer, G., Knoll, A. H., Learner, Z., Malin, M. C., McSween Jr, H. Y., Pocock, J., Ruff, S. W., Soderblom, L.,

Squyres, S. W., Tosca, N. J., Watters, W. A., Wyatt, M. B., and Yen, A. Provenance and diagenesis of the evaporite-bearing Burns formation, Meridiani Planum, Mars. *EPSL*. **2005**, 240, 95-121. doi: https://doi.org/10.1016/j.epsl.2005.09.041

110. Squyres S.W., Arvidson R.E., Ruff, S., Gellert, R., Morris, R. V., Ming, D. W., Crumpler, L., Farmer, J. D., Des Marais, D. J., Yen, A., McLennan, S. M., Calvin, W., Bell III, J. F., Clark, B. C., Wang, A., McCoy, T. J., Schmidt, M. E. and de Souza Jr, sP. A. Detection of Silica-Rich Deposits on Mars. *Science*. **2008**, 320, pp. 1063-1067. doi: http://doi.org/10.1126/science.1155429
111. Milliken, R. E., Swayze, G. A., Arvidson, R. E., Bishop, J. L., Clark, R. N., Ehlmann, B. L., Green, R. O., Grotzinger, J. P., Morris, R. V., Murchie, S. L., Miustard, J. F., and Weitz, C. Opaline silica in young deposits on Mars. *Geology*. **2008**, 36(11), 847-850. doi: https://doi.org/10.1130/G24967A.1
112. Maliva, R. G., Knoll, A. H. and Siever, R. Secular Change in Chert Distribution: A Reflection of Evolving Biological Participation in the Silica Cycle. *Palaios*. **1989**, 4 (6) (1989), pp. 519-532 PALAIOS (1989) 4 (6): 519–532. doi: https://doi.org/10.2307/3514743
113. Tosca, N. J. and Knoll A. H. Juvenile chemical sediments and the long term persistence of water at the surface of Mars. *EPSL*. **2009**, 286, issues 3-4, pp 379-386. doi: https://doi.org/10.1016/j.epsl.2009.07.004
114. Achilles, C.N., Rampe, E.B., Downs, R.T., Bristow, T.F., Ming, D.W., Morris, R.V., Vaniman, D.T., Blake, D.F., Yen, A.S., McAdam, A.C. and Sutter, B. Evidence for multiple diagenetic episodes in ancient fluvial‐lacustrine sedimentary rocks in Gale crater, Mars. *JGR: Planets*. **2020**, 125(8), p.e2019JE006295.
115. Dehouck, E., Gaudin, A., Mangold, N. Lajaunie, L. Dauzeres, A., Grauby, O., Le Menn, E. Weathereing of olivine under $CO_2$ atmosphere: A martian perspective. *GCA*. **2014**, 135, pp.170-189.
116. Smith, R. J., McLennan, S. M., Achilles, C. N., Dehouck, E., Horgan, B. H. N., Mangold, N., Rampe, E. B., Salvatore, M., Siebach, K. L., Sun, V. X-Ray Amorphous Components in Sedimentary Rocks of Gale Crater, Mars: Evidence for Ancient Formation and Long-Lived Aqueous Activity. *JGR: Planets*. **2021**, 126(3). doi: https://doi.org/10.1029/2020JE006782
117. Treiman, A.H., Bish, D.L., Vaniman, D.T., Chipera, S.J., Blake, D.F., Ming, D.W., Morris, R.V., Bristow, T.F., Morrison, S.M., Baker, M.B. and Rampe, E.B. Mineralogy, provenance, and diagenesis of a potassic basaltic sandstone on Mars: CheMin X‐ray diffraction of the Windjana sample (Kimberley area, Gale crater). *JGR: Planets*. **2016**, 121(1), pp.75-106. doi: https://agupubs.onlinelibrary.wiley.com/doi/full/10.1002/2015JE004932
118. Smith, R. J., McLennan, S. M., Sutter, B., Rampe, E. B., Dehouck, E., Siebach, K. L., Horgan, B. H. N., Sun, V., McAdam, A., Mangold, N., Vaniman, D., Salvatore, M., Thorpe, M. T., Achilles, C. N. X-Ray Amorphous Sulfur-Bearing Phases in Sedimentary Rocks of Gale Crater, Mars. *JGR: Planets*. **2022**, 127, e2021JE007128. doi: https://doi.org/10.1029/2021JE007128
119. Sutter, B., Mcadam, A.C., Mahaffy, P.R., Ming, D.W., Edgett, K.S., Rampe, E.B., Eigenbrode, J.L., Franz, H.B., Freissinet, C., Grotzinger, J.P. and Steele, A. Evolved gas analyses of sedimentary rocks and eolian sediment in Gale Crater, Mars: Results of the Curiosity rover's sample analysis at Mars instrument from Yellowknife Bay to the Namib Dune. *JGR: Planets*, **2017**, 122(12), pp.2574-2609.
120. Grotzinger, J., Beaty, D., Dromart, G., Gupta, S., Harris, M., Hurowitz, J., Kocurek, G., McLennan, S., Milliken, R., Ori, G.G. and Sumner, D. Mars sedimentary geology: key concepts and outstanding questions. *Astrobiology*. **2011**, 11, 1, 77-87. doi: Mars Sedimentary Geology: Key Concepts and Outstanding Questions | Astrobiology (liebertpub.com)
121. Day, M. and Kocurek, G. Observations of an aeolian landscape: From surface to orbit in Gale Crater. *Icarus*. **2016**, 280, pp.37-71. doi: Observations of an aeolian landscape: From surface to orbit in Gale Crater - ScienceDirect
122. Kite, E., Lewis, K., Lamb, M., Newman, C., Richardson, M. Growth and form of the mound in Gale Crater, Mars: Slope wind enhanced erosion and transport. *Geology*. 2013, 41, 543-546. https://doi.org/10.1130/G33909.1
123. Borlina, C. S., Ehlmann, B. L. and Kite, E. S. Modeling the thermal and physical evolution of Mount Sharp's sedimentary rocks, Gale Crater, Mars: Implications for diagenesis on the MSL Curiosity rover traverse *J. Geophys. Res. Planets*. **2015**, 120, 1396-1414. doi: https://doi.org/10.1002/2015JE004799

124. Lewis, K.W., Peters, S., Gonter, K., Morrison, S., Schmerr, N., Vasavada, A.R. and Gabriel, T. A surface gravity traverse on Mars indicates low bedrock density at Gale crater. *Science*. **2019,** 363(6426), pp.535-537. doi: A surface gravity traverse on Mars indicates low bedrock density at Gale crater | Science
125. Palucis, M. C., Dietrich, W. E., Williams, R. M. E., Hayes, A. G., Parker, T., Sumner, D. Y., Mangold, N., Lewis, K. and Newsom, H. Sequence and relative timing of large lakes in Gale crater (Mars) after the formation of Mount Sharp. *J. Geophys. Res. Planets*, **2016**, 121, 472–496. doi: http://doi.org/10.1002/2015JE004905
126. National Academies of Sciences, Engineering, and Medicine 2022. Origins, Worlds, and Life: A Decadal Strategy for Planetary Science and Astrobiology 2023-2032. Washington, DC: The National Academies Press. https://doi.org/10.17226/26522.
127. Hazen, R. M., Downs, R. T., Morrison, S. M., Tutolo, B. M., Blake, D. F., Bristow, T. F., Chipera, S. J., McSween, H. Y., Ming, D. L., Morris, R. V., Rampe, E. B., Thorpe, M. T., Treiman, A. H., Tu, V. M. and Vaniman, D. T. On the Diversity and Formation Modes of Martian Minerals. *JGR: Planets*. **2023**, 128, e2023JE007865. doi: https://doi.org/10.1029/2023JE007865
128. Hazen, R. M., Papineau, D., Bleeker, W., Downs, R. T., Ferry, J. M., McCoy, T. L., Sverjensky, D. A. and Yang, H. Mineral evolution. *Am Min*. **2008**, 93(11-12), 1693-1720. Doi: https://doi.org/10.2138/am.2008.2955
129. Hazen, R. M. and Morrison, S. M. On the paragenetic modes of minerals: A mineral evolution perspective. *Am Min*. **2022**, 107 (7): 1262–1287. doi: https://doi.org/10.2138/am-2022-8099
130. Grant, J. A., Golombek, M. P., Parker, T. J., Crisp, J. A., Squyres, S. W. and Weitz, C. M. Selecting landing sites for the 2003 Mars Exploration Rovers. *Planet. Space Sci*. **2004**, 52 pp. 11-21. doi: https://doi.org/10.1016/j.pss.2003.08.011
131. Grant, J. A., Golombek, M. P., Grotzinger, J. P., Wilson, S. A., Watkins, M. M., Vasavada, A. R., Griffes, J. L. and Parker, T. J. The science process for selecting the landing site for the 2011 Mars Science Laboratory. *Planet. Space Sci*. **2011**, 59 pp. 1114-1127. doi: https://doi.org/10.1016/j.pss.2010.06.016
132. Grant, J. A., Golombek, M. P., Wilson, S. A., Farley, K. A., Williford, K. H. and Chen, A. The science process for selecting the landing site for the 2020 Mars rover. *Planet. Space Sci*. **2018**, 164 pp. 106-126. doi: https://doi.org/10.1016/j.pss.2018.07.001
133. Farley, K.A., Williford, K.H., Stack, K.M., Williford, K. H., Stack, K. M., Chen, A., de la Torre, M., Hand, K., Goreva, Y., Liu, Y., Maki, J. N., Moeller, R. C., Nelessen, A., Nunes, D., Ponce, A., Spanovich, N., Willis, P. A., Beegle, L. W., Bhartia, R., Herd, C. D. K., Hueso, R., Martinez, G., Newman, C. E., Bell, J. F. III, Brown, A. J., Hamran, S-E., Hurowitz, J. A., Maurice, S., Paige, D. A., Rodriguez-Manfredi, J. A., Schulte, M., Wiens, R. C. Mars 2020 Mission Overview. *Space Sci Rev*. **2020**, 216, 142. doi: https://doi.org/10.1007/s11214-020-00762-y
134. Rampe, E.B., Bristow, T.F., Blake, D.F., Vaniman, D.T., Chipera, S.J., Downs, R.T., Ming, D.W., Morris, R.V., Tu, V.M., Thorpe, M.T. and Yen, A.S. Mineralogical trends over the clay-sulfate transition in Gale Crater from the Mars Science Laboratory CheMin instrument. In LPSC, Houston, Texas, USA, 3/7-3/11, 2022. doi: Mineralogical Trends Over the Clay-Sulfate Transition in Gale Crater from the Mars Science Laboratory CheMin Instrument - NASA Technical Reports Server (NTRS)
135. Rampe, E.B., Sarrazin, P., Blake, D.F., Bristow, T.F., Yen, A.S., Downs, R.T., Tu, V.M., Zacny, K., Lafuente, B., Thompson, K. and Gailhanou, M., 2024, March. Advances in X-ray Instruments to Support Mars Sample Return. In 55th LPSC, Houston, Texas, USA 3/11-3/15, 2024. doi: Advances in X-ray Instruments to Support Mars Sample Return - NASA Technical Reports Server (NTRS)
136. Anderson, R. B. and Bell, J. F. III. Geologic mapping and characterization of Gale Crater and implications for its potential as a Mars Science Laboratory landing site. *The International Journal of Mars Science and Exploration*. **2010**, 76–128, doi: http://dx.doi.org/10.1555/mars.2010.0004
137. Siebach, K. L. and Grotzinger, J. P. Volumetric estimates of ancient water on Mount Sharp based on boxwork deposits, Gale Crater, Mars. *JGR Planets*. **2013**, 119(1), 189-198. doi: https://doi.org/10.1002/2013JE004508
138. Achilles, C. N., Downs, R. T., Ming, D. W., Rampe, E. B., Morris, R. V., Treiman, A. H., Morrison, S. M, Blake, D. F. , Vaniman, D. T., Ewing, R. C., Chipera, S. J., Yen, A. S., Bristow, T. F., Ehlmann, B. L., Gellert, R., Hazen, R. M., Fendrich, K. V., Craig, P. I.,

Grotzinger, J. P., Des Marais, D. J., Farmer, J. D., Sarrazin, P. C., and Morookian, J. M. Mineralogy of an active eolian sediment from the Namib dune, Gale crater, Mars, J. Geophys. Res. Planets, **2017**, 122. doi:10.1002/2017JE005262.